Theoretical Study of Radio Telescope Optics with Wide Field of View

Hiroaki Imada

February 2016

Theoretical Study of Radio Telescope Optics with Wide Field of View

Hiroaki Imada
Doctoral Program in Physics

Submitted to the Graduate School of
Pure and Applied Sciences
in Partial Fulfillment of the Requirements
for the Degree of Doctor of Philosophy in
Science

at the
University of Tsukuba

Abstract

The parameters which describe the properties of an antenna are theoretically considered. In considering a receiving antenna, a receiving beam pattern and an effective aperture area are proved to be the most fundamental parameters. Both parameters can determine the properties of an antenna completely. By assuming reciprocity, the parameters mentioned above can be predicted via transmitting properties.

In case of an aperture antenna, the parameters are also explicitly expressed. In addition, if receiver sensitivity is assumed, parameters describing antenna properties can be determined only by the parameters of the receiver sensitivity. An aperture efficiency is defined as the ratio of an effective aperture area to a physical aperture area, which is composed of two spillover efficiencies and an optical, or coupling, efficiency. The spillover efficiency at the entrance pupil has been ignored until now but it is needed when a wide field-of-view telescope is considered.

When a radio telescope is designed, there are ultimately two requirements. In case of a single-beam telescope, the way to design an optical system satisfying these requirements is known well but the way in case of an arbitrary beam is not known. When a wide field-of-view telescope is considered, generalized theories are necessary.

Extension of the theories for a single-beam telescope is demonstrated theoretically. The condition for images independet of frequency is proved to be the lens formula. It is also achieved that the dependence of an aperture efficiency is written analytically as a function of the aberration coefficients and the parameters of detector sensitivity. This expression enables to evaluate both effects of geometry and diffraction.

In generalizing the theories, it is revealed that geometrical optics has an important role even when a radio telescope dealing with strongly coherent wave is considered. A novel method to design a radio telescope is proposed on the basis of the results. As a concise application, calculating the aperture efficiency of the 10-m THz telescope in Antarctica which is planned by University of Tsukuba is demonstrated. The optical design is proved to be almost perfect.

A novel wavefront sensor, which can be applied to radio devices, is discueed because wavefront sensing is an important technique to construct an optical system and to operate a telescope.

Acknowledgement

I am most grateful to Professor Naomasa Nakai, my supervisor, for giving me a chance to study optics. He has taught me not only astronomical things but also importance to have a great curiosity about everything as well as perseverance. I have to thank him for allowing me to work with respet to the project for astronomy in Antarctica. I am grateful to Professor Masumichi Seta, who has moved to Kwansei Gakuin University, for advising me what I should do to various problems. The experience through the 30-cm telescope in University of Tsukuba, including the operation of it in Chile, is precious to me. I am obliged to Professor Nario Kuno for giving me useful viewpoints at the appropriate time. I appreciate that Dr. Makoto Nagai spended much time discussing optics in radio bands with me. The contents in this thesis could not be mature without him. I am so happy to have a chance to discuss many things with him. I thank Assistant Professor Tom Nitta for helping me to make improvements on the ideas used in this thesis.

I appreciate that Associate Professor Yutaro Sekimoto and Mr. Toshihiro Tsuzuki have fruitful discussions with me and lead me when I am in trouble. I thank Dr. Yusuke Miyamoto, and Dr. Shun Ishii, who also took care of me in the master course, for encouraging writing my thesis. I thank Professor Hideo Ogawa, Dr. Kimihiro Kimura, Mr. Kazuki Tokuda, and Mr. Yutaka Hasegawa for discussing various things relating this thesis and giving a chance to access to the 1.85-m telescope at the Nobeyama Radio Observatory. I am grateful to Dr. Taro Matsuo, Dr. Masaru Kino, and Dr. Kodai Yamamoto for collaboration with me and completing the study of wavefront sensor. Discussion with them makes my present understandings about optics.

I could never complete this thesis without the great efforts made by the members in the laboratory; Shinji Fujita, Ken Asakura, Hiroya Uenishi, Iori Tanaka, Takuya Hatakeyama, Shunsuke Hisamatsu, Yoshino Yamada, Kaoaru Isami, Taishi Okumura, Mika Kuriki, Takahiro Tanaka, Yuto Tomiyasu and Zhou Bin. My longtime friends since the high school and the undergraduate school are thankful for encouraging me.

I sincerely appreciate that Professor Fumihiko Ukegawa and Professor Hiroshi Shibai referee this thesis and give the suggestions which significantly improves it.

Finally, I thank my parents, Kazuo and Ikuko, and my sister, Chikage, for supporting and encouraging me.

Contents

List of Figures

List of Tables

1

Introduction

1.1 Requirements to Radio Telescope in a New Era

Observation over the whole sky in a wide range of frequency is important to unveil the properties of celestial objects. Most of the radio telescopes constructed until now are, however, designed as a single-beam telescope capable of observing only one point toward which it is directed. Various plans of radio telescopes are proposed and require that a telescope should observe many points simultaneously in order to reduce observing time to cover the whole sky. For example, University of Tsukuba is planning to construct a 10-m THz telescope in Antarctica (Figure 1.1). Its science targets are mainly high redshift galaxies. It is required to operate at 400–1300 GHz and has a 1-degree^2 field of view for whole sky surveys. Cerro Chajnantor Atacama Telescope (CCAT, Riechers et al. 2015) should be also mentioned as another example (Figure 1.2). It is 25 meter in diameter and also has a 1-degree^2 field of view for high mapping speed. It will operate in the range of 140–860 GHz and work as a general-purpose telescope for various science targets (Glenn et al. 2012). One of the common points among these plans is "a wide field of view", or multi-beam, and another is "wide bandwidth". This thesis focuses on these two points.

1.2 Wide Field of View

It is necessary to extend the theories of a single-beam radio telescope which are already completed and insufficient to be applied to a wide field-of-view system. There are two factors to be considered when a multi-beam radio telescope is constructed. One is an optical system of a radio telescope and the other is multi-pixel detectors. Multi-pixel detectors have recently appeared and are being energetically developed (e.g., Baselmans 2012; Nitta et al. 2014). Development of a wide field-of-view radio telescope gets gradually in progress (e.g., Padin et al. 2010; Tsuzuki et al. 2015), but is behind the development of multi-pixel detectors. Although there are several radio telescopes with a wide field of view already constructed, e.g., South Pole Telescope (Padin et al. 2008; Carlstrom et al. 2011) and Aatacama Cosmology Telescope (Fowler et al. 2007), theoretical consideration of optics was not sufficiently carried out thanks to much longer wavelength than visible or infrared light. It might be easy to be confronted with a problem that an optical system of a wide field-of-view telescope cannot be designed in shorter wavelength bands, such as sub-mm or THz bands.

In optical or infrared astronomy, a wide field-of-view telescope has already been invented, e.g., Schmidt telescopes (Wilson 2007), or designed using geometrical optics. A recent example is Large Synoptic Survey Telescope (Terebizh 2008). It seems inevitable to use geometrical optics for designing a wide field-of-view radio telescope. However, it is not obvious whether one may use geometrical optics which cannot provide information on the effects of diffraction. A radio

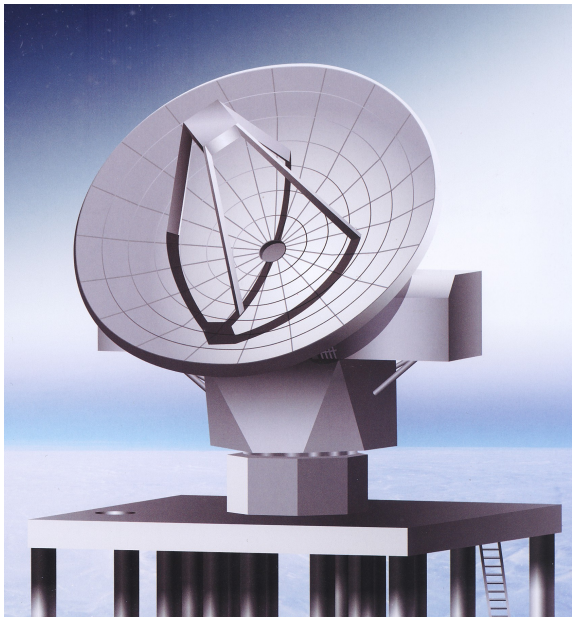

Figure 1.1: A 10-m THz telescope in Antarctica, planned by University of Tsukuba (`http://www.px.tsukuba.ac.jp/~nakai/astroobs/antarctica.html`)

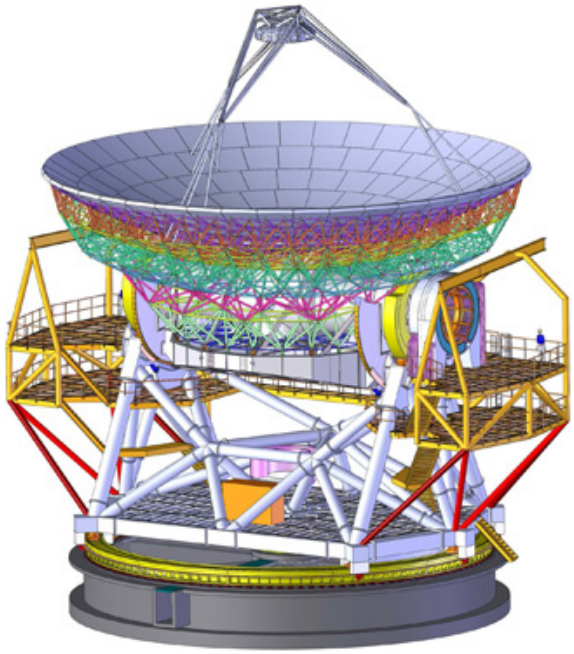

Figure 1.2: CCAT. (`https://www.ccatobservatory.org/index.cfm/page/observatory/telescope-facts.htm`)

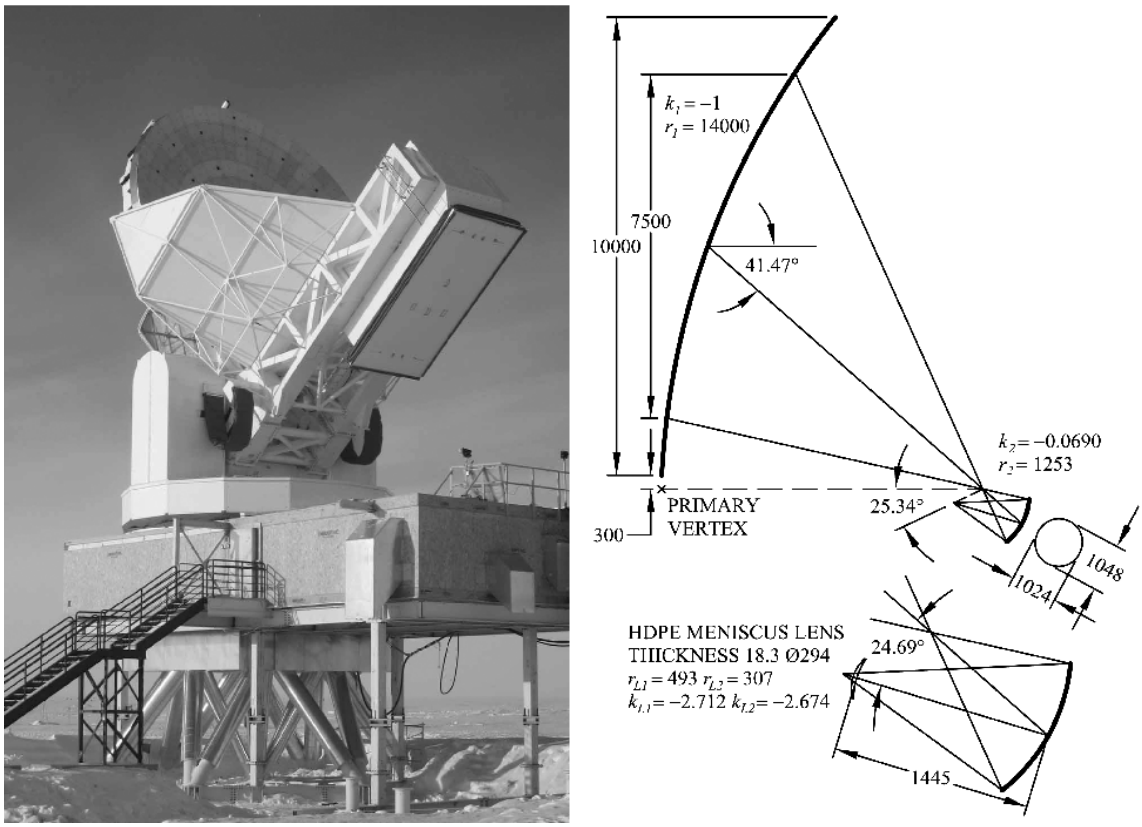

Figure 1.3: SPT. Left: appearance. Right: Optics (Padin et al. 2008).

telescope generally transmits long wave which interferes itself, and therefore, diffraction should be considered. In case of a radio telescope, quasi optics, or Gaussian beams, can describes the behavior of electromagnetic wave in a telescope well.

There is another problem to complicate application of geometrical optics to designing a radio telescope. In optical or near infrared regions, one can shut stray light out and use detectors with isotropic sensitivity. It is sufficient to consider only rays passing through an optical system by using geometrical parameters, such as Strehl ratio, unless diffraction needs to be evaluated. On the other hands, in radio bands, everything with finite temperature emits radiation which enters detectors, which makes it difficult to shut stray light out. Detectors used in a radio telescope have to be sensitive to the radiation coming through an optical system, i.e., detectors has the dependence of sensitivity on derection. As a result, parameters used in designing a radio telescope or quasi optics, such as an aperture efficiency, are completely different from those used in an optical telescope or geometrical optics.

Under the assumption that geometrical optics plays an important role in designing a wide field-of-view radio telescope and is used, problems to be discussed are the evaluation of diffraction and the relations between parameters used in geometrical optics and quasi optics.

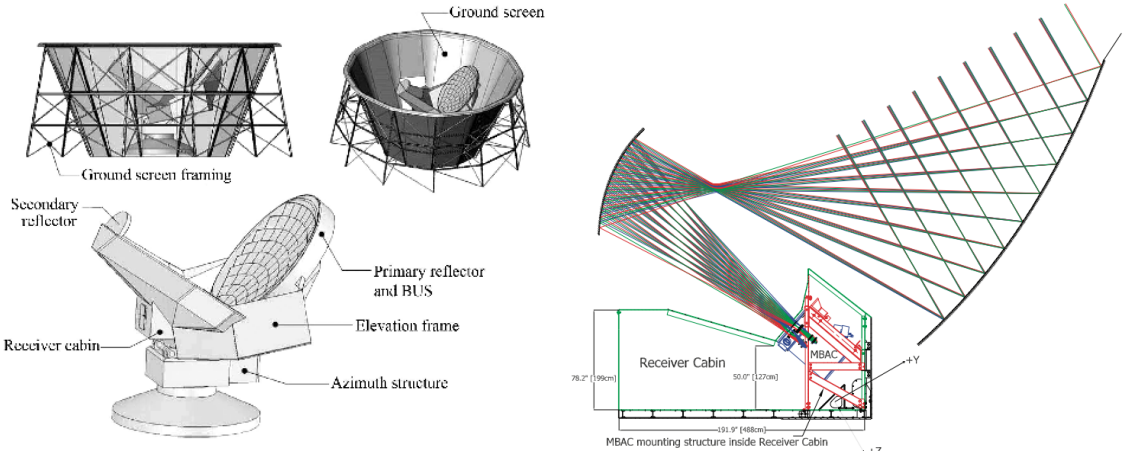

Figure 1.4: ACT. Left: appearance. Right: Optics (Fowler et al. 2007).

1.3 Wide Bandwidth

As mentioned at the beginning, astronomical radio observation over a wide range of frequency is important. Many single-beam telescopes are actually operating with a wide bandwidth. For example, the Atacama Large Millimeter/Submillimeter Array (ALMA) which started science operations in 2011 covers the frequency range from 84 GHz up to 950 GHz, which will be expanded on completion of ALMA: from 31 GHz up to 950 GHz (Remijan et al. 2015). The highest frequency is about 30 times higher than the lowest frequency, which means that the effects of diffraction at the lowest frequency are quite different from those at the highest one.

For a single-beam telescope, it is known that there are specific positions where the properties of a beam are independent of frequency under a certain condition. The telescope constructed copes with frequency dependence by using the condition. Extension of this condition is also one of the problems to be discussed.

1.4 Goal of This Thesis

This thesis discusses extension of the theories which are completed for a single-beam telescope and shows concise examples of using the extended theories. The problems to be discussed are three as demonstrated in Sections 1.2 and 1.3:

1. how are the effects of diffraction evaluated if geometrical optics is used?

2. what relations exist between parameters used in geometrical optics and quasi optics?

3. can the frequency-independent condition for a single-beam telescope be extended?

In Chapter 2, the most fundamental parameters which describe the properties of an antenna are introduced by considering two cases in which an antenna receives radiation from a point source and in which from an isotropic source. Other parameters can be derived from the two parameters. In Chapter 3, the parameters in case of an aperture antenna are explicitly expressed. In Chapter 4, the problems to be discussed are considered theoretically. It is proved that geometrical optics is so useful to design a wide field-of-view telescope. A novel method to design a radio telescope is proposed, which uses both geometrical optics and quasi optics. Chapter 5 shows a concise application of the result in Chapter 4. In Chapter 6, a wavefront sensor which can be applied to radio devices is discussed. A wavefront sensor will be necessary to construct and operate a large sub-millimeter or a THz telescope in the future because wavefront sensing is imperative in the manufacture of optical elements and the calibration of an optical system.

2

Parameters Characterizing Antenna

2.1 Introduction

A telescope used in Astronomy gives us how much energy comes from specific directions. In this section, parameters characterizing a radio telescope and quantities obtained through it are introduced in terms of a receiving antenna. Finally, the relation between reciprocity and parameters of a receiving antenna is discussed.

2.2 Measurable Quantities

In case of a radio telescope, a measurable quantity is usually electric power at a frequency of ν with a bandwidth of $\mathrm{d}\nu$, $W_\nu(\theta,\phi)\,\mathrm{d}\nu$. The unit of $W_\nu(\theta,\phi)$ is $\mathrm{W\,Hz^{-1}}$.

2.2.1 Receiving Beam Pattern

A model which is composed of a receiving antenna and a point source at infinity as shown in Figure 2.1 is considered. The spherical coordinates (θ',ϕ') are defined such that the axes $(\theta',\phi') = (0,0)$ and $(\theta',\phi') = (\pi/2,0)$ coincide with axes which typifies the direction of the antenna or the support structure of it. Note that $0 \leq \theta' \leq \pi$ and $0 \leq \phi' \leq 2\pi$. It is assumed that the medium between the antenna and the point source is a homogeneous and isotropic one.

$P'_\nu(\theta',\phi')\,\mathrm{d}\nu$ is defined as the power received through the antenna in the case where the point source is located at (θ',ϕ'). $P'_\nu(\theta',\phi')\,\mathrm{d}\nu$ is determined by measurements, in W. In most cases, $P'_\nu(\theta',\phi')\,\mathrm{d}\nu$ has a maximum and let (Θ',Φ') be the direction of the maximum. By using the maximum, the normalized receiving beam pattern can be defined as

$$P'_{\mathrm{n},\nu}(\theta',\phi') := \frac{P'_\nu(\theta',\phi')\,\mathrm{d}\nu}{P'_\nu(\Theta',\Phi')\,\mathrm{d}\nu}. \tag{2.1}$$

$P'_{\mathrm{n},\nu}(\theta',\phi')$ represents the dependence of an antenna sensitivity on direction. It is a fundamental parameter and determines power entering a receiver from celestial objects.

Other spherical coordinates (θ,ϕ) are introduced. Let the coordinates (θ,ϕ) represent the position on the celestial sphere. $(\theta,\phi) = (0,0)$ corresponds to the zenith. Note that $0 \leq \theta \leq \pi$ and $0 \leq \phi \leq 2\pi$. When the axis $(\theta',\phi') = (0,0)$ points toward the direction $(\theta,\phi) = (\theta_{\mathrm{ant}},\phi_{\mathrm{ant}})$, the normalized receiving beam pattern on the celestial sphere can be written as

$$P_{\mathrm{n},\nu}(\theta,\phi;\theta_{\mathrm{ant}},\phi_{\mathrm{ant}}) = P'_{\mathrm{n},\nu}(\theta',\phi'), \tag{2.2}$$

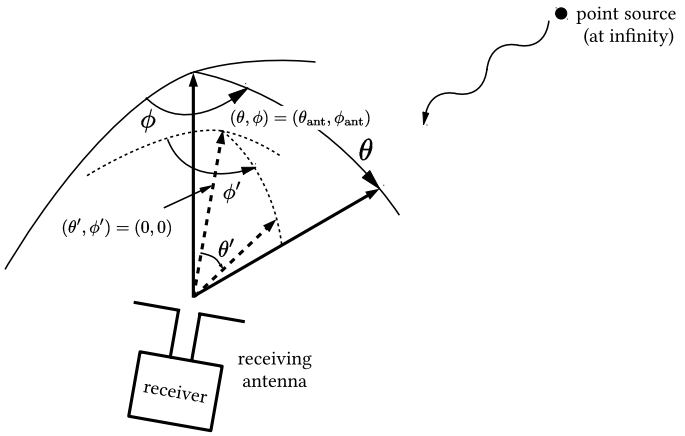

Figure 2.1: The model under consideration. It is composed of the receiving antenna, the point source, and the spherical coordinates (θ', ϕ') and (θ, ϕ).

where the relation between (θ, ϕ) and (θ', ϕ') is given by, e.g.,

$$\begin{aligned}\begin{pmatrix}\sin\theta'\cos\phi'\\ \sin\theta'\sin\phi'\\ \cos\theta'\end{pmatrix} &= \begin{pmatrix}\cos\theta_{\rm ant} & 0 & -\sin\theta_{\rm ant}\\ 0 & 1 & 0\\ \sin\theta_{\rm ant} & 0 & \cos\theta_{\rm ant}\end{pmatrix}\begin{pmatrix}\cos\phi_{\rm ant} & \sin\phi_{\rm ant} & 0\\ -\sin\phi_{\rm ant} & \cos\phi_{\rm ant} & 0\\ 0 & 0 & 1\end{pmatrix}\begin{pmatrix}\sin\theta\cos\phi\\ \sin\theta\sin\phi\\ \cos\theta\end{pmatrix}\\ &= \begin{pmatrix}\cos\theta_{\rm ant}\cos\phi_{\rm ant} & \cos\theta_{\rm ant}\sin\phi_{\rm ant} & -\sin\theta_{\rm ant}\\ -\sin\phi_{\rm ant} & \cos\phi_{\rm ant} & 0\\ \sin\theta_{\rm ant}\cos\phi_{\rm ant} & \sin\theta_{\rm ant}\sin\phi_{\rm ant} & \cos\theta_{\rm ant}\end{pmatrix}\begin{pmatrix}\sin\theta\cos\phi\\ \sin\theta\sin\phi\\ \cos\theta\end{pmatrix}. \qquad (2.3)\end{aligned}$$

Equation (2.3) yields

$$\tan\theta' = \frac{\sqrt{\left[\sin\theta\cos\theta_{\rm ant}\cos(\phi-\phi_{\rm ant}) - \sin\theta_{\rm ant}\cos\theta\right]^2 + \sin^2\theta\sin^2(\phi-\phi_{\rm ant})}}{\sin\theta\sin\theta_{\rm ant}\cos(\phi-\phi_{\rm ant}) + \cos\theta\cos\theta_{\rm ant}}, \qquad (2.4)$$

$$\tan\phi' = \frac{\sin\theta\sin(\phi-\phi_{\rm ant})}{\sin\theta\cos\theta_{\rm ant}\cos(\phi-\phi_{\rm ant}) - \sin\theta_{\rm ant}\cos\theta}. \qquad (2.5)$$

If θ, ϕ, θ', ϕ', $\theta_{\rm ant}$, and $\phi_{\rm ant} \ll 1$, then Equations (2.4) and (2.5) reduce to

$$\theta' \simeq \theta - \theta_{\rm ant}, \qquad (2.6)$$

$$\frac{\phi'}{\theta} \simeq \frac{\phi - \phi_{\rm ant}}{\theta'}. \qquad (2.7)$$

The coordinates (Θ, Φ) are introduced such that

$$P_{{\rm n},\nu}(\Theta, \Phi; \theta_{\rm ant}, \phi_{\rm ant}) = 1. \qquad (2.8)$$

The role of (Θ, Φ) is the same as that of (Θ', Φ'). By using the inversion relation of Equation (2.3),

(Θ, Φ) can be determined from (Θ', Φ').

2.2.2 Antenna Temperature and Radiation Temperature

Using the normalized beam pattern $P_{\mathrm{n},\nu}(\theta, \phi; \theta_{\mathrm{ant}}, \phi_{\mathrm{ant}})$ defined in Section 2.2.1, one can express power entering a receiver from a source with an intensity distribution $I_\nu(\theta, \phi)$ whose unit is $\mathrm{W\,m^{-2}\,Hz^{-1}\,sr^{-1}}$. The power entering a receiver, $W_\nu(\theta_{\mathrm{ant}}, \phi_{\mathrm{ant}})\,\mathrm{d}\nu$, can be written as

$$W_\nu(\theta_{\mathrm{ant}}, \phi_{\mathrm{ant}})\,\mathrm{d}\nu = \eta'_{\mathrm{ant}}(\theta_{\mathrm{ant}}, \phi_{\mathrm{ant}})\lambda^2\,\mathrm{d}\nu \iint_{4\pi} \eta_{\mathrm{mut}}(\theta, \phi; \theta_{\mathrm{ant}}, \phi_{\mathrm{ant}}) P_{\mathrm{n},\nu}(\theta, \phi; \theta_{\mathrm{ant}}, \phi_{\mathrm{ant}}) I_\nu(\theta, \phi)\mathrm{d}\Omega, \tag{2.9}$$

where λ is wavelength and $\mathrm{d}\Omega = \sin\theta \mathrm{d}\theta\mathrm{d}\phi$. Note that a passive antenna and passive media are assumed. $\eta'_{\mathrm{ant}}(\theta_{\mathrm{ant}}, \phi_{\mathrm{ant}})$ is the efficiency of an antenna and can be calculated when an antenna is specified. λ^2 makes $\eta'_{\mathrm{ant}}(\theta_{\mathrm{ant}}, \phi_{\mathrm{ant}})$ be a dimensionless quantity. It is usually expected that the performance of an antenna, i.e., $\eta'_{\mathrm{ant}}(\theta_{\mathrm{ant}}, \phi_{\mathrm{ant}})$, is designed to be independent of its posture $(\theta_{\mathrm{ant}}, \phi_{\mathrm{ant}})$. η_{mut} is the efficiencies determined by the mutual properties among media, sources, and a receiver, e.g., absorption, polarization.

In radio astronomy, $W_\nu(\theta_{\mathrm{ant}}, \phi_{\mathrm{ant}})$ is often converted into antenna temperature T_{A}. Nyquist (1928) showed theoretically that a resistor with temperature of T_{res} produces some power at a frequency of ν with a bandwidth of $\mathrm{d}\nu$, $P_{\mathrm{res},\nu}(T_{\mathrm{res}})\,\mathrm{d}\nu$. The concept of the antenna temperature originates from expressing the power $W_\nu(\theta_{\mathrm{ant}}, \phi_{\mathrm{ant}})\,\mathrm{d}\nu$ using the resistor temperature T_{res} such that $P_{\mathrm{res},\nu}(T_{\mathrm{res}})\,\mathrm{d}\nu = W_\nu(\theta_{\mathrm{ant}}, \phi_{\mathrm{ant}})\,\mathrm{d}\nu$ in the Rayleigh-Jeans region. Because $P_{\mathrm{res},\nu}(T_{\mathrm{res}})\,\mathrm{d}\nu \simeq k_{\mathrm{B}} T_{\mathrm{res}}\,\mathrm{d}\nu$ in the Rayleigh-Jeans region, and therefore, the antenna temperature T_{A}, in Kelvin, is defined as

$$T_{\mathrm{A}}(\theta_{\mathrm{ant}}, \phi_{\mathrm{ant}}) := \frac{W_\nu(\theta_{\mathrm{ant}}, \phi_{\mathrm{ant}})\,\mathrm{d}\nu}{k_{\mathrm{B}}\,\mathrm{d}\nu}, \tag{2.10}$$

where k_{B} is the Boltzmann constant, $1.381 \times 10^{-23}\ \mathrm{W\,K^{-1}\,Hz^{-1}}$. However, the Rayleigh-Jeans approximation breaks down in case where the frequency of radiation is higher or the temperature of a resistor is lower. According to Nyquist (1928),

$$P_{\mathrm{res},\nu}(T_{\mathrm{res}})\,\mathrm{d}\nu = \frac{h_{\mathrm{P}}\nu}{\exp\left(h_{\mathrm{P}}\nu / k_{\mathrm{B}} T_{\mathrm{res}}\right) - 1}\,\mathrm{d}\nu, \tag{2.11}$$

where h_{P} is the Planck constant, $6.626 \times 10^{-34}\ \mathrm{W\,Hz^{-2}}$. The antenna temperature T_{A} differs from the physical temperature of a resistor, T_{res}.

Next, focus on the brightness distribution $I_\nu(\theta, \phi)$ in Equation (2.9). $I_\nu(\theta, \phi)$ is converted into radiation temperature $J_\nu(\theta, \phi)$ in $\mathrm{K\,sr^{-1}}$. When the radiation of a black body with a thermody-

namic temperature of $T_{\rm bb}$ is equal to $I_\nu(\theta,\phi)$, the radiation temperature $J_\nu(\theta,\phi)$ is defined as

$$\frac{2h_{\rm P}\nu^3}{c^2}\frac{1}{\exp(h_{\rm P}\nu/k_{\rm B}T_{\rm bb})-1}\,{\rm d}\nu := I_\nu(\theta,\phi)\,{\rm d}\nu. \tag{2.12}$$

$$J_\nu(\theta,\phi) := \frac{\lambda^2}{2k_{\rm B}\,{\rm d}\nu}I_\nu(\theta,\phi)\,{\rm d}\nu. \tag{2.13}$$

Note that Equation (2.12) is the definition of the thermodynamic temperature $T_{\rm bb}$. In the Rayleigh-Jeans region, $h_{\rm P}\nu/k_{\rm B}T_{\rm bb} \ll 1$,

$$J_\nu(\theta,\phi) = \frac{\lambda^2}{2k_{\rm B}}I_\nu(\theta,\phi) \simeq T_{\rm bb}. \tag{2.14}$$

Equation (2.14) shows that the radiation temperature $J_\nu(\theta,\phi)$ corresponds to the thermodynamic temperature $T_{\rm bb}$.

Substitution of Equations (2.10) and (2.13) into Equation (2.9) yields

$$T_{\rm A}(\theta_{\rm ant},\phi_{\rm ant}) = 2\eta'_{\rm ant}(\theta_{\rm ant},\phi_{\rm ant})\iint_{4\pi}\eta_{\rm mut}(\theta,\phi;\theta_{\rm ant},\phi_{\rm ant})P_{{\rm n},\nu}(\theta,\phi;\theta_{\rm ant},\phi_{\rm ant})J_\nu(\theta,\phi){\rm d}\Omega. \tag{2.15}$$

2.2.3 Effective Aperture Area

A simple model consisting of an antenna with a receiving beam pattern $P_{{\rm n},\nu}(\theta,\phi)$ and a black body with a temperature of $T_{\rm bb}$ is considered. The black body subtends a solid angle of 4π to the antenna. The media between them are assumed to be vacuum. Under this assumption, the following relations are obtained:

$$\eta_{\rm mut}(\theta,\phi;\theta_{\rm ant},\phi_{\rm ant}) = \frac{1}{2}, \tag{2.16}$$

$$J_\nu(\theta,\phi) = J_\nu. \tag{2.17}$$

$\eta_{\rm mut}$ is determined by receiver polarization. Equation (2.15) is transformed into

$$T_{{\rm A},4\pi}(\theta_{\rm ant},\phi_{\rm ant}) = \eta'_{\rm ant}(\theta_{\rm ant},\phi_{\rm ant})\Omega_{\rm rx}J_\nu \tag{2.18}$$

$$\Omega_{\rm rx} := \iint_{4\pi}P_{{\rm n},\nu}(\theta,\phi;\theta_{\rm ant},\phi_{\rm ant}){\rm d}\Omega. \tag{2.19}$$

Note that $P_{{\rm n},\nu}(\Theta,\Phi;\theta_{\rm ant},\phi_{\rm ant}) = 1$ and the unit of J_ν is $\mathrm{K\,sr^{-1}}$. $\Omega_{\rm rx}$ defined in Equation (2.19) is called a receiving beam solid angle, which is one of antenna parameters. $T_{{\rm A},4\pi}(\theta_{\rm ant},\phi_{\rm ant})$ is a measurable quantity and J_ν can be evaluated via Equations (2.12), (2.13), and (2.17), which means that $\eta'_{\rm ant}(\theta_{\rm ant},\phi_{\rm ant})\Omega_{\rm rx}$ can be determined by measurements. Equation (2.18) indicates that antenna efficiency can be defined as the ratio of antenna temperature to radiation temperature,

and therefore, antenna efficiency $\eta_{\rm ant}$ is defined in this thesis as

$$\eta_{\rm ant}(\theta_{\rm ant},\phi_{\rm ant}) := \eta'_{\rm ant}(\theta_{\rm ant},\phi_{\rm ant})\Omega_{\rm rx}. \tag{2.20}$$

The parameters that are determined only by the properties of an antenna are gathered from Equation (2.9).

$$\eta'_{\rm ant}(\theta_{\rm ant},\phi_{\rm ant})\lambda^2 P_{{\rm n},\nu}(\theta,\phi;\theta_{\rm ant},\phi_{\rm ant}) = \eta_{\rm ant}(\theta_{\rm ant},\phi_{\rm ant})\frac{\lambda^2 P_{{\rm n},\nu}(\theta,\phi;\theta_{\rm ant},\phi_{\rm ant})}{\Omega_{\rm rx}}. \tag{2.21}$$

Equation (2.21) has the dimension of area, so that an effective aperture area is defined as

$$A_{\rm eff}(\theta,\phi;\theta_{\rm ant},\phi_{\rm ant}) := \eta_{\rm ant}(\theta_{\rm ant},\phi_{\rm ant})\frac{\lambda^2 P_{{\rm n},\nu}(\theta,\phi;\theta_{\rm ant},\phi_{\rm ant})}{\Omega_{\rm rx}\cos\theta}. \tag{2.22}$$

Equation (2.22) agrees with the result in Nagai & Imada (2016). By using Equation (2.22), Equations (2.9) and (2.15) are replaced with

$$W_\nu(\theta_{\rm ant},\phi_{\rm ant}) = \iint_{4\pi}\eta_{\rm mut}(\theta,\phi;\theta_{\rm ant},\phi_{\rm ant})I_\nu(\theta,\phi)A_{\rm eff}(\theta,\phi;\theta_{\rm ant},\phi_{\rm ant})\cos\theta{\rm d}\Omega, \tag{2.23}$$

$$T_{\rm A}(\theta_{\rm ant},\phi_{\rm ant}) = \frac{2}{\lambda^2}\iint_{4\pi}\eta_{\rm mut}(\theta,\phi;\theta_{\rm ant},\phi_{\rm ant})J_\nu(\theta,\phi)A_{\rm eff}(\theta,\phi;\theta_{\rm ant},\phi_{\rm ant})\cos\theta{\rm d}\Omega, \tag{2.24}$$

respectively. To improve efficiency of astronomical observations, it is important to enlarge the effective aperture area.

For theoretical simplicity, direction cosines (l,m) are introduced.

$$l = \sin\theta\cos\phi, \qquad m = \sin\theta\sin\phi. \tag{2.25}$$

By calculating the Jacobian matrix, the relations ${\rm d}l{\rm d}m = \sin\theta\cos\theta{\rm d}\theta{\rm d}\phi = \cos\theta{\rm d}\Omega$ are obtained. Thus, the beam pattern, Equations (2.22), (2.23), and (2.24) are also expressed as

$$\tilde{P}_{{\rm n},\nu}(l,m;l_{\rm ant},m_{\rm ant}) := \frac{P_{{\rm n},\nu}(\theta,\phi;\theta_{\rm ant},\phi_{\rm ant})}{\cos\theta} \tag{2.26}$$

$$\tilde{A}_{\rm eff}(l,m;l_{\rm ant},m_{\rm ant}) = \eta_{\rm ant}(l_{\rm ant},m_{\rm ant})\frac{\lambda^2\tilde{P}_{{\rm n},\nu}(l,m;l_{\rm ant},m_{\rm ant})}{\Omega_{\rm rx}}, \tag{2.27}$$

$$W_\nu(l_{\rm ant},m_{\rm ant}) = \iint\eta_{\rm mut}(l,m;l_{\rm ant},m_{\rm ant})I_\nu(l,m)\tilde{A}_{\rm eff}(l,m;l_{\rm ant},m_{\rm ant}){\rm d}l{\rm d}m, \tag{2.28}$$

$$T_{\rm A}(l_{\rm ant},m_{\rm ant}) = \frac{2}{\lambda^2}\iint\eta_{\rm mut}(l,m;l_{\rm ant},m_{\rm ant})J_\nu(l,m)\tilde{A}_{\rm eff}(l,m;l_{\rm ant},m_{\rm ant}){\rm d}l{\rm d}m, \tag{2.29}$$

where $l_{\rm ant} = \sin\theta_{\rm ant}\cos\phi_{\rm ant}$, $z_{\rm ant} = \sin\theta_{\rm ant}\sin\phi_{\rm ant}$.

Finally, focus on the case where a point source is observed. If a source is located at $(l,m) =$

$(l_{\rm ps}, m_{\rm ps})$, the brightness distribution $I_\nu(l, m)$ is given by

$$I_\nu(\theta, \phi) = I_{\nu,\rm ps}\delta(l - l_{\rm ps})\delta(m - m_{\rm ps}). \tag{2.30}$$

Note that the unit of $I_{\nu,\rm ps}$ is W m^{-2} Hz^{-1} sr^{-1}. Equations (2.28) and (2.29) becomes

$$\begin{aligned} W_{\nu,\rm ps}(l_{\rm ant}, m_{\rm ant}) &= \eta_{\rm mut}(l_{\rm ps}, m_{\rm ps}; l_{\rm ant}, m_{\rm ant}) I_{\nu,\rm ps}\tilde{A}_{\rm eff}(l_{\rm ps}, m_{\rm ps}; l_{\rm ant}, m_{\rm ant}) \\ &= \eta_{\rm mut}(l_{\rm ps}, m_{\rm ps}; l_{\rm ant}, m_{\rm ant})\eta_{\rm ant}(l_{\rm ant}, m_{\rm ant}) I_{\nu,\rm ps}\frac{\lambda^2\tilde{P}_{{\rm n},\nu}(l_{\rm ps}, m_{\rm ps}; l_{\rm ant}, m_{\rm ant})}{\Omega_{\rm rx}}. \end{aligned} \tag{2.31}$$

$$\begin{aligned} T_{\rm A,ps}(l_{\rm ant}, m_{\rm ant}) &= \frac{2}{\lambda^2}\eta_{\rm mut}(l_{\rm ps}, m_{\rm ps}; l_{\rm ant}, m_{\rm ant}) J_{\nu,\rm ps}\tilde{A}_{\rm eff}(l_{\rm ps}, m_{\rm ps}; l_{\rm ant}, m_{\rm ant}) \\ &= 2\eta_{\rm mut}(l_{\rm ps}, m_{\rm ps}; l_{\rm ant}, m_{\rm ant})\eta_{\rm ant}(l_{\rm ant}, m_{\rm ant}) J_{\nu,\rm ps}\frac{\tilde{P}_{{\rm n},\nu}(l_{\rm ps}, m_{\rm ps}; l_{\rm ant}, m_{\rm ant})}{\Omega_{\rm rx}}. \end{aligned} \tag{2.32}$$

Note that the unit of $J_{\nu,\rm ps}$ is K sr^{-1}. If a point source is located at $(l_{\rm ps}, m_{\rm ps}) = (l_{\max}, m_{\max})$ which is the direction of a maximum antenna sensitivity, then

$$W_{\nu,\rm ps}(l_{\rm ant}, m_{\rm ant}) = \eta_{\rm mut}(l_{\max}, m_{\max}; l_{\rm ant}, m_{\rm ant})\eta'_{\rm ant}(l_{\rm ant}, m_{\rm ant})\Omega_{\rm rx}\lambda^2\frac{I_{\nu,\rm ps}}{\Omega_{\rm rx}}. \tag{2.33}$$

$$T_{\rm A,ps}(l_{\rm ant}, m_{\rm ant}) = 2\eta_{\rm mut}(l_{\max}, m_{\max}; l_{\rm ant}, m_{\rm ant})\eta'_{\rm ant}(l_{\rm ant}, m_{\rm ant})\Omega_{\rm rx}\frac{J_{\nu,\rm ps}}{\Omega_{\rm rx}}. \tag{2.34}$$

Compared to Equation (2.18), Equation (2.34) shows that antenna response to an infinitesimal source with radiation temperature $J_{\nu,\rm ps}$ located at the direction of an antenna maximum sensitivity is equivalent to antenna response to an isotropic distribution $J_{\nu,\rm ps}/\Omega_{\rm rx}$.

2.3 Derivative Parameters

The receiving beam pattern $P_{{\rm n},\nu}(\theta, \phi)$ and the effective aperture area $A_{\rm eff}(\theta, \phi)$ that are defined in Section 2.2 describe the performance of an antenna. They can be regarded as the most fundamental parameters of an antenna. Other parameters can be derived from the two parameters, $P_{{\rm n},\nu}(\theta, \phi)$ and $A_{\rm eff}(\theta, \phi)$, and are introduced (cf., Balanis 2005; Stutzman & Thiele 2012; Rohlfs & Wilson 2004; Kraus 1966). In this section, the direction of an antenna, $(\theta_{\rm ant}, \phi_{\rm ant})$, is omitted.

2.3.1 Receiving Beam Solid Angle

A receiving beam solid angle $\Omega_{\rm rx}$ has been already defined in Equation (2.19). $\Omega_{\rm rx}$ gives the extent of an antenna sensitivity. An antenna having a small receiving beam solid angle can receive only a signal from certain ranges of θ and ϕ. If an antenna has an isotropic sensitivity, a receiving beam solid angle is 4π that is the maximum.

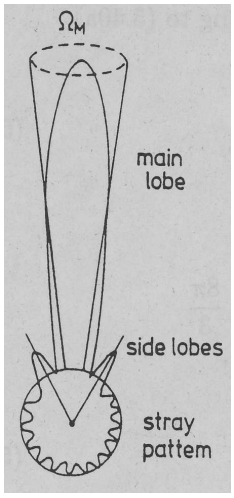

Figure 2.2: A receiving beam pattern. It is resolved into the main lobe, the side lobes, and the stray pattern (Rohlfs & Wilson 2004).

2.3.2 Main Beam

In most cases of astronomical antennas, the normalized beam pattern $P_{\mathrm{n},\nu}(\theta,\phi)$ is nearly unity for a particular direction, otherwise $P_{\mathrm{n},\nu}(\theta,\phi) \simeq 0$. The range of $P_{\mathrm{n},\nu}(\theta,\phi) \simeq 1$ is called a main beam or main lobe. The other range where an antenna is less sensitive is called side lobes or back lobes. Each of back lobes and side lobes far from main lobe is hardy distinguished, so that they form a stray pattern (Figure 2.2). Far side lobes and back lobes are partly caused by stray light.

In analogy to a receiving beam solid angle, a main beam solid angle can be introduced.

$$\Omega_{\mathrm{rx,MB}} := \iint_{\mathrm{MB}} P_{\mathrm{n},\nu}(\theta,\phi)\mathrm{d}\Omega. \tag{2.35}$$

A main beam solid angle $\Omega_{\mathrm{rx,MB}}$ corresponds to energy entering an antenna through a main beam. A main beam efficiency is also introduced as

$$\eta_{\mathrm{rx,MB}} := \frac{\Omega_{\mathrm{rx,MB}}}{\Omega_{\mathrm{rx}}}. \tag{2.36}$$

2.3.3 Beam Width

Half power beam width (HPBW) is a parameter which indicates angular extent of the main beam. HPBW appears frequently because it gives the information on the spatial resolution of celestial objects which are observed. The definition of HPBW is the angle between the points θ'_1 and θ'_2 such that $P'_{\mathrm{n},\nu}(\theta'_1,\phi'_1) = P'_{\mathrm{n},\nu}(\theta'_2,\phi'_1+\pi) = 0.5$. The definition of $P'_{\mathrm{n},\nu}$ is referred to Equation (2.1). HPBW is also called full width to half power. If the beam pattern $P'_{\mathrm{n},\nu}$ has an axial symmetry around the axis $(\theta',\phi') = (0,0)$, HPBW is independent of ϕ'_1.

2.3.4 Directivity and Gain

As a parameter representing how an antenna sensitivity is concentrated toward a specific direction, directivity D can be defined as

$$\begin{aligned} D(\theta,\phi) &:= \frac{4\pi P_{\mathrm{n},\nu}(\theta,\phi)}{\Omega_{\mathrm{rx}}\cos\theta} = \frac{4\pi P_{\nu}(\theta,\phi)\cos\Theta}{\Omega_{\mathrm{rx}} P_{\nu}(\Theta,\Phi)\cos\theta}, \\ \tilde{D}(l,m) &:= \frac{4\pi \tilde{P}_{\mathrm{n},\nu}(l,m)}{\Omega_{\mathrm{rx}}} = \frac{4\pi \tilde{P}_{\nu}(l,m)}{\Omega_{\mathrm{rx}}\tilde{P}_{\nu}(l_{\max},m_{\max})}. \end{aligned} \tag{2.37}$$

Directivity can be determined via the measurement of the beam pattern. Another parameter similar to directivity is also introduced. It is called gain, defined as

$$\begin{aligned} G(\theta,\phi) &:= \frac{4\pi A_{\mathrm{eff}}(\theta,\phi)}{\lambda^2} = \eta_{\mathrm{ant}}\frac{4\pi P_{\mathrm{n},\nu}(\theta,\phi)}{\Omega_{\mathrm{rx}}\cos\theta}, \\ \tilde{G}(l,m) &:= \frac{4\pi \tilde{A}_{\mathrm{eff}}(l,m)}{\lambda^2} = \eta_{\mathrm{ant}}\frac{4\pi \tilde{P}_{\mathrm{n},\nu}(l,m)}{\Omega_{\mathrm{rx}}}. \end{aligned} \tag{2.38}$$

By using the gain in Equation (2.38), Equation (2.32) is transformed into

$$T_{\mathrm{A,ps}} = 2\eta_{\mathrm{mut}}(l_{\mathrm{ps}},m_{\mathrm{ps}})\tilde{G}(l_{\mathrm{ps}},m_{\mathrm{ps}})\frac{J_{\nu,\mathrm{ps}}}{4\pi}. \tag{2.39}$$

Gain can be determined in receiving an isotropic radiation. The antenna temperature $T_{\mathrm{A,ps}}$ can be regarded as the radiation temperature $J_{\nu,\mathrm{ps}}/4\pi$ magnified by the gain $\tilde{G}(l_{\mathrm{ps}},m_{\mathrm{ps}})$.

Kraus (1966) regarded η_{ant} as antenna losses, especially an ohmic loss. In the next chapter, it is revealed what η_{ant} can include.

2.3.5 Aperture Efficiency

In case of an antenna having an physical aperture, the ratio of an effective aperture area to the physical area of an aperture can be considered. It is called an aperture efficiency, which is defined as

$$\eta_{\mathrm{A}}(l,m) := \frac{\tilde{A}_{\mathrm{eff}}(l,m)}{A_{\mathrm{phys}}} = \eta_{\mathrm{ant}}\frac{\lambda^2\tilde{P}_{\mathrm{n},\nu}(l,m)}{A_{\mathrm{phys}}\Omega_{\mathrm{rx}}}. \tag{2.40}$$

By using Equation (2.40), Equations (2.31) is transformed into

$$W_{\nu,\mathrm{ps}} = \eta_{\mathrm{mut}}(l_{\mathrm{ps}},m_{\mathrm{ps}})\eta_{\mathrm{A}}(l_{\mathrm{ps}},m_{\mathrm{ps}})A_{\mathrm{phys}}I_{\nu,\mathrm{ps}}. \tag{2.41}$$

2.4 Reciprocity and Characteristic Parameters of an Antenna

It is known that reciprocity can be observed in many physical phenomena. Reciprocity applied to a system including radiation and an antenna was discussed by Carson (1924, 1930).

2.4.1 Reciprocal Theorem

Let there be two antenna A_1 and A_2 located at the far field of each other. Two cases are considered:

1. An electric field $\boldsymbol{E}_1(\boldsymbol{r}_{\mathrm{A}_1})$ impressed to the antenna A_1 produces a current $\boldsymbol{J}_1(\boldsymbol{r}_{\mathrm{A}_2})$ on the antenna A_2.

2. An electric field $\boldsymbol{E}_2(\boldsymbol{r}_{\mathrm{A}_2})$ impressed to the antenna A_2 produces a current $\boldsymbol{J}_2(\boldsymbol{r}_{\mathrm{A}_1})$ on the antenna A_1.

If it is assumed that the media between the antennas are linear conducting and dielectric ones, that current is proportional to electric field (Ohm's law), and that magnetic matter is excluded, Carson (1924), which used the retarded potentials, showed the reciprocal theorem as follows:

$$\int_{V_1} \boldsymbol{E}_1(\boldsymbol{r}_{\mathrm{A}_1}) \cdot \boldsymbol{J}_2^*(\boldsymbol{r}_{\mathrm{A}_1}) \mathrm{d}V_1 = \int_{V_2} \boldsymbol{E}_2(\boldsymbol{r}_{\mathrm{A}_2}) \cdot \boldsymbol{J}_1^*(\boldsymbol{r}_{\mathrm{A}_2}) \mathrm{d}V_2. \tag{2.42}$$

Note that $*$ represents a complex conjugate. V_1 is the volume including the antenna A_1, the point $\boldsymbol{r}_{\mathrm{A}_1}$ is included in V_1, and V_2 and $\boldsymbol{r}_{\mathrm{A}_2}$ are similar parameters for the antenna A_2. Equation (2.42) can be also interpreted as the case where a current $\boldsymbol{J}_2(\boldsymbol{r}_{\mathrm{A}_1})$ supplied to the antenna A_1 produces an electric field $\boldsymbol{E}_2(\boldsymbol{r}_{\mathrm{A}_2})$ on the antenna A_2, and vice versa.

The application of Equation (2.42) is demonstrated. Figure 2.3 shows the model consisting of two capacitors as antennas. The capacitor as an antenna A_1 has a thickness of d_1 and an area of S_1. The other capacitor as an antenna A_2 has, as well as the antenna A_1, a thickness of d_2 and an area of S_2. For simplicity, the quantities in the capacitors A_1 and A_2, i.e., field, current, permittivity, and permeability, are assumed to be uniform. In addition, the fields and the currents in the capacitors should be normal to conductors constituting the capacitors. Thus, Equation (2.42) can be calculated and the relation among the fields and the currents, $\boldsymbol{E}_1$, $\boldsymbol{E}_2$, $\boldsymbol{J}_1$, and $\boldsymbol{J}_2$, is obtained.

$$|\boldsymbol{E}_1| d_1 \cdot |\boldsymbol{J}_2| S_1 = |\boldsymbol{E}_2| d_2 \cdot |\boldsymbol{J}_1| S_2. \tag{2.43}$$

$|\boldsymbol{E}_1| d_1$ corresponds to an impressed voltage $E_1(1)$ at the antenna A_1 and $|\boldsymbol{J}_1| S_2$ corresponds to an induced current $J_1(2)$ at the antenna A_2. Quantities $|\boldsymbol{E}_2| d_2$ and $|\boldsymbol{J}_2| S_1$ are also interpreted as a voltage $E_2(2)$ and a current $J_1(2)$, respectively, as well as $E_1(1)$ and $J_1(2)$. Then, Equation (2.43)

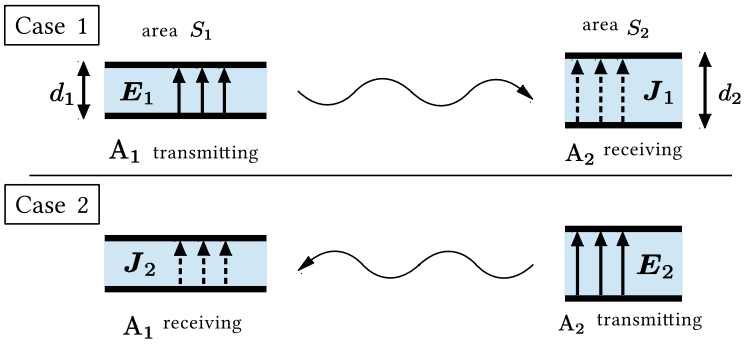

Figure 2.3: Reciprocity.

reduces to

$$E_1(1)J_2(1) = E_2(2)J_1(2). \tag{2.44}$$

One can introduce a transmission line equivalent to the model composed of the two capacitors working as a transmitting antenna and a receiving antenna, respectively (Figure 2.4). Impedance Z_{ij} is defined as the ratio of a voltage $E(i)$ at a port i to a current $J(j)$ at a port j. By using impedances Z_{12} and Z_{21},

$$E_1(1) = Z_{12}J_1(2), \qquad E_2(2) = Z_{21}J_2(1). \tag{2.45}$$

By using Equations (2.45), the reciprocal theorem (2.42) is equivalent to the case where the impedances are equal, i.e., $Z_{12} = Z_{21}$. In more general, if E_i and J_i are a voltage and a current at a port i, respectively, E_i and J_i are related with

$$\begin{pmatrix} E_1 \\ E_2 \end{pmatrix} = \begin{pmatrix} Z_{11} & Z_{12} \\ Z_{21} & Z_{22} \end{pmatrix} \begin{pmatrix} I_1 \\ I_2 \end{pmatrix}, \tag{2.46}$$

and the reciprocal theorem corresponds to $Z_{12} = Z_{21}$. When each Z_{ij} has the same value as Z_χ, Z_χ is called characteristic impedance.

2.4.2 Application to Beam Pattern

The parameters characterizing antenna performance which are introduced in Section 2.3 is based on the receiving pattern $P_{\mathrm{n},\nu}(\theta, \phi)$. The reciprocal theorem (2.42) refers to the relation between an electric field and a current, not to power. Reciprocity with respect to energy represents that the ratio of power received through an antenna 1 to power emitted from an antenna 2 is the same as the ratio of power received through the antenna 2 to power emitted from the antenna 1. Carson

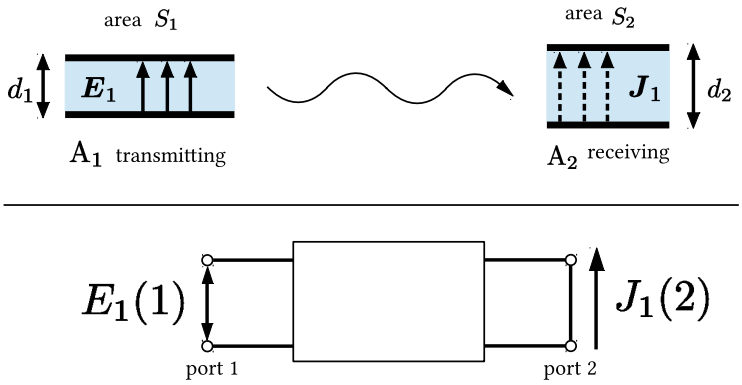

Figure 2.4: A transmission-line model corresponding to the case 1 in Figure 2.3.

(1930) showed the conditions in which the reciprocity with respect to energy holds.

Consider a system consisting of a source, an antenna, and a receiver. Figure 2.5 shows an equivalent transmission-line model to the system. The impedances of the point source, the antenna, and the receiver are assumed to be $Z_{\rm src} = R_{\rm src} + \sqrt{-1}\,X_{\rm src}$, $Z_{\rm ant} = R_{\rm ant} + \sqrt{-1}\,X_{\rm ant}$, and $Z_{\rm rx} = R_{\rm rx} + \sqrt{-1}\,X_{\rm rx}$, respectively. R and X denote resistance and reactance, respectively. $Z_{\rm src}$ and $Z_{\rm rx}$ are given as characteristic impedance and $Z_{\rm ant}$ is given by

$$Z_{\rm ant} = \begin{pmatrix} Z_{11} & Z_{12} \\ Z_{21} & Z_{22} \end{pmatrix} = \begin{pmatrix} R_{11} & R_{12} \\ R_{21} & R_{22} \end{pmatrix} + \sqrt{-1} \begin{pmatrix} X_{11} & X_{12} \\ X_{21} & X_{22} \end{pmatrix}. \tag{2.47}$$

E in Figure 2.5 is electromotive force, which is used as a common source at the source and the receiver. E induces the current $J_{\rm rx}$ at the receiver and the current $J_{\rm src}$ at the source. The case considered in Section 2.2.1 where the receiving beam pattern is discussed corresponds to the receiving case in Figure 2.5. In the receiving case, the currents $J_{\rm rx}$ and $J_{\rm src}$ are calculated as functions of E and the impedances.

$$\begin{pmatrix} J_{\rm src} \\ J_{\rm rx} \end{pmatrix} = \frac{E}{(Z_{\rm src} + Z_{11})(Z_{\rm rx} + Z_{22}) - Z_{12}Z_{21}} \begin{pmatrix} Z_{\rm rx} + Z_{22} \\ -Z_{21} \end{pmatrix}. \tag{2.48}$$

The ratio of the energy consumed at the receiver, $P_{\rm rx} = R_{\rm rx}|J_{\rm rx}|^2$, to the energy emitted from the source, $P_{\rm src} = (R_{\rm src} + {R_{11}}^{\rm C})|J_{\rm src}|^2$, is obtained,

$$\frac{P_{\rm rx}}{P_{\rm src}} = \frac{R_{\rm rx}}{R_{\rm src} + {R_{11}}^{\rm C}} \frac{|Z_{21}|^2}{|Z_{\rm rx} + Z_{22}|^2}, \tag{2.49}$$

$$ {Z_{11}}^{\rm C} = {R_{11}}^{\rm C} + \sqrt{-1}{X_{11}}^{\rm C} \qquad := Z_{11} - \frac{Z_{12}Z_{21}}{Z_{\rm rx} + Z_{22}}. \tag{2.50}$$

In the transmitting case, the ratio of the energy consumed at the source, $P'_{\rm src} = R_{\rm src}|J'_{\rm src}|^2$, to the

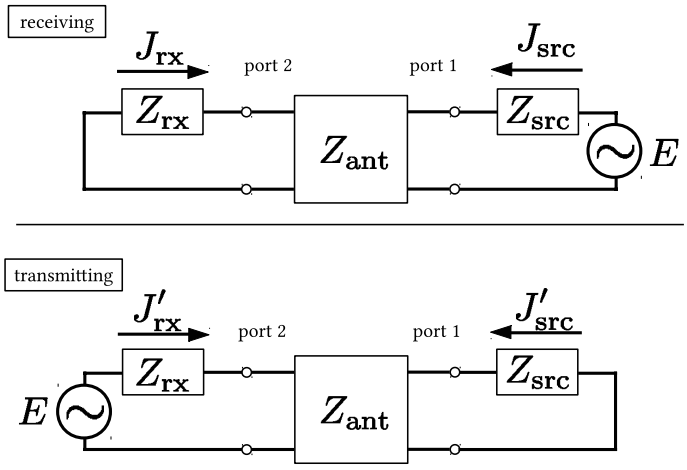

Figure 2.5: An equivalent transmission line.

energy emitted from the receiver, $P'_{\mathrm{rx}} = (R_{\mathrm{rx}} + {R_{22}}^{\mathrm{C}})|J'_{\mathrm{rx}}|^2$, is obtained in a similar way,

$$\frac{P'_{\mathrm{src}}}{P'_{\mathrm{rx}}} = \frac{R_{\mathrm{src}}}{R_{\mathrm{rx}} + {R_{22}}^{\mathrm{C}}} \frac{|Z_{12}|^2}{|Z_{\mathrm{src}} + Z_{11}|^2}, \tag{2.51}$$

$${Z_{22}}^{\mathrm{C}} = {R_{22}}^{\mathrm{C}} + \sqrt{-1}{X_{22}}^{\mathrm{C}} \qquad := Z_{22} - \frac{Z_{12}Z_{21}}{Z_{\mathrm{src}} + Z_{11}}. \tag{2.52}$$

According to Carson (1930), if the reciprocal theorem holds, i.e., $Z_{12} = Z_{21} =: Z_\chi$, the conditions for the reciprocal energy theorem, $P_{\mathrm{rx}}/P_{\mathrm{src}} = P'_{\mathrm{src}}/P'_{\mathrm{rx}}$, are

$$Z_{\mathrm{src}} = {Z_{11}^*}^{\mathrm{C}} = Z_{11}^* - \frac{\left(Z_\chi^*\right)^2}{Z_{\mathrm{rx}}^* + Z_{22}^*}, \tag{2.53}$$

$$Z_{\mathrm{rx}} = {Z_{22}^*}^{\mathrm{C}} = Z_{22}^* - \frac{\left(Z_\chi^*\right)^2}{Z_{\mathrm{src}}^* + Z_{11}^*}. \tag{2.54}$$

These conditions (2.53) and (2.54) not only make the ratios $P_{\mathrm{rx}}/P_{\mathrm{src}}$ and $P'_{\mathrm{src}}/P'_{\mathrm{rx}}$ equal to each other but also maximize them (Carson 1930; Silver 1949). By applying the reciprocal energy theorem to the measurement of energy from a point source located at direction (θ, ϕ), the ratio of antenna output power $P_\nu(\theta, \phi)\,\mathrm{d}\nu$ to brightness $I_{\nu,\mathrm{ps}}\,\mathrm{d}\nu$ is the same value as the ratio of energy reaching to the point source to energy invested in the antenna. Because reciprocity holds independently of direction (θ, ϕ), the receiving beam pattern of an antenna, $P_{\mathrm{n},\nu}(\theta, \phi)$, is the same as a transmitting beam pattern of the antenna. The antenna efficiency η_{ant} for a receiving antenna in Equation (2.20) also corresponds to that for a transmitting antenna. The properties of a receiving antenna can be predicted by the properties of it when it works as a transmitting antenna.

The reciprocity of an antenna and the reciprocal energy theorem are hereafter assumed, and therefore, the parameters appearing in Sections 2.2 and 2.3 can be described using a transmitting beam pattern.

2.5 Summary

Parameters which represent the properties of an antenna are described in this chapter. A receiving beam pattern defined in Equation (2.1) is one of the most fundamental parameters, which can be measured when a point source is observed. Another fundamental parameter is an effective aperture area defined in Equation (2.22), which can be also measured. An effective aperture area is proportional to the product of two quantities: the efficiency of an antenna, which is measured in observing an isotropic and non-polarized source, and a receiving beam pattern. These two parameters determines the properties of an antenna completely, so that other parameters are derived from them. Reciprocity is a useful concept when one predicts the properties of an antenna.

3

Antenna with Aperture

3.1 Introduction

The aim of this chapter is to describe explicitly the efficiency η_{ant} for an aperture antenna by assuming reciprocity and to demonstrate how to design the optical system of a single-beam radio telescope until now.

All of the antennas taken into account in this chapter are assumed to have an aperture. Antennas in this chapter may have optical elements, e.g., lenses and mirrors. A mirror is identified with a corresponding lens because a mirror plays the same role as and can be replaced with a lens. Discussion is developed at a specific frequency ν with a bandwidth $\mathrm{d}\nu$.

3.2 Transmitter-Antenna-Receiver System

3.2.1 Finite Distance between Transmitter and Receiver

Before a radio telescope with an aperture is discussed, consider a simple system consisting of a transmitter, a lens which plays the role of an antenna with an aperture, and a receiver, shown in Figure 3.1, to clarify the meaning of the antenna efficiency η_{ant} in Equation (2.20).

In Case 1 in Figure 3.1, let energy transmitted by the transmitter and energy received by the receiver be W_1^{tx} and W_1^{rx}, respectively. An electromagnetic wave leaving the transmitter reaches the lens but part of the wave cannot go through it. This phenomenon is called spillover. Spillover efficiency $\eta_{\mathrm{sp},1}^{\mathrm{tx}}$ is introduced as the ratio of energy which can enter the lens to the transmitted energy W_1^{tx}. The lens sends the entering energy into the opposite space to the transmitter, part of which can be transferred toward the receiver. The ratio of the energy toward the receiver to the entering energy can be considered and is represented by optical efficiency $\eta_{\mathrm{opt},1}$. The optical efficiency $\eta_{\mathrm{opt},1}$ is a function of the relative positions of the transmitter and the receiver to the lens. The energy toward the receiver after the lens reaches the receiver but the receiver cannot receive all the energy. One of the reasons to reduce the received energy is efficiency determined by the properties of both the transmitter and the receiver, such as polarization. This efficiency corresponds to η_{mut} in Equation (2.9). Other reasons, such as receiver efficiency, can be also considered, so that let $\eta'_{\mathrm{other},1}$ represent the efficiency originating from other factors. Thus, the energy received by the receiver is expressed as

$$W_1^{\mathrm{rx}} = \eta'_{\mathrm{other},1}\eta_{\mathrm{mut}}\eta_{\mathrm{opt},1}\eta_{\mathrm{sp},1}^{\mathrm{tx}}W_1^{\mathrm{tx}}. \tag{3.1}$$

In Case 2 in Figure 3.1, a similar equation to Equation (3.1) can be obtained by exchanging the

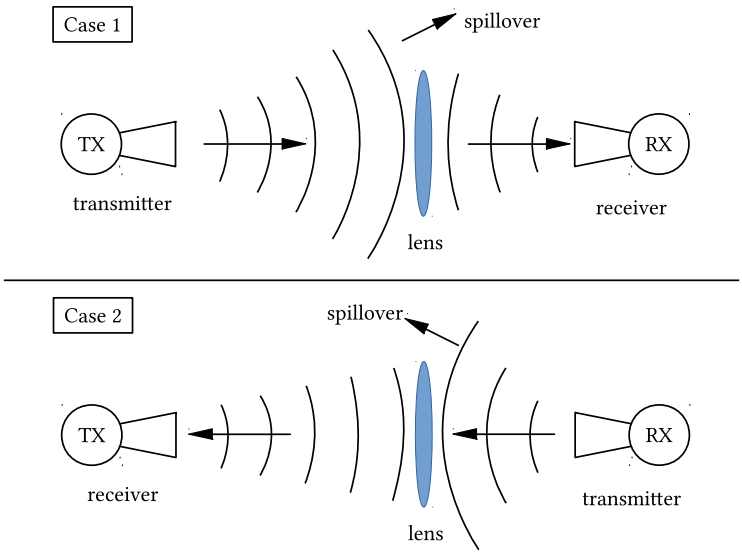

Figure 3.1: Transmitter-Antenna-Receiver System. According to the reciprocal energy theorem, the ratio of received energy to transmitted energy is the same in both cases 1 and 2.

roles between the transmitter and the receiver.

$$W_2^{\mathrm{tx}} = \eta'_{\mathrm{other},2}\eta_{\mathrm{mut}}\eta_{\mathrm{opt},2}\eta_{\mathrm{sp},2}^{\mathrm{rx}}W_2^{\mathrm{rx}}. \tag{3.2}$$

Note that η_{mut} is independent of the direction of propagation. In accordance with the reciprocity of each component and the reciprocal energy theorem,

$$\eta_{\mathrm{opt},1} = \eta_{\mathrm{opt},2}, \tag{3.3}$$

$$\eta'_{\mathrm{other},1}\eta_{\mathrm{mut}}\eta_{\mathrm{opt},1}\eta_{\mathrm{sp},1}^{\mathrm{tx}} = \eta'_{\mathrm{other},2}\eta_{\mathrm{mut}}\eta_{\mathrm{opt},2}\eta_{\mathrm{sp},2}^{\mathrm{rx}}. \tag{3.4}$$

If $\eta'_{\mathrm{other},1} = \eta_{\mathrm{other}}^{\mathrm{rx}}\,\eta_{\mathrm{other}}^{\mathrm{tx}}\,\eta_{\mathrm{sp},2}^{\mathrm{rx}}$ and $\eta'_{\mathrm{other},2} = \eta_{\mathrm{other}}^{\mathrm{rx}}\,\eta_{\mathrm{other}}^{\mathrm{tx}}\,\eta_{\mathrm{sp},1}^{\mathrm{tx}}$, Equations (3.1) and (3.2) can be rewritten regardless of Case 1 and 2:

$$W^{\mathrm{rx}} = \eta_{\mathrm{mut}}\,\eta_{\mathrm{sp}}^{\mathrm{rx}}\,\eta_{\mathrm{other}}^{\mathrm{rx}}\,\eta_{\mathrm{opt}}\,\eta_{\mathrm{other}}^{\mathrm{tx}}\,\eta_{\mathrm{sp}}^{\mathrm{tx}}\,W^{\mathrm{tx}}. \tag{3.5}$$

When $\eta_{\mathrm{other}}^{\mathrm{rx}} = \eta_{\mathrm{other}}^{\mathrm{tx}} = 1$, Equation (3.5) reduces to

$$W^{\mathrm{rx}} = \eta_{\mathrm{mut}}\,\eta_{\mathrm{sp}}^{\mathrm{rx}}\,\eta_{\mathrm{opt}}\,\eta_{\mathrm{sp}}^{\mathrm{tx}}\,W^{\mathrm{tx}}. \tag{3.6}$$

η_{opt} represents the correlation between energy from the transmitter and sensitivity of the receiver, i.e., η_{opt} can be regarded as coupling efficiency between the transmitted beam and the receiver sensitivity, as pointed out by Nagai & Imada (2016).

Figure 3.2 shows an equivalent transmission line to the model in Figure 3.1. Each component is linear and the reciprocity holds. $Z_{\rm tx}$ and $Z_{\rm rx}$ are characteristic impedances including the properties of the media among the lens, the transmitter, and the receiver. Each impedance matrix is given by

$$\begin{pmatrix} E^{\rm tx} \\ -(E^{\rm tx}_{\rm lens})^* \\ -(E^{\rm tx}_{\rm L})^* \end{pmatrix} = Z^{\rm tx}_{\rm sp} \begin{pmatrix} J^{\rm tx} \\ -(J^{\rm tx}_{\rm lens})^* \\ -(J^{\rm tx}_{\rm L})^* \end{pmatrix} = \begin{pmatrix} Z^{\rm tx}_{{\rm sp},11} & Z^{\rm tx}_{{\rm sp},12} & Z^{\rm tx}_{{\rm sp},13} \\ Z^{\rm tx}_{{\rm sp},12} & Z^{\rm tx}_{{\rm sp},22} & 0 \\ Z^{\rm tx}_{{\rm sp},13} & 0 & Z^{\rm tx}_{{\rm sp},33} \end{pmatrix} \begin{pmatrix} J^{\rm tx} \\ -(J^{\rm tx}_{\rm lens})^* \\ -(J^{\rm tx}_{\rm L})^* \end{pmatrix}, \tag{3.7}$$

$$\begin{pmatrix} E^{\rm tx}_{\rm lens} \\ E^{\rm rx}_{\rm lens} \end{pmatrix} = Z_{\rm lens} \begin{pmatrix} J^{\rm tx}_{\rm lens} \\ J^{\rm rx}_{\rm lens} \end{pmatrix} = \begin{pmatrix} Z_{{\rm lens},11} & Z_{{\rm lens},\chi} \\ Z_{{\rm lens},\chi} & Z_{{\rm lens},22} \end{pmatrix} \begin{pmatrix} J^{\rm tx}_{\rm lens} \\ J^{\rm rx}_{\rm lens} \end{pmatrix}, \tag{3.8}$$

$$\begin{pmatrix} E^{\rm rx} \\ -(E^{\rm rx}_{\rm lens})^* \\ -(E^{\rm rx}_{\rm L})^* \end{pmatrix} = Z^{\rm rx}_{\rm sp} \begin{pmatrix} J^{\rm rx} \\ -(J^{\rm rx}_{\rm lens})^* \\ -(J^{\rm rx}_{\rm L})^* \end{pmatrix} = \begin{pmatrix} Z^{\rm rx}_{{\rm sp},11} & Z^{\rm rx}_{{\rm sp},12} & Z^{\rm rx}_{{\rm sp},13} \\ Z^{\rm rx}_{{\rm sp},12} & Z^{\rm rx}_{{\rm sp},22} & 0 \\ Z^{\rm rx}_{{\rm sp},13} & 0 & Z^{\rm rx}_{{\rm sp},33} \end{pmatrix} \begin{pmatrix} J^{\rm rx} \\ -(J^{\rm rx}_{\rm lens})^* \\ -(J^{\rm rx}_{\rm L})^* \end{pmatrix}. \tag{3.9}$$

If an optical system composed of more than one elements has no spillover and its impedance matrix is $Z_{\rm opt}$, $Z_{\rm lens}$ in Equation (3.11) can be replaced with $Z_{\rm opt}$. Consequently, Equation (3.8) can be used for a more complicated antenna than the simple model in Figure 3.1 unless there is spillover between the entrance and the exit of the antenna, which correspond to "pupil" in geometrical optics.

3.2.2 Transmitter infinitely apart from Lens and Receiver

It will be difficult to determine the transmitted energy $W^{\rm tx}$ when the transmitter is located at infinity. In this case, it may be reasonable to use the energy entering through an aperture instead of $W^{\rm tx}$ and to redefine the spillover efficiency $\eta^{\rm tx}_{\rm sp}$ as the ratio of the energy through an aperture stop to the energy though an aperture. An aperture is the opening of the first element of an optical system. On the other hand, an aperture stop, or simply stop, defines the cross section of an electric field which can reach a receiver. The images of stop are called pupil (Born & Wolf 1997, pp. 186–188), which is a fundamental concept in geometrical optics. When an antenna consists of one lens, the aperture stop of the antenna corresponds to its aperture and the spillover efficiency $\eta^{\rm tx}_{\rm sp}$ is unity. When an antenna has a plural components in its optical system, the spillover efficiency $\eta^{\rm tx}_{\rm sp}$ can be less than unity, which often occurs in a wide field-of-view system.

By using the energy passing through an aperture, $W^{\rm ap}$, Equation (3.5) is rewritten as

$$W^{\rm rx} = \eta_{\rm mut}\, \eta^{\rm rx}_{\rm sp}\, \eta_{\rm opt}\, \eta^{\rm tx}_{\rm sp}\, W^{\rm ap}. \tag{3.10}$$

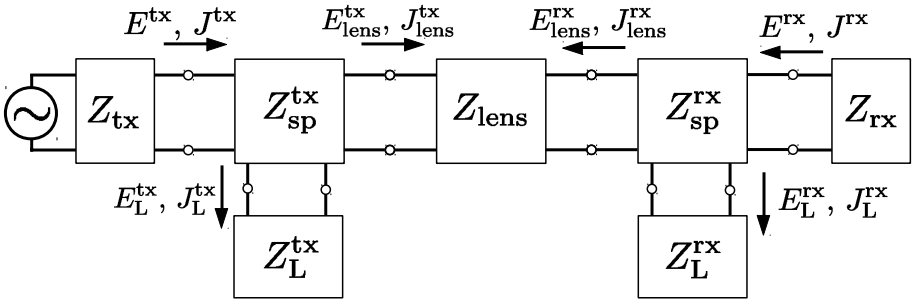

Figure 3.2: An equivalent transmission line to the transmitter-Antenna-Receiver model.

Comparison of Equation (3.10) with Equation (2.31) leads to the following correspondence:

$$W_{\nu,\mathrm{ps}} = W^{\mathrm{rx}}, \qquad I_{\nu,\mathrm{ps}} A_{\mathrm{ap}} = W^{\mathrm{ap}}, \qquad \eta_{\mathrm{ant}} \frac{\lambda^2 \tilde{P}_{\mathrm{n},\nu}}{A_{\mathrm{ap}}\Omega} = \eta^{\mathrm{rx}}_{\mathrm{sp}}\, \eta_{\mathrm{opt}}\, \eta^{\mathrm{tx}}_{\mathrm{sp}}, \tag{3.11}$$

where A_{ap} is the area of an aperture, $\tilde{P}_{\mathrm{n},\nu}$ denotes a receiving and transmitting beam pattern, and Ω a receiving and transmitting beam solid angle. As mentioned above, the position of the transmitter and the receiver determines η_{opt}, so that

$$\eta_{\mathrm{opt}} = \frac{\lambda^2 \tilde{P}_{\mathrm{n},\nu}}{A_{\mathrm{ap}}\Omega}, \qquad \eta_{\mathrm{ant}} = \eta^{\mathrm{tx}}_{\mathrm{sp}}\, \eta^{\mathrm{rx}}_{\mathrm{sp}}. \tag{3.12}$$

In case of an aperture antenna composed of one element, the results of Equation (3.12) transforms the effective aperture area in Equation (2.27) into

$$\tilde{A}_{\mathrm{eff}} = \eta_{\mathrm{ant}} \frac{\lambda^2 \tilde{P}_{\mathrm{n},\nu}}{\Omega} = \eta^{\mathrm{tx}}_{\mathrm{sp}}\, \eta^{\mathrm{rx}}_{\mathrm{sp}}\, \eta_{\mathrm{opt}} A_{\mathrm{ap}}. \tag{3.13}$$

The aperture efficiency in Equation (2.40) is also expressed as

$$\eta_{\mathrm{A}} = \eta^{\mathrm{tx}}_{\mathrm{sp}}\, \eta^{\mathrm{rx}}_{\mathrm{sp}}\, \eta_{\mathrm{opt}} = \eta^{\mathrm{tx}}_{\mathrm{sp}}\, \eta^{\mathrm{rx}}_{\mathrm{sp}} \frac{\lambda^2 \tilde{P}_{\mathrm{n},\nu}}{A_{\mathrm{ap}}\Omega}. \tag{3.14}$$

Equation (3.14) seems different from the literature on a radio telescope, such as Kraus & Marhefka (2002). They described a special case where $\eta^{\mathrm{tx}}_{\mathrm{sp}} = \eta^{\mathrm{rx}}_{\mathrm{sp}} = 1$. Schelkunoff & Friis (1952, p. 565) pointed out that spillover efficiencies should be multiplied to an efficiency and be included in the aperture efficiency. Equation (3.14) is consistent with Schelkunoff & Friis (1952).

3.3 Description Using Gaussian Distribution

In most cases, a receiver used in a radio telescope has sensitivity depending on direction from which electromagnetic wave comes because received energy should be occupied by a signal with

as a large proportion as possible. A Gaussian function is usually adopted as the distribution of sensitivity on the entrance of a receiver. It is well known that an field described by a Gaussian distribution propagates keeping a Gaussian distribution, namely a Gaussian beam, cf. Equation (4.19). The propagation of Gaussian beams including higher modes can be described well by using quasioptics (Goldsmith 1998). Figure 3.3 shows a radio telescope adopted as an example. This radio telescope model consists of a circular lens with a radius of $R_{\rm lens}$ and a receiver whose sensitivity is an axially symmetric Gaussian distribution. If spillover between pupils does not exist, it is sufficient to use a telescope model with one lens, as mentioned after Equation (3.9). It is also assumed that axes of the lens, the receiver, and the sensitivity corresponds to each other, and therefore the whole system from a receiver to a lens, including the axially symmetric sensitivity, has an axial symmetry. The time dependence of a field is assumed to be $\exp(\sqrt{-1}\omega t)$.

3.3.1 Beam Pattern

Because reciprocity is assumed, consider a beam pattern when an antenna is used for a transmitting antenna. The imaginary field which a detector sensitivity induces at an aperture stop is assumed to be

$$E_{\rm ap}(r,\phi) = \begin{cases} \exp\left(-\dfrac{r^2}{w^2}\right) & (r \le R_{\rm lens}) \\ 0 & (r > R_{\rm lens}) \end{cases}, \tag{3.15}$$

where w is the beam size. According to diffraction theory, the electric field at infinity is given as

$$\begin{aligned} E_\infty(\theta,\phi) &= \int_0^{R_{\rm lens}} \int_0^{2\pi} \exp\left(-\frac{r^2}{w^2}\right) \exp\left[-\sqrt{-1}\, kr\sin\theta\cos(\varphi-\phi)\right] r\,\mathrm{d}r\,\mathrm{d}\varphi \\ &= \pi {R_{\rm lens}}^2 \int_0^1 \exp\left(-\alpha\rho^2\right) J_0(\beta\rho)\,\mathrm{d}(\rho^2), \end{aligned} \tag{3.16}$$

where $\rho := r/R_{\rm lens}$, $\alpha := {R_{\rm lens}}^2/w^2$, $\beta := kR_{\rm lens}\sin\theta$, $k := 2\pi/\lambda$, λ is a wavelength, and J_0 is the zeroth-order Bessel function of the first kind. r, θ, ϕ, and φ are defined in Figure 3.4. By extending the Bessel function as a series (Watson 1966, p. 15),

$$\begin{aligned} E_\infty(\theta,\phi) &= \pi {R_{\rm lens}}^2 \sum_{m=0}^{\infty} \frac{(-1)^m}{m!m!} \left(\frac{\beta}{2}\right)^{2m} \int_0^1 \exp\left(-\alpha\rho^2\right) \rho^{2m}\mathrm{d}(\rho^2) \\ &= \pi {R_{\rm lens}}^2 \sum_{m=0}^{\infty} \frac{1}{m!} \left(-\frac{\beta^2}{4\alpha}\right)^m \left(\frac{1}{\alpha} - \frac{\exp(-\alpha)}{\alpha} \sum_{k=0}^{m} \frac{\alpha^k}{k!}\right) \\ &= \frac{\pi {R_{\rm lens}}^2}{\alpha} \left\{ \exp\left(-\frac{\beta^2}{4\alpha}\right) - \exp[-\alpha] \sum_{m=0}^{\infty} \left(-\frac{\beta}{2\alpha}\right)^m J_m(\beta) \right\}. \end{aligned} \tag{3.17}$$

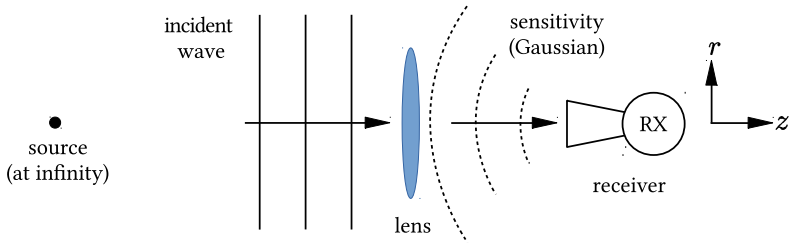

Figure 3.3: A radio telescope model used to calculate parameters.

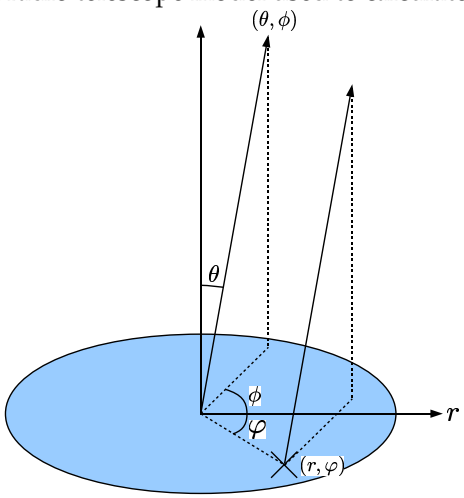

Figure 3.4: Definition of the coordinates r, θ, ϕ, and φ. The blue area represents the lens, i.e., aperture stop.

The generating function of the Bessel function (Watson 1966, pp.14–15) is

$$\exp\left[\frac{z}{2}\left(t-\frac{1}{t}\right)\right] = J_0(z) + \sum_{n=1}^{\infty}\left[t^n + \left(-\frac{1}{t}\right)^n\right] J_n(z), \tag{3.18}$$

and substituting $t = -\beta/(2\alpha)$ and $z = \beta$ into Equation (3.18) yields

$$\exp\left(-\frac{\beta^2}{4\alpha}+\alpha\right) = \sum_{n=0}^{\infty}\left(-\frac{\beta}{2\alpha}\right)^n J_n(\beta) + \sum_{n=1}^{\infty}\left(\frac{2\alpha}{\beta}\right)^n J_n(\beta). \tag{3.19}$$

As a consequence, the electric field at infinity,

$$E_\infty(\theta,\phi) = \pi {R_{\text{lens}}}^2 \frac{\exp(-\alpha)}{\alpha} \sum_{n=1}^{\infty}\left(\frac{2\alpha}{\beta}\right)^n J_n(\beta), \tag{3.20}$$

is obtained. When $(\theta,\phi) = (0,0)$, $|E_\infty(\theta,\phi)|$ is maximized and by Equation (3.17) the maximum is

$$E_\infty(0,0) = \pi {R_{\text{lens}}}^2 \frac{1-\exp(-\alpha)}{\alpha}. \tag{3.21}$$

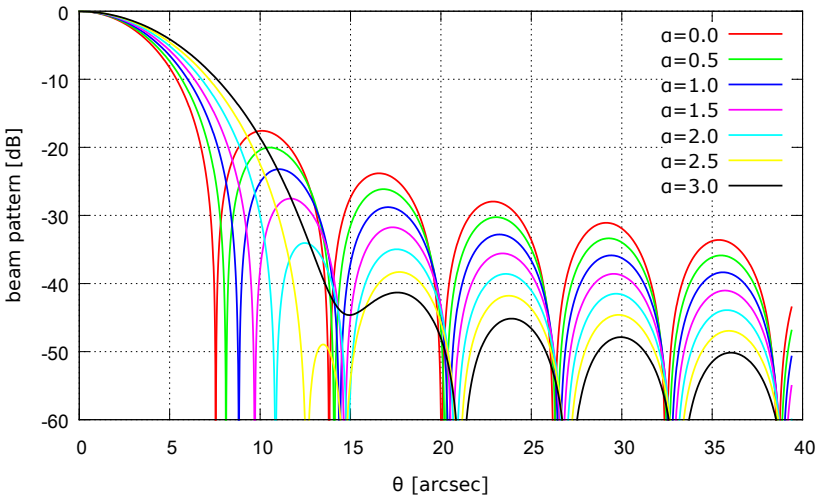

Figure 3.5: Analytically predicted Beam Pattern.

Table 3.1: Several quantities characterinzing beam pattern. For $\alpha = 3.0$, the first local minimum is not null but regarded as a null point.

α	beam width	first side lobe position	first side lobe level	first null point
0.0	$6''.36$	$10''.12$	-17.57 dB	$7''.55$
0.5	$6''.66$	$10''.54$	-20.03 dB	$8''.12$
1.0	$7''.00$	$11''.05$	-23.20 dB	$8''.82$
1.5	$7''.38$	$11''.68$	-27.52 dB	$9''.71$
2.0	$7''.76$	$12''.47$	-34.05 dB	$10''.86$
2.5	$8''.18$	$13''.49$	-48.95 dB	$12''.59$
3.0	$8''.58$	$14''.94$	-44.63 dB	$14''.94$

Thus, the beam pattern is given by

$$P_{\rm n}(\theta,\phi) = \frac{\exp(-2\alpha)}{[1-\exp(-\alpha)]^2} \sum_{n=1}^{\infty}\sum_{m=1}^{\infty} (2\alpha)^{m+n} \frac{J_m(\beta)}{\beta^m}\frac{J_n(\beta)}{\beta^n}. \tag{3.22}$$

Note that $\alpha = {R_{\rm lens}}^2/w^2$ and $\beta = kR_{\rm lens}\sin\theta$. Figure 3.5 shows several beam patterns which are theoretically predicted by Equation (3.22). It is assumed in Figure 3.5 that the wavelength is 300 μm and the radius of the lens, $R_{\rm lens}$, is 5000 mm. A beam width introduced in Section 2.3.3, a first side lobe level, and a first null point can be derived by solving Equation (3.22) numerically. They are shown in Table 3.1.

3.3.2 Beam Solid Angle

A beam solid angle is obtained by the integration of Equation (3.22) over θ and ϕ as shown in Equation (2.19). However, the effect of back lobes cannot be evaluated by Equation (3.22) because the beam pattern $P_{\rm n}(\theta,\phi)$, Equation (3.22), does not include the influence of diffraction by the

edge of the lens and stray light. The ranges of θ and ϕ are here adopted as 0 to $\pi/2$ and 0 to 2π, respectively.

$$\Omega_{\mathrm{A}} = \frac{\exp(-2\alpha)}{[1-\exp(-\alpha)]^2} \sum_{n=1}^{\infty}\sum_{m=1}^{\infty} (2\alpha)^{m+n} \iint_{2\pi} \frac{J_m(\beta)}{\beta^m}\frac{J_n(\beta)}{\beta^n}\mathrm{d}\Omega. \tag{3.23}$$

By assuming $kR_{\mathrm{lens}} \gg 1$, which means that the lens is much bigger than the scale of wavelength, $J_n(\beta)/\beta^n$ will not contribute the integral because $J_n(x)$ behaves such that $|J_n(x)| < \sqrt{2/(\pi x)}$. As a result, only case of $\theta \ll 1$ has to be considered and the range of θ can be replaced by from 0 to infinity. Then,

$$\begin{aligned}
\Omega_{\mathrm{A}} &\simeq \frac{\lambda^2}{\pi {R_{\mathrm{lens}}}^2}\frac{\exp(-2\alpha)}{2[1-\exp(-\alpha)]^2}\sum_{n=1}^{\infty}\sum_{m=1}^{\infty}(2\alpha)^{m+n}\int_0^{\infty}\frac{J_m(\beta)J_n(\beta)}{\beta^{m+n-1}}\mathrm{d}\beta \\
&= \frac{\lambda^2}{\pi {R_{\mathrm{lens}}}^2}\frac{\exp(-2\alpha)}{2\left(1-\exp(-\alpha)\right)^2}2\alpha\sum_{n=1}^{\infty}\sum_{m=1}^{\infty}\frac{\alpha^{m+n-1}}{(m-1)!(n-1)!(m+n-1)} \\
&= \frac{\lambda^2}{\pi {R_{\mathrm{lens}}}^2}\frac{\exp(-2\alpha)}{2\left[1-\exp(-\alpha)\right]^2}2\alpha\sum_{n=0}^{\infty}\sum_{m=0}^{\infty}\frac{\alpha^{n+1}}{(n+1)!}\binom{n}{m} \\
&= \frac{\lambda^2}{\pi {R_{\mathrm{lens}}}^2}\frac{\alpha[1-\exp(-2\alpha)]}{2\left[1-\exp(-\alpha)\right]^2}.
\end{aligned} \tag{3.24}$$

Note that the following formula about the Bessel function is used:

$$\frac{\mathrm{d}}{\mathrm{d}z}\left(\frac{J_{\mu-1}(z)}{z^{\mu-1}}\frac{J_{\nu-1}(z)}{z^{\nu-1}} + \frac{J_{\mu}(z)}{z^{\mu-1}}\frac{J_{\nu}(z)}{z^{\nu-1}}\right) = 2(1-\mu-\nu)\frac{J_{\mu}(z)J_{\nu}(z)}{z^{\mu+\nu-1}}, \tag{3.25}$$

which can be derived by using the relations (Watson 1966, p. 17)

$$J_{\nu-1}(z) + J_{\nu+1}(z) = \frac{2\nu}{z}J_{\nu}(z), \tag{3.26}$$

$$\frac{\mathrm{d}}{\mathrm{d}z}\left[z^{-\nu}J_{\nu}(z)\right] = -z^{-\nu}J_{\nu+1}(z). \tag{3.27}$$

By rearranging Equation (3.24), the beam solid angle, the area of an aperture stop, and the wavelength are connected by the parameter $\alpha = {R_{\mathrm{lens}}}^2/w^2$.

$$\frac{\lambda^2}{\pi {R_{\mathrm{lens}}}^2\,\Omega_{\mathrm{A}}} = \frac{2\left[1-\exp(-\alpha)\right]^2}{\alpha[1-\exp(-2\alpha)]}. \tag{3.28}$$

Note that Equation (3.28) corresponds to the optical efficiency in Equation (3.12) η_{opt}, or coupling efficiency, when $\tilde{P}_{\mathrm{n}} = 1$.

3.3.3 Spillover

When the source is located at infinity and the aperture plays the role of an aperture stop, the spillover efficiency on the side of the source, $\eta_{\rm sp}^{\rm tx}$, is unity. This situation often occurs and is regarded as a common case until now. The spillover efficiency on the side of the receiver, $\eta_{\rm sp}^{\rm rx}$, can be given by calculating the energy of an electromagnetic field on the aperture and the whole energy to be detected by the receiver, i.e., $\eta_{\rm sp}^{\rm rx}$ can be also derived from Equation (3.15).

$$\eta_{\rm sp}^{\rm rx} = \frac{\iint_{\rm ap} E_{\rm ap}(r,\varphi) E_{\rm ap}^{*}(r,\varphi) r {\rm d}r{\rm d}\varphi}{\iint_{\infty} E_{\rm ap}(r,\varphi) E_{\rm ap}^{*}(r,\varphi) r {\rm d}r{\rm d}\varphi} = 1 - \exp(-2\alpha), \tag{3.29}$$

where α is the same parameter as seen in the previous section, $\alpha = {R_{\rm lens}}^2/w^2$. Note that the spillover efficiency on the side of the receiver is determined only by the receiver sensitivity and the spillover efficiency on the side of the source is in the same way determined only by the field produced by the source.

3.3.4 Aperture Efficiency

Through Sections 3.3.1 to 3.3.3, Equation (3.14) can be explicitly written with the parameter of the receiver sensitivity, α, as follows:

$$\begin{aligned}\eta_{\rm A}(l,m) &= \eta_{\rm sp}^{\rm tx}\,\eta_{\rm sp}^{\rm rx}\,\eta_{\rm opt} = \eta_{\rm sp}^{\rm tx}\,\eta_{\rm sp}^{\rm rx}\,\frac{\lambda^2 P_{{\rm n},\nu}}{A_{\rm ap}\Omega} \\ &= \frac{2\exp(-2\alpha)}{\alpha}\sum_{n=1}^{\infty}\sum_{m=1}^{\infty}(2\alpha)^{m+n}\frac{J_m(\beta)}{\beta^m}\frac{J_n(\beta)}{\beta^n},\end{aligned} \tag{3.30}$$

where $\alpha = {R_{\rm lens}}^2/w^2$ and $\beta = kR_{\rm lens}\sin\theta$. Note that when $\beta = 0$ the summation becomes

$$\sum_{n=1}^{\infty}\sum_{m=1}^{\infty}(2\alpha)^{m+n}\frac{J_m(\beta)}{\beta^m}\frac{J_n(\beta)}{\beta^n}\bigg|_{\beta=0} = \exp(2\alpha)[1-\exp(-\alpha)]^2. \tag{3.31}$$

In this case, the aperture efficiency which has been used for a long time is obtained,

$$\eta_{\rm A,trad} := \eta_{\rm A}(0,0) = \frac{2[1-\exp(-\alpha)]^2}{\alpha}, \tag{3.32}$$

which can be seen in, e.g., Goldsmith (1998, Section 6.3). Figure 3.6 shows Equation (3.32) as a function of the parameter $\alpha = {R_{\rm lens}}^2/w^2$. The optical efficiency in Equation (3.28), or coupling efficiency, and the spillover efficiency in Equation (3.29) are also shown. $\eta_{\rm A,trad}$ has the maximum of about 0.8 at $\alpha \simeq 1.58$.

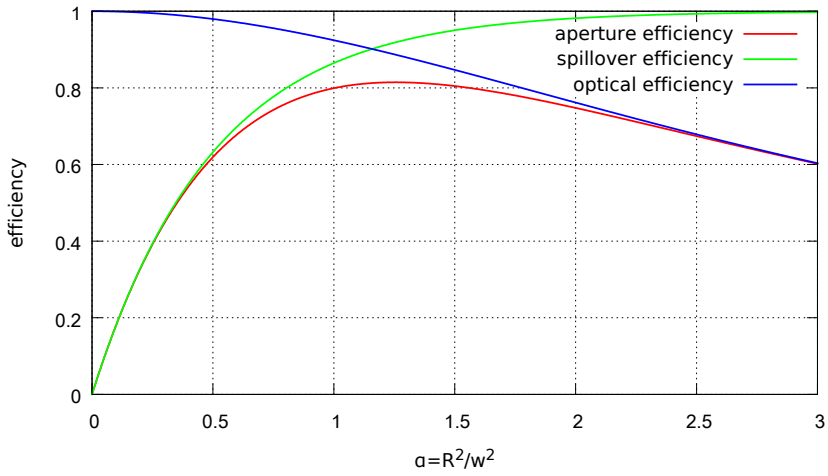

Figure 3.6: The aperture efficiency as a function of α. The spillover efficiency (green line) and the optical efficiency (blue line) are also plotted.

3.4 Design of Classical Cassegrain Antenna

As demonstrated in Chapter 2, some parameters charactering an antenna are important to design the optical system of a radio telescope. The requirements to design a radio telescope are ultimately the following two points.

1. An aperture efficiency is not dependent on operating frequency.
2. An aperture efficiency is as high as possible.

Requirement 1 arises from a wide bandwidth in operation. Requirement 2 determines the efficiency of observation. In this section, one of the way to design a radio telescope is introduced and where to be improved for a wide field-of-view telescope is discussed.

3.4.1 System Independent of Frequency

When a radio telescope composed of several lenses, the amplitude distribution and the phase of a beam varies depending on the distance of propagation and the frequency of the beam. In case of an on-axis fundamental Gaussian beam, Chu (1983) proved that there are certain positions where the amplitude distribution and the wavefront are independent of frequency and determined only by the geometry of an optical system.

According to Chu (1983), the amplitude and the wavefront of an on-axis beam are converted into other amplitude and wavefront, respectively, independently of frequency at the positions where the lens formula holds. Consider the system shown in Figure 3.7. An on-axis fundamental Gaussian beam enters the lens with a focal length of f from the left, passes through the lens, and

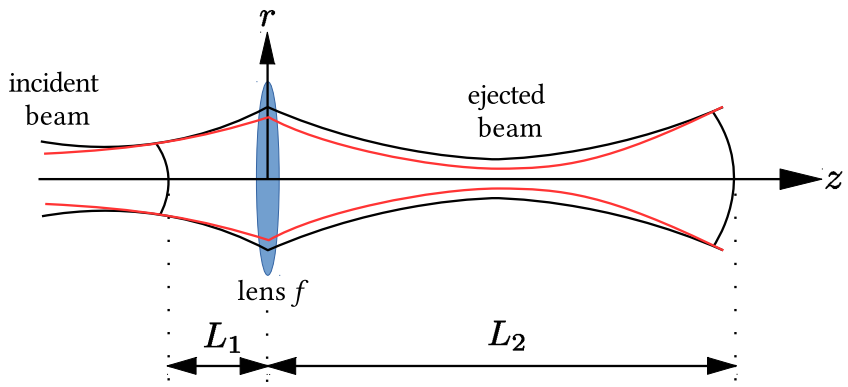

Figure 3.7: A fundamental Gaussian beam passing though a lens. The black line represents a beam with a frequency of f_1 and the red one with another frequency f_2.

goes out of the lens to the right. Focus on the two positions, $z = -L_1$ and $z = L_2$, which meet the lens formula, i.e.,

$$\frac{1}{f} = \frac{1}{L_1} + \frac{1}{L_2}. \tag{3.33}$$

Let the beam sizes at $z = -L_1$ and L_2 be w_1 and w_2, respectively. In the same way as the beam sizes, the radii of curvature of wavefront are r_1 and r_2, respectively. Note that the radius of curvature of wavefront is positive when the wavefront is convex seen from the negative part of the z axis. The beam sizes, w_1 and w_2, are related to each other as follows:

$$\frac{w_1}{w_2} = \frac{L_1}{L_2}, \tag{3.34}$$

As well as the beam size, the radii of curvature of the wavefront, r_1 and r_2, are related.

$$-L_1 \left(1 - \frac{L_1}{r_1}\right) = L_2 \left(1 + \frac{L_2}{r_2}\right). \tag{3.35}$$

Equations (3.34) and (3.35) are independent of frequency and indicate that the properties of beams are determined only by the geometry of the system. These relations are useful to design an optical system of a single-beam telescope.

Consider application to designing a single-beam radio telescope consisting of a few lenses (Figure 3.8). There are premises to make a telescope work as a telescope. The radius of curvature of the wavefront at an aperture is infinity because an incident wave from celestial objects is a plane wave. At the same time, the beam size at an aperture stop has to be required to be independent of frequency. An aperture efficiency is determined by the beam size as shown in Section 3.3.4 and is expected to be constant against frequency. The same situation occurs at the entrance of a receiver, e.g., a horn aperture, due to the same reasons. Therefore, the positions of the aperture stop and

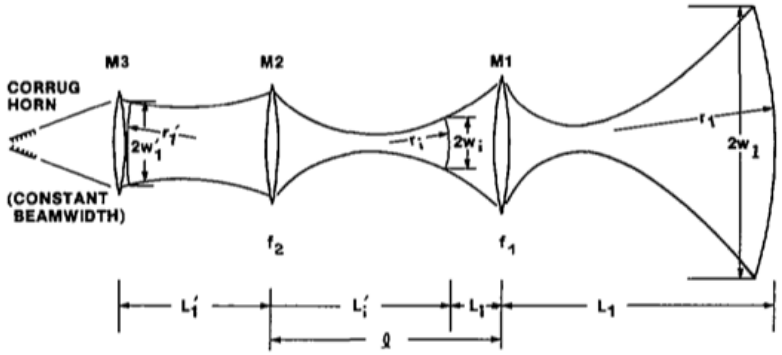

Figure 3.8: An example of application the condition (Fig. 2 in Chu 1983).

a receiver entrance should meet the lens formula and each element, a lens or a mirror, should be adapted such that the lens formula holds there.

The theory and the relations proved by Chu (1983) are based on the assumption that the beam taken into consideration is a fundamental Gaussian beam. This assumption is reasonable to apply the relation to a single-beam system. It is, however, not suitable when a wide field-of-view system is considered because beams in a wide field-of-view system is different from fundamental Gaussian beams. A fundamental Gaussian beam cannot describe complicated situations seen in a wide field-of-view system.

In Chapter 4, it is shown that the relations proved by Chu (1983) are one of general cases.

3.4.2 High Aperture Efficiency

It is revealed in Section 3.3.4 that an aperture efficiency is determined only by a beam size. An aperture efficiency is a slow function of a beam size, so that one can adopt a beam size such that other requirements are satisfied, e.g., the beam width, the side lobe level which appear in Section 3.3. However, in general, only a beam size can hardly determined an aperture efficiency because the beam propagating in a telescope is not a fundamental Gaussian beam. An actual beam propagating is affected by the edges of optical elements, misalignment, aberrations, and so on. As a result, beams are often distorted from a fundamental Gaussian beam.

In case of a beam different from a fundamental Gaussian beam, there are little discussions as to an aperture efficiency. Goldsmith (1998) considered a defocus case and also discussed tip-tilt and decenter with respect to coupling. Murphy (1987) dealt with distortion by off-axis mirrors, but did not reach comprehensive understanding. One of general methods is numerical simulation, e.g., PO simulation, which needs a lot of time and is unsuitable to make it clear what decreases an aperture efficiency. It is difficult to state that a method to design a telescope with a high aperture efficiency is established in terms of Optics, even in case of a single-beam telescope.

In Chapter 4, it is proposed to use quasioptics and PO simulation together with ray tracing simulation based on geometrical optics when a (wide field-of-view) telescope with a high aperture efficiency is designed. The relation between an aperture efficiency and aberrations is discussed, which leads to improve the method to design a radio telescope.

3.5 Summary

Some of the parameters derived in Chapter 2 are explicitly expressed for an aperture antenna. If a beam propagating in a telescope is assumed to be a fundamental Gaussian beam, the parameters can be determined by its beam size.

The requirements to design a radio telescope are a frequency-independent aperture efficiency and as a high aperture efficiency as possible. The condition to achieve a frequency-independent system by using a fundamental Gaussian beam has been known but is unsuitable to design a wide field-of-view telescope. The aperture efficiency expressed by a fundamental Gaussian beam is well known but an actual beam is different from a fundamental mode, which has not been investigated adequately. In the next chapter, a generalized condition to achieve a system independent of frequency and an aperture efficiency for actual beams including distorted beams are shown.

4

Radio Telescope Optics for Wide Field of View

4.1 Introduction

It is revealed in the previous chapter what efficiencies constitute an aperture efficiency. Especially, in assuming an on-axis fundamental Gaussian beam, only the beam size determines it. The frequency-independent condition has also been revealed by assuming an on-axis fundamental Gaussian beam. Removing the limitation of "an on-axis fundamental Gaussian beam" is one of the goals in this chapter and extends the relations for a single-beam telescope demonstrated in Chapter 3 into relations for more general cases. An aperture efficiency and a frequency-independent condition generalized to an arbitrary beam lead a novel method to design a wide field-of-view radio telescope is proposed.

In Section 4.2, the frequency-independent condition for a wide field-of-view telescope is discussed by referring to Imada et al. (2015b). In Section 4.3, an aperture efficiency is extended for more general cases based on Imada & Nagai (2016). In Section 4.4, a novel method to design an antenna is propsed.

4.2 Frequency-Independent Condition

The relations between an arbitrary electric field on an object plane and an induced one on an image plane after passing through a lens can be proved by calculating Fresnel diffraction integrals (Imada et al. 2015b). If the lens formula holds, there is a one-to-one correspondence between points on the object plane and the image plane. This result enables to use methods based on geometrical optics.

4.2.1 Wide Field-of-View System

There are a few properties of a wide field of view. In general, a wide field-of-view system has many mirrors to cancel aberrations, not only to transmit beams. Secondly, a free-form surface, e.g., Kataza et al. (2012), can be used recently, which enables to have more choice in designing an optical system. A free-form surface includes not only a conic surface but also a higher order polynomial surface. Transformation of a spherical wavefront into another spherical one by a conic surface is traditional and is a special case of general transformation, such as an aspherical wavefront into spherical one. Finally, beams in a wide field-of-view system propagate along various paths, i.e., most of beams are kept away from and tilted against the optical axis. It means that each beam passes through parts of lenses where the beam hits. It is necessary to focus on the influence of diffraction on an arbitrary field distribution, which depends on frequency.

Martin & Bowen (1993) calculated an electric field induced by an arbitrary electric field expanded into a summation of fundamental and higher order mode Hermite-Gaussian beams. Us-

ing beam-mode transfer matrices, Martin & Bowen (1993) derived the relations of Fourier Optics and showed that the distribution on an image plane can be calculated by scaling or magnifying the distribution on an object plane independently of frequency in case that the two planes met the lens formula. There, however, seems to be mathematically unclear points in deriving the relations; Martin & Bowen (1993) assumed the lens formula and discussed frequency-independent images with an analogy between a Fourier Optics system consisting of two transformers and a single lens system, though each system has different forms of beam-mode transfer matrices.

To calculate an arbitrary field, the Fresnel diffraction integral can be used instead of using beam-mode transfer matrices. Goodman (2005, Chapter 5) showed the calculation of the Fresnel diffraction integral but did not integrate on the object plane or take into consideration finally quadratic terms present in the phase terms.

It is shown to derive conditions, relations or equations to form images independent of frequencies applicable to a wide field-of-view system. These enable to make the frequency dependence of a telescope clear without applying the condition proved in Chu (1983) as many times as the number of optical elements. Clearer derivation is also demonstrated in a mathematical points of view.

4.2.2 Calculating Fresnel Diffraction Integral

Figure 4.1 represents the model for calculating the Fresnel diffraction integral. The coordinates are set as shown in Figure 4.1. An electromagnetic wave with a wavenumber of k propagates from the negative region of z to the positive. There is an axially symmetric lens at $z = 0$ with a radius of R and a focal length of $f > 0$. It is assumed for simplicity that the lens has no aberrations, though effects of aberrations appear in higher order terms of wavefront transformation than the quadratic terms taken here into consideration. The plane at $z = a$ is referred to as an object plane and the plane at $z = b$ as an image plane, respectively. The coordinates (ξ_1, η_1) and (ξ_2, η_2) are on the object plane and the image plane, respectively. $E_{\mathrm{obj}}(\xi_1, \eta_1)$, $E_{\mathrm{lens}}(x, y)$, and $E_{\mathrm{img}}(\xi_2, \eta_2)$ are electric fields expressed by a complex number on the object plane, the lens, and the image plane, respectively. The time dependence is assumed to be $\exp(\sqrt{-1}\omega t)$, where $\omega = ck$ and c is the speed of light.

The paraxial approximations of $1/k \ll x$, y, ξ, η, $R \ll a$, b, f are assumed. R is also assumed to be large enough to carry high spatial frequencies. Paying attention to the phase transformation at the lens, and using the Fresnel diffraction integral, the fields can be expressed as follows:

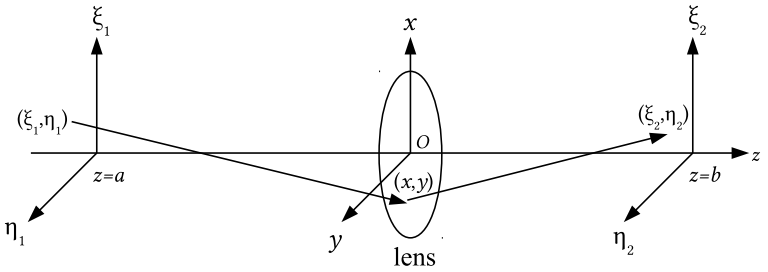

Figure 4.1: Model for calculating the Fresnel diffraction integral. There is a lens with a focal length of f at $z = 0$. The coordinates (ξ_1, η_1) and (ξ_2, η_2) are defined as shown. This figure is in case of $a < 0$ and $b > 0$, while our discussion goes in parallel no matter what their signs are.

$$E_{\rm lens}(x,y) = \frac{\sqrt{-1}\,k}{2\pi a}\exp\left(\sqrt{-1}\,ka + \sqrt{-1}\,k\,\frac{x^2+y^2}{2a}\right) \times \int \mathrm{d}\xi_1 \int \mathrm{d}\eta_1 E_{\rm obj}(\xi_1,\eta_1)\,\exp\left(-\sqrt{-1}\,k\,\frac{x\xi_1+y\eta_1}{a} + \sqrt{-1}\,k\,\frac{{\xi_1}^2+{\eta_1}^2}{2a}\right), \quad (4.1)$$

$$E_{\rm img}(\xi_2,\eta_2) = -\frac{\sqrt{-1}\,k}{2\pi b}\exp\left(-\sqrt{-1}\,kb - \sqrt{-1}\,k\,\frac{{\xi_2}^2+{\eta_2}^2}{2b}\right) \times \int \mathrm{d}x \int \mathrm{d}y\, E_{\rm lens}(x,y)\,\exp\left(\sqrt{-1}\,k\,\frac{x^2+y^2}{2f} + \sqrt{-1}\,k\,\frac{x\xi_2+y\eta_2}{b} - \sqrt{-1}\,k\,\frac{x^2+y^2}{2b}\right). \quad (4.2)$$

Substituting Equation (4.1) into Equation (4.2) and re-arranging the integrals, the fields on the object plane and the image plane are related.

$$E_{\rm img}(\xi_2,\eta_2) = \frac{k^2}{4\pi^2 ab}\exp\left(-\sqrt{-1}\,k(b-a) - \sqrt{-1}\,k\,\frac{{\xi_2}^2+{\eta_2}^2}{2b}\right) \times \int \mathrm{d}\xi_1 \int \mathrm{d}\eta_1\, E_{\rm obj}(\xi_1,\eta_1)\exp\left(\sqrt{-1}\,k\,\frac{{\xi_1}^2+{\eta_1}^2}{2a}\right) \times \int \mathrm{d}x \int \mathrm{d}y\,\exp\left[\sqrt{-1}\,k\,\frac{x^2+y^2}{2}\left(\frac{1}{f}+\frac{1}{a}-\frac{1}{b}\right)\right] \times \exp\left[-\sqrt{-1}\,kx\left(\frac{\xi_1}{a}-\frac{\xi_2}{b}\right) - \sqrt{-1}\,ky\left(\frac{\eta_1}{a}-\frac{\eta_2}{b}\right)\right]. \quad (4.3)$$

Equation (4.3) shows that the distribution $E_{\rm img}(\xi_2, \eta_2)$ on the image plane depends on the field distribution $E_{\rm obj}(\xi_1, \eta_1)$ on the object plane and the wavenumber k. Conditions to be derived are that the amplitude of $E_{\rm img}(\xi_2, \eta_2)$ except for phase becomes independent of the wavenumber k, that is,

$$E_{\rm img}(\xi_2,\eta_2) = C(a,b)E_{\rm obj}(\xi_1,\eta_1)\exp(\sqrt{-1}\,k\Delta), \quad (4.4)$$

where $C(a, b)$ is a real coefficient and Δ is an amount representing how a phase advances or retards. Equation (4.4) is a special case in terms of being independent of the wavenumber as a result of superposition of the diffracted wave.

To evaluate the integrals, the notation of variables and parameters is changed.

$$A := \frac{1}{f} + \frac{1}{a} - \frac{1}{b}, \quad \rho\cos\varphi := \frac{\xi_1}{a} - \frac{\xi_2}{b}, \quad \rho\sin\varphi := \frac{\eta_1}{a} - \frac{\eta_2}{b}, \quad r\cos\theta := x, \quad r\sin\theta := y. \tag{4.5}$$

The integral of x and y is defined as I, and integration over θ is carried out,

$$\begin{aligned} I &:= \int \mathrm{d}x \int \mathrm{d}y \, \exp\left[\sqrt{-1}\,kA\,\frac{x^2+y^2}{2} - \sqrt{-1}\,kx\left(\frac{\xi_1}{a} - \frac{\xi_2}{b}\right) - \sqrt{-1}\,ky\left(\frac{\eta_1}{a} - \frac{\eta_2}{b}\right)\right] \\ &= 2\pi \int_0^R \mathrm{d}r\, r \exp\left(\sqrt{-1}\,kA\,\frac{r^2}{2}\right) J_0(kr\rho), \end{aligned} \tag{4.6}$$

where J_0 is the zero order Bessel function of the first kind. Expanding J_0 yields

$$I = 2\pi \sum_{m=0}^{\infty} \frac{(-1)^m k^{2m} \rho^{2m}}{(m!)^2 2^{2m}} \int_0^R \mathrm{d}r\, r^{2m+1} \exp\left(\sqrt{-1}\,kA\,\frac{r^2}{2}\right). \tag{4.7}$$

The integral of r in Equation (4.7) contains higher order terms of k due to the exponential and becomes the coefficient of Equation (4.3) without integrated by ρ and φ. Then the following condition is required to obtain a relation in the form of Equation (4.4):

$$A = \frac{1}{f} + \frac{1}{a} - \frac{1}{b} = 0. \tag{4.8}$$

Equation (4.8) represents the well-known lens formula. Images independent of frequency can be obtained where and only where this formula holds. Note that one can expect ρ to be nearly zero because there are terms including the higher orders of k. Substituting Equation (4.8) into the integral I,

$$I = 2\pi R^2 \int_0^1 \mathrm{d}\left(\frac{r}{R}\right) \frac{r}{R}\, J_0\left(kr\,\frac{\rho}{R}\right) = \pi R^2\, \frac{2J_1(kR\rho)}{kR\rho}, \tag{4.9}$$

is obtained and the distribution is described as

$$\begin{aligned} E_{\mathrm{img}}(\xi_2, \eta_2) = \frac{R^2 k^2 a}{4\pi b} &\exp\left(-\sqrt{-1}\,k(b-a) - \sqrt{-1}\,k\,\frac{{\xi_2}^2 + {\eta_2}^2}{2b}\right) \\ &\times \int \mathrm{d}\rho \int \mathrm{d}\varphi\, \rho\, \frac{2J_1(kR\rho)}{kR\rho}\, E_{\mathrm{obj}}\left(a\rho\cos\varphi + \frac{a\xi_2}{b}, a\rho\sin\varphi + \frac{a\eta_2}{b}\right) \\ &\times \exp\left(\sqrt{-1}\,k\,\frac{\left(a\rho\cos\varphi + a\xi_2/b\right)^2 + \left(a\rho\sin\varphi + a\eta_2/b\right)^2}{2a}\right). \end{aligned} \tag{4.10}$$

Equation (4.10) allows one to adopt an arbitrary field distribution as the distribution E_{obj} as far as it exists physically, i.e., it is a constant or decreases to zero at infinity, because $2J_1(x)/x$ decreases rapidly as $x \gg 1$ where it behaves like $2\sqrt{2/\pi x^3}\cos(x - 3\pi/4)$ asymptotically. In addition, the

field $E_{\mathrm{img}}(\xi_2, \eta_2)$ is determined by only the field at a point $(a\xi_2/b, a\eta_2/b)$ because the paraxial approximation makes kR greater than unity. In other words, the distribution E_{obj} can contribute only when ρ is almost zero. By using Equation (4.8),

$$\begin{aligned} E_{\mathrm{img}}(\xi_2, \eta_2) = \frac{R^2 k^2 a}{4\pi b} \exp\left(-\sqrt{-1}\, k(b-a) + \sqrt{-1}\, k\, \frac{a}{b} \frac{{\xi_2}^2 + {\eta_2}^2}{2f}\right) \\ \times \int \mathrm{d}\rho \int \mathrm{d}\varphi\, \rho\, \frac{2J_1(kR\rho)}{kR\rho}\, E_{\mathrm{obj}}\left(a\rho\cos\varphi + \frac{a\xi_2}{b}, a\rho\sin\varphi + \frac{a\eta_2}{b}\right) \\ \times \exp\left[\sqrt{-1}\, \frac{ka\rho}{2}\left(\rho + \frac{2(\xi_2\cos\varphi + \eta_2\sin\varphi)}{b}\right)\right]. \end{aligned} \tag{4.11}$$

Consider the integral of the Bessel function included in Equation (4.11),

$$\int_0^\infty \mathrm{d}\rho \int_0^{2\pi} \mathrm{d}\varphi\, \rho\, \frac{2J_1(kR\rho)}{kR\rho} = \frac{4\pi}{k^2R^2} \int_0^\infty \mathrm{d}(kR\rho)\, J_1(kR\rho) = \frac{4\pi}{k^2R^2}. \tag{4.12}$$

By using a simple relation,

$$\int_0^{2/(kR)} \mathrm{d}\rho \int_0^{2\pi} \mathrm{d}\varphi\, \rho = \frac{4\pi}{k^2R^2}, \tag{4.13}$$

the integral limit of ρ is replaced by $2/(kR)$, and moreover, $2J_1(kR\rho)/kR\rho$ and the exponential term in the integral by unity because the distribution E_{obj} contributes to the integral only when ρ is almost zero as mentioned above. Finally, the distribution E_{obj} and phase term can be regarded as a constant $E_{\mathrm{obj}}(a\xi_2/b, a\eta_2/b)$ because the variations of them are slow in the ρ range of $[0, 2/(kR)]$ which corresponds to the size of a few wavelengths on the object plane. Thus the relation is acquired,

$$\begin{aligned} E_{\mathrm{img}}(\xi_2, \eta_2) &\approx \frac{a}{4\pi b} \exp\left(-\sqrt{-1}\, k(b-a) + \sqrt{-1}\, k \frac{a}{b} \frac{{\xi_2}^2 + {\eta_2}^2}{2f}\right) \\ &\quad \times \int_0^{2/(kR)} \mathrm{d}\rho \int_0^{2\pi} \mathrm{d}\varphi\, \rho\, E_{\mathrm{obj}}\left(\frac{a\xi_2}{b}, \frac{a\eta_2}{b}\right) \\ &= \frac{a}{b}\, E_{\mathrm{obj}}\left(\frac{a\xi_2}{b}, \frac{a\eta_2}{b}\right) \exp\left(-\sqrt{-1}\, k(b-a) + \sqrt{-1}\, k\, \frac{a}{b} \frac{{\xi_2}^2 + {\eta_2}^2}{2f}\right). \end{aligned} \tag{4.14}$$

The derived condition and relations are gathered,

$$\frac{1}{f} = -\frac{1}{a} + \frac{1}{b}, \tag{4.15}$$

$$E_{\mathrm{img}}(\xi_2, \eta_2) = \frac{a}{b}\, E_{\mathrm{obj}}\left(\frac{a\xi_2}{b}, \frac{a\eta_2}{b}\right) \exp\left(-\sqrt{-1}\, k(b-a) + \sqrt{-1}\, k\, \frac{a}{b} \frac{{\xi_2}^2 + {\eta_2}^2}{2f}\right), \tag{4.16}$$

$$\frac{\xi_1}{a} = \frac{\xi_2}{b},\ \frac{\eta_1}{a} = \frac{\eta_2}{b}. \tag{4.17}$$

Since these apply for any signs of a, b, and f, Equations (4.16) and (4.17) hold whenever a and

b meet the lens formula Equation (4.15). Equations (4.15) to (4.17) can be derived clearly and concisely, which can be seen in Martin & Bowen (1993).

4.2.3 Relation to Geometrical Optics

An intent look at Equations (4.16) and (4.17) shows that there is a one-to-one correspondence between the points (ξ_1, η_1) on the object plane and (ξ_2, η_2) on the image plane such that $(\xi_1, \eta_1) = (a\xi_2/b, a\eta_2/b)$. It means that one can treat the field distribution with geometrical optics on the planes where the lens formula holds. Whenever an imaging system having an object and its image with no aberrations is formed by geometrical optics, Equation (4.16) can be applied to it. In addition, geometrical optics allows one to know an equivalent single lens system obtained by ray tracing simulation or by the formula combining two focal lengths of f_1 and f_2,

$$\frac{1}{f_{\mathrm{comb}}} = \frac{1}{f_1} + \frac{1}{f_2} - \frac{d}{f_1 f_2}, \tag{4.18}$$

where f_{comb} is an equivalent focal length and d is the distance between two lens. It is important to consider an equivalent single lens system because there are difficulties in applying the relations as many times as the number of optical elements in a system considered, and because the relations cannot be applied to one of a pair of elements which works as one lens. By using ray tracing simulation, an equivalent focal length is obtained, and then, the condition and relations derived here can be applied to a complicated system with many focusing elements, or with each element not having a traditional focal length, e.g., a mirror with a free-form surface. Thus, Equation (4.16) can be applied to an arbitrary optical system because an equivalent single lens system of it is obtained by geometrical optics.

Next, consider how to apply Equation (4.16) to a wide field-of-view system. In general, various beams propagate on corresponding paths to each beam in a wide field-of-view system but coincide at "pupils", where all of them are piled up on the same position. The pupil is a fundamental concept in geometrical optics (Born & Wolf 1997). The lens formula always holds on all of the pupils because they are images of one another. In addition, it is most important that beam patterns are defined at either the entrance pupil or the exit pupil; for the entrance pupil, beam patterns are far-field patterns, for the exit pupil they are "receiver" patterns, i.e. point-spread functions. When electric field amplitude at a specific pupil is given and Equation (4.16) is applied to it and the entrance (exit) pupil, the electric field amplitudes of all the beams are the same unrelated to propagating direction and always independent of frequency on the pupils. Thus, a frequency-independent system is simply obtained. All things to construct a frequency-independent system are to investigate positions of pupils with ray tracing simulation or Equation (4.18) and to determine beam parameters on one of the pupils.

4.2.4 Verification of Relation

Relation Derived by Chu (1983)

In this section, the relation (4.16) is verified through some examples. Firstly, Equation (4.16) is applied to a fundamental Gaussian beam, which leads to the condition derived by Chu (1983). Assuming a fundamental Gaussian beam with a beam waist of w_0 which is located at $z = a_0$,

$$E_{\mathrm{obj}}(x_1, y_1; a) = \sqrt{\frac{2}{\pi w(a)^2}} \exp\left[-\frac{{x_1}^2 + {y_1}^2}{w(a)^2} - \sqrt{-1}\, k(a - a_0) + \sqrt{-1}\, k\, \frac{{x_1}^2 + {y_1}^2}{2R(a)} + \sqrt{-1}\, k\varphi(a)\right], \tag{4.19}$$

$$w(a) = w_0 \sqrt{1 + \left(\frac{2(a - a_0)}{k{w_0}^2}\right)^2}, \tag{4.20}$$

$$R(a) = -(a - a_0)\left[1 + \left(\frac{k{w_0}^2}{2(a - a_0)}\right)^2\right], \tag{4.21}$$

$$\varphi(a) = -\tan^{-1}\frac{2(a - a_0)}{k{w_0}^2}, \tag{4.22}$$

Substituting these equations into Equation (4.16) results in

$$\begin{aligned} E_{\mathrm{img}}(x_2, y_2; b) &= \frac{a}{b} E_{\mathrm{obj}}\left(\frac{ax_2}{b}, \frac{ay_2}{b}; a\right) \exp\left(-\sqrt{-1}\, k(b - a) + \sqrt{-1}\, k\, \frac{a}{b} \frac{{x_2}^2 + {y_2}^2}{2f}\right) \\ &= \mathrm{sgn}\left(\frac{a}{b}\right) \sqrt{\frac{2a^2}{\pi b^2 w(a)^2}} \exp\left[-\frac{{x_2}^2 + {y_2}^2}{b^2 w(a)^2/a^2} - \sqrt{-1}\, k(b - b_0)\right] \\ &\quad \times \exp\left[\sqrt{-1}\, k\, \frac{{x_2}^2 + {y_2}^2}{2}\left(\frac{a^2}{b^2 R(a)} + \frac{a}{bf}\right) + \sqrt{-1}\, k(\varphi(a) + a_0 - b_0)\right], \end{aligned} \tag{4.23}$$

where $b = (1/f + 1/a)^{-1}$, b_0 is the position of a beam waist after a focusing element. By compared to the general form of a fundamental Gaussian beam, the following relations are obtained from Equation (4.23),

$$w'(b)^2 = \frac{b^2 w(a)^2}{a^2}, \tag{4.24}$$

$$\frac{1}{R'(b)} = \frac{a^2}{b^2 R(a)} + \frac{a}{bf}, \tag{4.25}$$

$$\varphi'(b) = \varphi(a) + a_0 - b_0. \tag{4.26}$$

By arranging them, the relations shown in Chu (1983) are acquired.

$$\frac{w'(b)^2}{b^2} = \frac{w(a)^2}{a^2}, \tag{4.27}$$

$$b\left(1 + \frac{b}{R'(b)}\right) = a\left(1 + \frac{a}{R(a)}\right). \tag{4.28}$$

Application to One-mirror System

Next, consider a one-spherical-mirror system with a focal length $f = 150$ mm. PO simulation using GRASP 8 (TICRA Engineering Consultants 2003) is conducted and simulation results are compared to the distributions expected by Equation (4.8). Three Gaussian beams enter the mirror; a 500 GHz on-axis beam, a 500 GHz beam 10 mm off the axis (Figure 4.2), and a 1 THz beam with the same beam radius and radius of curvature of a wavefront at the plane obj2 as those of the 500 GHz off-axis beam. The beam waists of the 500 GHz beams are located at 450 mm. First, the field distributions of the incident beams on the planes obj1, obj2, and obj3 at $z = 200$, 300, and 600 mm, respectively, are calculated. The beams reflect and then the distribution of the reflected beams on the planes img1, img2, and img3 at $z = 600$, 300, and 200 mm, respectively, are calculated by two ways, the PO simulation and substituting the distribution on the planes obj1, obj2, and obj3, into Equation (4.8). Finally the distributions obtained by the PO simulation and Equation (4.8) are compared.

Figure 4.3 and Figure 4.4 show the results of the 500 GHz beams. In Figure 4.3, the electric field distributions expected by Equation (4.16) agree with those calculated by the PO simulation very well. The finite size of the spherical mirror affects the distribution distant from the center as shown in Figure 4.3 (b), (c), (e), and (f). The distribution at img1 (Figure 4.3 (a) and (d)) should also be affected in a region $|x| > 50$ mm, where PO simulation has not been conducted. The effect of mirror aberrations which fills in nulls between side lobes is also seen. The results of calculating the phase by the PO simulation and Equation (4.16) are shown in Figure 4.4. The results of Equation (4.16) also agree with those by PO simulation near the center where the effect of mirror size is weak. It is confirmed that Equation (4.16) holds at the position satisfying the lens formula with the 500 GHz beams.

It is finally confirmed whether the field distributions and phase on the specific positions are independent of the beam frequencies. The 500 GHz and the 1 THz off-axis beams are used. The results are shown in Figure 4.5. Except for the region where the effect of the finite mirror size exists, the distribution and the wavefront of both frequencies shows the same shape at img2. This confirms that the condition for fields independent of frequency is that the plane positions which are taken into consideration satisfy the lens formula, $1/f = -1/a + 1/b$, and that the distribution and phase have the relations expressed by Equation (4.16).

Application to Three-mirror Telescope

Equation (4.16) is applied to a three-mirror telescope in Figure 4.6 (a). The primary mirror is an off-axis paraboloid with a diameter of 300 mm. The secondary mirror is an off-axis ellipsoid. The tertiary mirror is an off-axis hyperboloid. The parameters of the three mirrors are determined

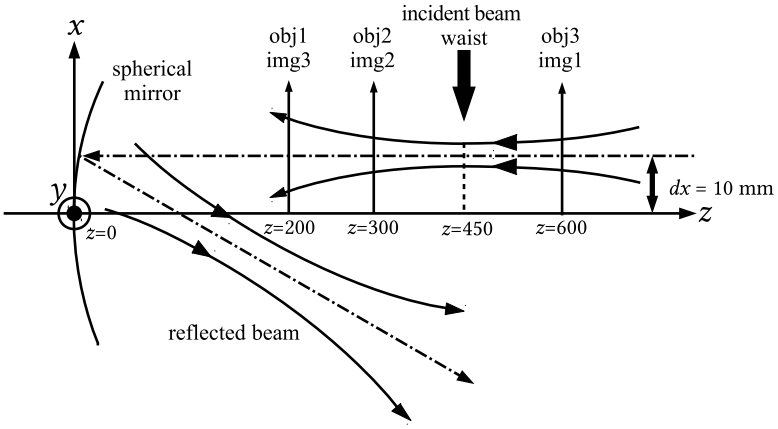

Figure 4.2: One-mirror simulation model for the 500 GHz off-axis beam. The incident beam propagates 10 mm off the axis and in parallel to it, and a reflected beam does not in parallel to it as shown. Both beams are in the region $z > 0$. The planes (obj1, img1), (obj2, img2), and (obj3, img3) are pairs of images that satisfy the lens formula.

following Chang & Prata (2005). The ray tracing software (Radiant Zemax 2014) is used. The telescope has a focal length of about 1663 mm and has a wide field of view of 1 degree at 1 THz without vignetting in which there are scarecely aberrations. The secondary mirror works as a stop; its images shown in Figure 4.6 (b) are the entrance and exit pupils, on which the lens formula holds. The relation (4.16) can be applied. In this case, an equivalent a and b are about -4236 mm and 2731 mm, respectively, at which the pupils are located.

PO simulation is carried out. Four beams pass through the telescope from the focal plane. One of them is a 500 GHz on-axis beam, the second is a 500 GHz 0.5 degrees off-axis apart from the center of field of view, the others are the same beams as the 500 GHz ones, except for the frequency of 1 THz. The off-axis beams propagate toward the center of the exit pupil (Figure 4.6 (b)). An edge taper is set to be -15 dB at the secondary. Combining this edge taper with the radius of the aperture stop at the secondary gives a beam radius w_0 to be used in Equation (4.16). The radius of curvature of wavefront is estimated from a distance between the focal plane and the exit pupil. With these parameters, if the field distribution at the exit pupil is independent of frequency, it is expected that the distribution on the entrance pupil will be also independent of frequency.

Figure 4.7 shows the distributions at the exit and the entrance pupil of the telescope. The 500 GHz and the 1 THz distributions are similar on the exit pupil and keep their own shape on the entrance pupil. The fine dotted lines in Figure 4.7 represent the expected distributions by Equation (4.16). It is shown that the field distributions on the entrance pupil do not depend on the beam frequencies and specific information of the telescope, e.g. the number of mirrors, focal lengths of each, and so on. Although Equation (4.16) frees one from having to know details of the

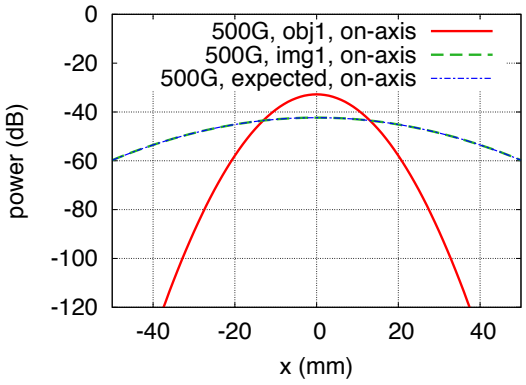

(a) 500 GHz on-axis beam on obj1 and img1.

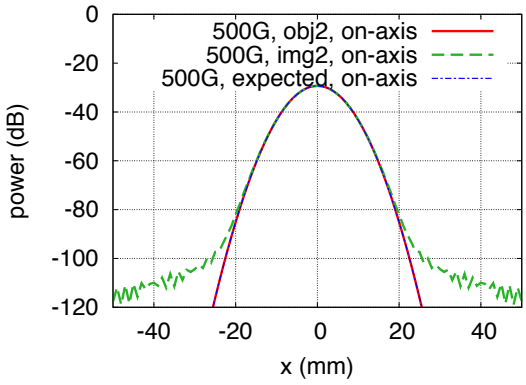

(b) 500 GHz on-axis beam on obj2 and img2.

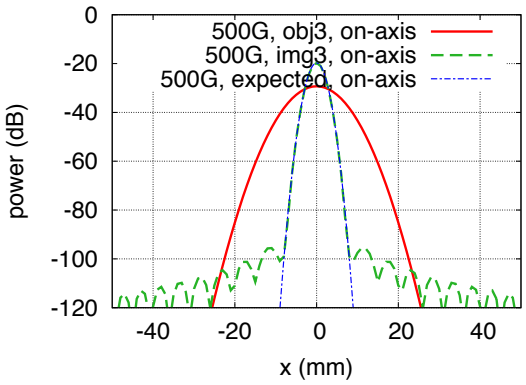

(c) 500 GHz on-axis beam on obj3 and img3.

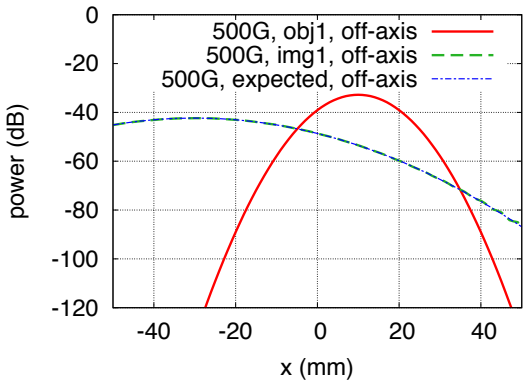

(d) 500 GHz off-axis beam on obj1 and img1.

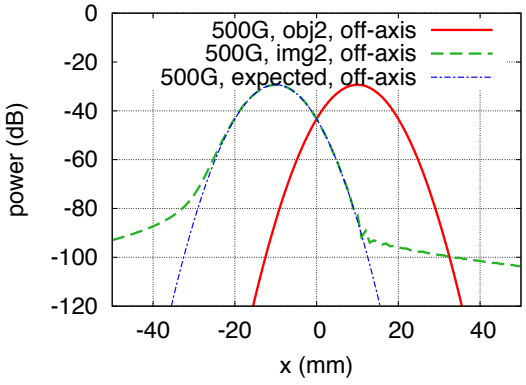

(e) 500 GHz off-axis beam on obj2 and img2.

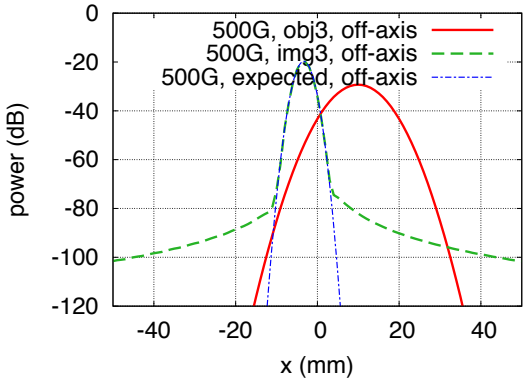

(f) 500 GHz off-axis beam on obj3 and img3.

Figure 4.3: Calculated electric fields on the planes, obj and img. The red (solid) line is the incident beam, the green (dashed) line the reflected beam calculated by PO simulation. The blue (dashed-dotted) line is a expected distribution by Equation (8) from the incident beam distribution (the red-solid line).

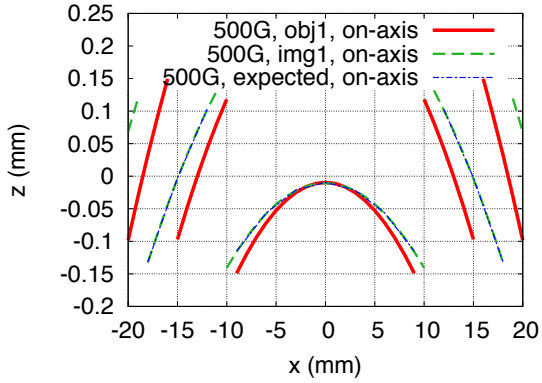

(a) 500 GHz on-axis beam on obj1 and img1.

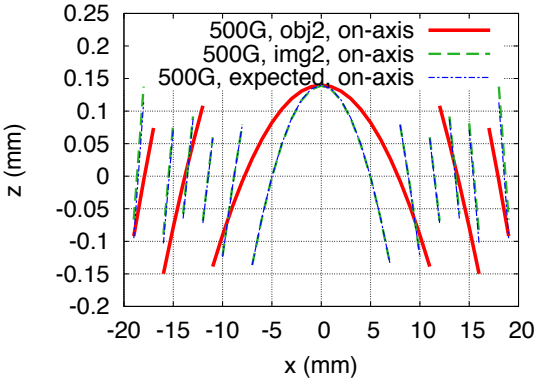

(b) 500 GHz on-axis beam on obj2 and img2.

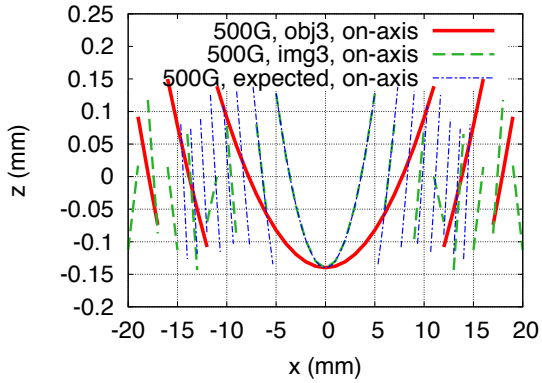

(c) 500 GHz on-axis beam on obj3 and img3.

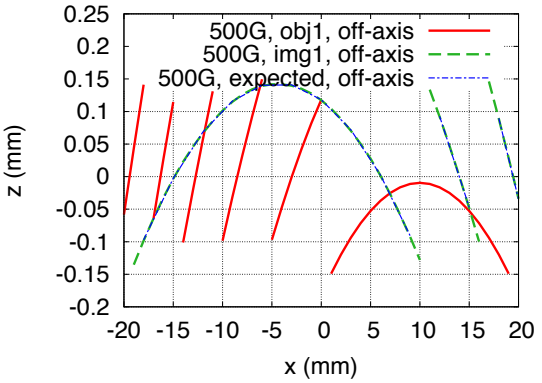

(d) 500 GHz off-axis beam on obj1 and img1.

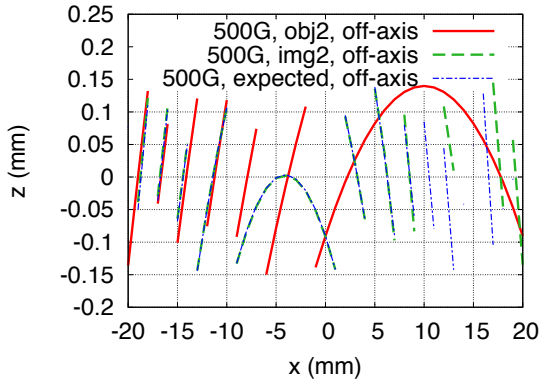

(e) 500 GHz off-axis beam on obj2 and img2.

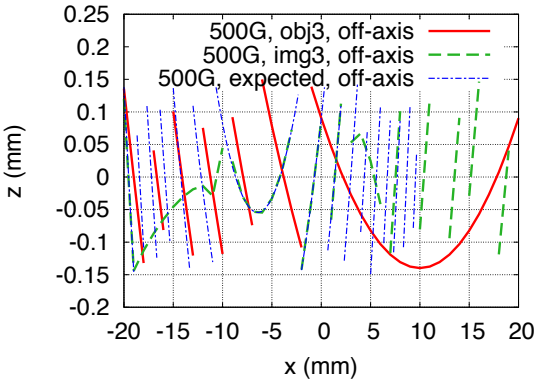

(f) 500 GHz off-axis beam on obj3 and img3.

Figure 4.4: Cross sections of wavefront on the plane $y = 0$ at the planes obj and img. Figures (a) to (f) correspond to Figure 4.3 (a) to (f), respectively. The red (solid) line is the incident beam, the green (dashed) line the reflected beam calculated by PO simulation. The blue (dashed-dotted) line is expected by Equation (4.16) from the incident beam distribution (the red-solid line).

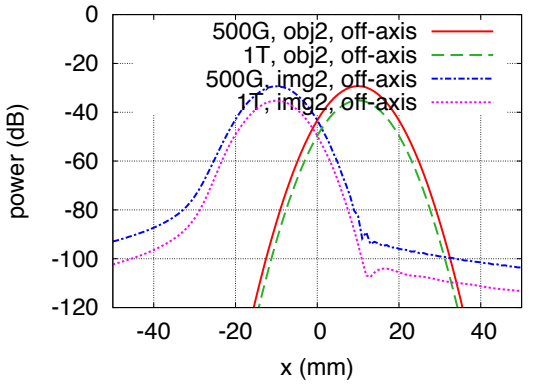

(a)

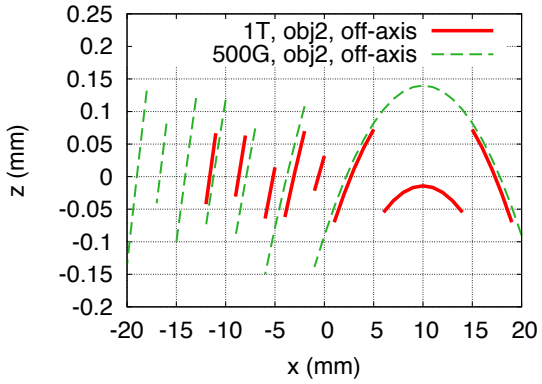

(b)

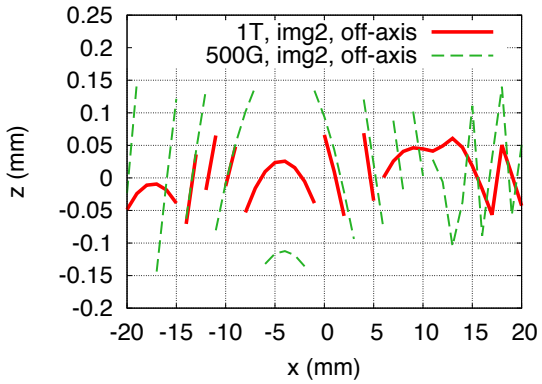

(c)

Figure 4.5: The distribution and the wavefront on obj2 and img2. (a) The red (solid) line and green (dashed) line represent the distributions of the 500 GHz and the 1 THz off-axis incident beam, respectively. They are similar one. The blue (dashed-dotted) line and magenta (dotted) line is the 500 GHz and the 1 THz off-axis reflected beam distribution, respectively. (b) The red (solid) line and green (dashed) line represent the cross sections of the wavefront of the 500 GHz and the 1 THz off-axis incident beams, respectively. (c) The red (solid) line and green (dashed) line represent the cross sections of the wavefront of the 500 GHz and the 1 THz off-axis reflected beam, respectively. They have the same shape.

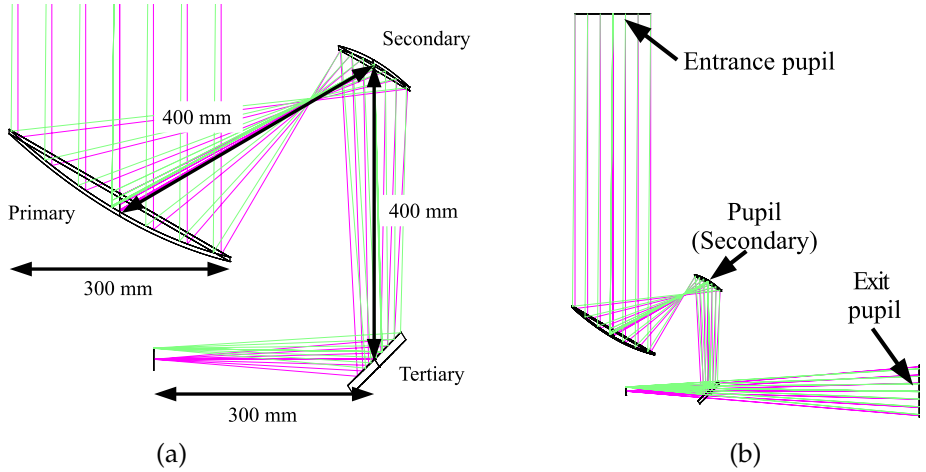

Figure 4.6: Three mirror telescope considered. (a) The primary and secondary mirror fold beams by 60 degrees, and the tertiary folds by 90 degrees. (b) There are three pupils in the considered telescope. One of them is located at the secondary. The Entrance pupil is an image of the secondary by the primary, and the exit pupil is by the tertiary. The magenta beam is on the axis of the telescope. The green beam is 0.5 degrees off the center of the field of view.

system, it does not tell whether the actual sizes of mirrors are sufficient to transmit beams without significant distortion; these sizes must be determined by other methods, e.g., PO simulation. It is also unknown whether efficiencies of a whole system are high or not.

The beam patterns of this telescope are also calculated. Figure 4.8 shows the beam patterns of the four beams on the celestial sphere. They are axially symmetric and have the beam widths expected from the diameter of the entrance pupil.

4.2.5 Summary of Frequency-Independent Condition

Starting from the Fresnel diffraction integral, the condition for a wide field-of-view system to form images independent of frequency is derived. The condition can be expressed simply using the well-known lens formula. One can obtain images independent of frequency where and only where the lens formula holds. The relation of the field distributions between the object and image planes is also acquired. The relation corresponds completely to geometrical optics. The relation of the phase is directly derived. Numerical simulation verifies the derived relations with a simple model consisting of one mirror. In addition, it is confirmed that they can be applied to a wide field-of-view telescope with the model of a three-mirror telescope. To design a wide field-of-view telescope, calculating an equivalent focal length to the optical system considered and the position of the entrance and exit pupil with geometrical optics or ray tracing software is everything to do, and then next thing is to determine beam parameters at the pupils.

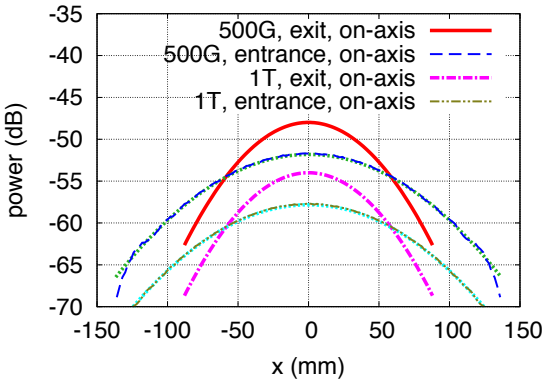

(a) On-axis beams, field along x axis.

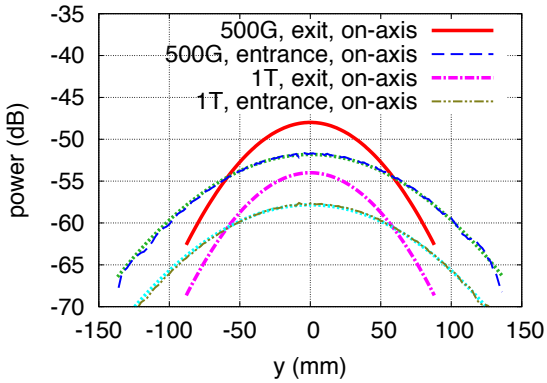

(b) On-axis beams, field along y axis.

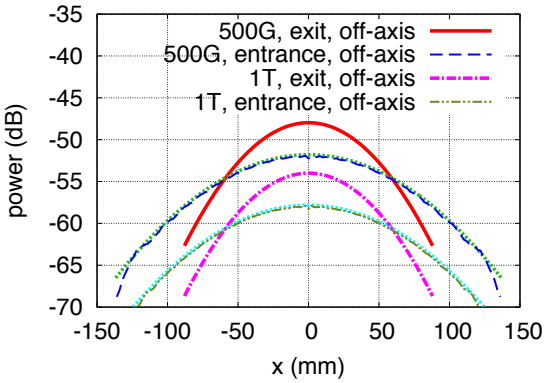

(c) Off-axis beams, field along x axis.

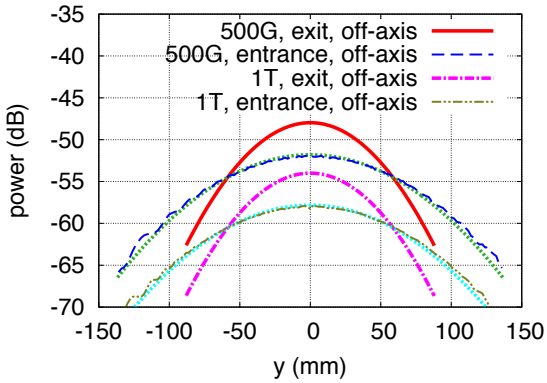

(d) Off-axis beams, field along y axis.

Figure 4.7: Three-mirror telescope: field distributions on the entrance and exit pupil. The red (solid) line is the distribution of the 500 GHz beam at the exit pupil, the blue (dashed) line is that at the entrance pupil. The magenta (dashed-dotted) and greenish brown (dashed-dotted-dotted) represents the distribution of the 1 THz beam at the entrance and exit pupil, respectively. The cyan and green (fine dotted) lines are expected from the distribution on the exit pupil.

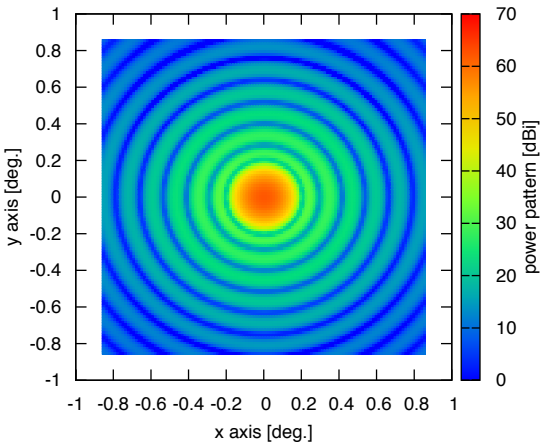

(a) 500 GHz on-axis beam.

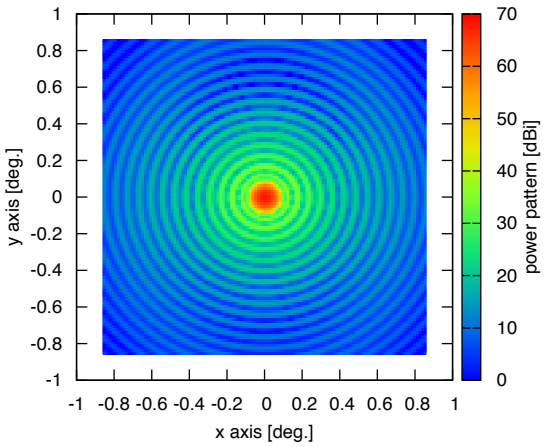

(b) 1 THz on-axis beam.

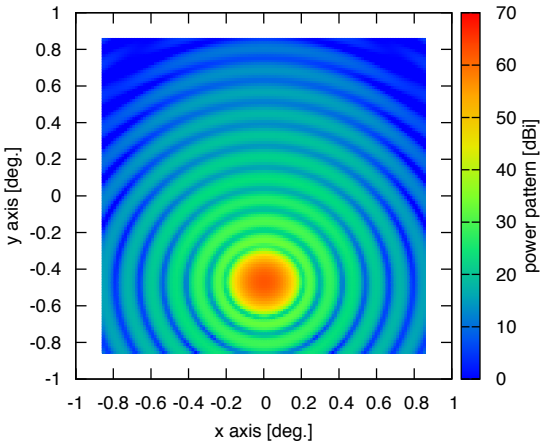

(c) 500 GHz off-axis beam.

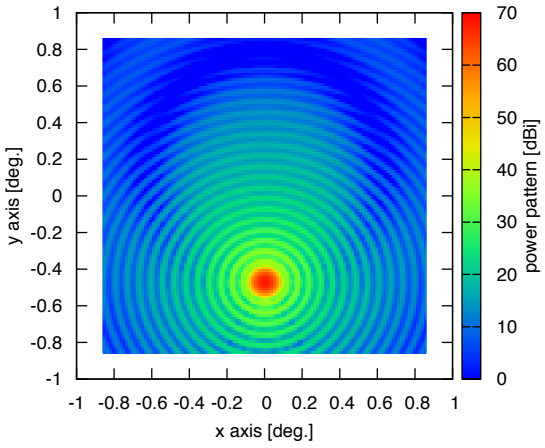

(d) 1 THz off-axis beam.

Figure 4.8: Beam patterns of the telescope.

4.3 Aperture Efficiency for Arbitrary Beam

To consider how a wide field-of-view telescope behaves, the aperture efficiency introduced in the preceding chapter is extended into more general cases, such as for a distorted beam and optics with aberrations. By making a guess from the aperture efficiency, Equation (3.14), which consists of spillover efficiencies and a beam pattern, wavefront errors of an incident wave and a distribution of detector sensitivity at an aperture are expected to play an important role in determining antenna performance.

In terms of wavefront errors, Gaussian beams affected by wavefront errors have been discussed (e.g., Arimoto 1974; Lowenthal 1974). Balanced aberrations for Gaussian beams have also been reported (Mahajan 1982, 1986). They are, however, inadequate to discuss the aperture efficiency because the wave entering a radio telescope is a plane wave, not a Gaussian beam. The response of coupling between a Gaussian beam and a plane wave has to be discussed. Olmi & Bolli (2007) examined the relation between a Strehl ratio and an aperture efficiency. They pointed out that an aperture efficiency is a function of wavefront errors, but they did not completely clarify the parameter dependence. To design a wide field-of-view system, it is important to consider the parameter dependence of an aperture efficiency.

There are a few ways to calculate an aperture efficiency. In this section, by expanding the wavefront errors of an incident wave and the distribution of detector sensitivity into the summation of the Zernike polynomials, it is proved that an aperture efficiency, especially an coupling efficiency, can be expressed in any case. Discussion in this section is conducted based on Imada & Nagai (2016).

4.3.1 Definitions and assumptions

System Setting and Symbols

It is assumed that an optical system with an annular aperture is axially symmetric and an electromagnetic wave propagating through the system has the time dependence $\exp(\sqrt{-1}\omega t)$. $\omega = ck$ where c is the speed of light and $k = 2\pi/\lambda$ is the wave number. The radius of curvature of the wavefront is positive when the wavefront is convex as seen from the negative part of the coordinate system. Linear polarization is also assumed, the direction of which corresponds to that of the detector sensitivity.

Pupil, Aperture, and Aperture Plane

Pupil is a fundamental concept in geometrical optics and is defined as the image of an aperture stop (Born & Wolf 1997, pp. 186–188). There are no optical elements between an object and an

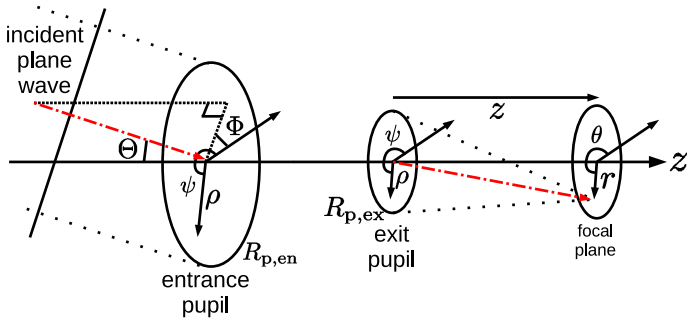

Figure 4.9: Definition of the coordinates.

entrance pupil, and between an exit pupil and an image. Fresnel diffraction describes the propagation between the object and the entrance pupil and between the exit pupil and the image.

The positions of an aperture and an aperture plane are hardly specified so far because an electromagnetic wave after leaving the aperture can be regarded as a plane wave (Goldsmith 1998, Chap. 6). In order to discuss the incident direction dependence in Section 4.3.2, the opening of the first element in an optical system is regarded as an aperture, an infinite plane expanding the aperture as an aperture plane. An entrance pupil is not necessarily located at an aperture.

Coordinates

Figure 4.9 shows the coordinates used in this section. (Θ, Φ) represent the direction of an incident plane wave. (r, θ, z) are cylindrical coordinates and $z = 0$ corresponds to the exit pupil. Another set of coordinates (ρ, ψ) on the exit pupil are introduced. ρ $(\varepsilon \leq \rho \leq 1,\ 0 \leq \varepsilon < 1)$ is a dimensionless amount normalized by $R_{\mathrm{p,en}}$ or $R_{\mathrm{p,ex}}$ which represent the radii of the entrance pupil and exit pupil, respectively. ε is a dimensionless parameter of the center hole radius of the annular aperture. ρ and ψ are common parameters of the pupils. f is the focal length of the considered optical system. Incident angle (Θ, Φ) can relate to the Gaussian image point $(r_{\mathrm{g}}, \theta_{\mathrm{g}}, z_{\mathrm{g}})$ with $r_{\mathrm{g}} = f \tan\Theta$ and $\theta_{\mathrm{g}} = \Phi + \pi$ if there are no aberrations.

For simplicity, unit vector $\hat{\boldsymbol{p}}$ which is set to direction (Θ, Φ) from the entrance pupil center, vector $\boldsymbol{\rho}$ which is set to point (ρ, ψ) on the pupils, and vector $\boldsymbol{r}$ which is set to point (r, θ, z) from the exit pupil center are introduced.

Wavefront Error

Focus on the wavefront of an incident wave propagating toward the exit pupil. In the ideal case, the incident wave at the exit pupil is a spherical wave whose radius is equal to the distance between the exit pupil center and the Gaussian image point, but the actual wavefront is not spherical because of aberrations. Wavefront error W is defined as seen in Figure 4.10. Wavefront W is posi-

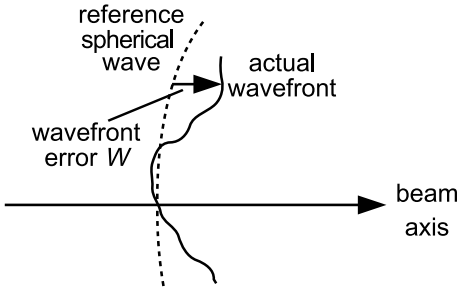

Figure 4.10: Definition of the wavefront error. The beam propagates from the left to the right. The beam axis corresponds to the red (dashed-dotted) arrow in Figure 4.9.

tive when the actual wavefront deviates to the direction of beam propagation. In this paper, it is is assumed that the wavefront is deformed by Seidel aberrations, and therefore, random wavefront errors caused by, e.g., atmospheric fluctuation and optical element surface roughness, are not discussed. For considering these errors, statistical methods are needed, as seen in Ruze (1966); Fried (1965); Noll (1976), which are beyond the scope of this paper. Wavefront error W depends on an incident angle $\hat{\boldsymbol{p}}$, position on the pupil $\boldsymbol{\rho}$, and reference spherical wave center $\boldsymbol{r}_{\mathrm{ref}}$, which means

$$W = W(\hat{\boldsymbol{p}}; \boldsymbol{\rho}; \boldsymbol{r}_{\mathrm{ref}}). \tag{4.29}$$

Field at Pupils

The field distribution of an incident wave at the entrance pupil is assumed to be uniform, i.e.,

$$E_{\mathrm{inc}}(\hat{\boldsymbol{p}}; \boldsymbol{\rho}) = \begin{cases} \exp\left[\sqrt{-1}kR_{\mathrm{p,en}}\rho\sin\Theta\cos(\psi-\Phi)\right] & (\varepsilon \le \rho \le 1) \\ 0 & (\mathrm{otherwise}) \end{cases}. \tag{4.30}$$

If there are no aberrations, the field distribution at the exit pupil corresponds to that at the entrance pupil (Imada et al. 2015b) and becomes a spherical wave centered at Gaussian image point $\boldsymbol{r}_{\mathrm{g}} = (r_{\mathrm{g}}, \theta_{\mathrm{g}}, z_{\mathrm{g}})$, that is,

$$\begin{aligned} E_{\mathrm{ex}}(\hat{\boldsymbol{p}}; \boldsymbol{\rho}) &= \frac{R_{\mathrm{p,en}}}{R_{\mathrm{p,ex}}} E_{\mathrm{inc}}\left(\hat{\boldsymbol{p}}; \frac{R_{\mathrm{p,ex}}}{R_{\mathrm{p,en}}}\boldsymbol{\rho}\right) \\ &= \begin{cases} \dfrac{R_{\mathrm{p,en}}}{R_{\mathrm{p,ex}}} \exp\left[\sqrt{-1}k\dfrac{f}{z_{\mathrm{g}}}R_{\mathrm{p,ex}}\rho\sin\Theta\cos(\psi-\Phi) + \sqrt{-1}\dfrac{k{R_{\mathrm{p,ex}}}^2}{2z_{\mathrm{g}}}\rho^2\right] & (\varepsilon \le \rho \le 1) \\ 0 & (\mathrm{otherwise}) \end{cases}. \end{aligned} \tag{4.31}$$

To derive Equation (4.31), the geometrical relation $R_{\mathrm{p,en}}/f = R_{\mathrm{p,ex}}/z_{\mathrm{g}}$ is used.

The reference spherical wave center $\boldsymbol{r}_{\mathrm{ref}}$ can be set to a different point from Gaussian image

point $\boldsymbol{r}_{\mathrm{g}}$. If $W(\hat{\boldsymbol{p}};\boldsymbol{\rho};\boldsymbol{r}_{\mathrm{ref}}) \ll \lambda$, it can be assumed that wavefront error $W(\hat{\boldsymbol{p}};\boldsymbol{\rho};\boldsymbol{r}_{\mathrm{ref}})$ affects only the wavefront form and does not affect the amplitude distribution $|E_{\mathrm{ex}}(\hat{\boldsymbol{p}};\boldsymbol{\rho})|$. Thus,

$$E_{\mathrm{ex}}(\hat{\boldsymbol{p}};\boldsymbol{\rho}) = \frac{R_{\mathrm{p,en}}}{R_{\mathrm{p,ex}}} E_{\mathrm{inc}}\left(\hat{\boldsymbol{p}}; \frac{R_{\mathrm{p,ex}}}{R_{\mathrm{p,en}}}\boldsymbol{\rho}\right) \exp\left[\sqrt{-1}kW(\hat{\boldsymbol{p}};\boldsymbol{\rho};\boldsymbol{r}_{\mathrm{ref}})\right] \tag{4.32}$$

4.3.2 Analytical Expression of Aperture Efficiency

The definition of an aperture efficiency is summarized based on Nagai & Imada (2016). An aperture efficiency η_{A} is defined as the product of two spillover efficiencies, $\eta_{\mathrm{sp,en}}$, $\eta_{\mathrm{sp,ex}}$, and a coupling efficiency η_{coup},

$$\eta_{\mathrm{A}}(\hat{\boldsymbol{p}};\boldsymbol{r}_{\mathrm{ref}}) := \eta_{\mathrm{sp,en}}\eta_{\mathrm{coup}}\eta_{\mathrm{sp,ex}}, \tag{4.33}$$

$$\eta_{\mathrm{sp,en}}(\hat{\boldsymbol{p}}) := \frac{\iint_P |E_{\mathrm{inc}}(\hat{\boldsymbol{p}};\boldsymbol{\rho})|^2 \,\mathrm{d}^2\boldsymbol{\rho}}{\iint_{P_{\mathrm{ap}}} |E_{\mathrm{inc}}(\boldsymbol{\rho},\hat{\boldsymbol{p}})|^2 \,\mathrm{d}^2\boldsymbol{\rho}}, \tag{4.34}$$

$$\eta_{\mathrm{coup}}(\hat{\boldsymbol{p}};\boldsymbol{r}_{\mathrm{ref}}) := \frac{\left|\iint_P E_{\mathrm{inc}}(\hat{\boldsymbol{p}};\boldsymbol{\rho}) {E_{\mathrm{det}}}^*(\boldsymbol{\rho};\boldsymbol{r}_{\mathrm{ref}})\mathrm{d}^2\boldsymbol{\rho}\right|^2}{\iint_P |E_{\mathrm{inc}}(\hat{\boldsymbol{p}};\boldsymbol{\rho})|^2 \,\mathrm{d}^2\boldsymbol{\rho} \iint_P |E_{\mathrm{det}}(\boldsymbol{\rho};\boldsymbol{r}_{\mathrm{ref}})|^2 \,\mathrm{d}^2\boldsymbol{\rho}}, \tag{4.35}$$

$$\eta_{\mathrm{sp,ex}}(\boldsymbol{r}_{\mathrm{ref}}) := \frac{\iint_P |E_{\mathrm{det}}(\boldsymbol{\rho};\boldsymbol{r}_{\mathrm{ref}})|^2 \,\mathrm{d}^2\boldsymbol{\rho}}{\iint_{P_{\mathrm{det}}} |E_{\mathrm{det}}(\boldsymbol{\rho};\boldsymbol{r}_{\mathrm{ref}})|^2 \,\mathrm{d}^2\boldsymbol{\rho}}, \tag{4.36}$$

where interval P_{ap} is the area of the aperture, P_{det} is the area where the detector sensitivity makes an imaginary field at the exit pupil, and $P = P_{\mathrm{ap}} \cap P_{\mathrm{phys}} \cap P_{\mathrm{det}}$. Interval P_{phys} corresponds to the pupil, or aperture stop. If the case where the aperture works as an aperture stop and $P_{\mathrm{phys}} \subset P_{\mathrm{det}}$ is considered, $\eta_{\mathrm{sp,en}}(\hat{\boldsymbol{p}}) = 1$. "Traditional" taper efficiency η_{tap} corresponds to the product $\eta_{\mathrm{sp,en}}\eta_{\mathrm{coup}}$. A plane where the integrals (4.34–4.36) are calculated is set at an arbitrary pupil because spillover efficiencies are a constant at all the pupils and a coupling efficiency is an invariant in the whole system. The invariance of a coupling efficiency is proved in Appendix A.

Evaluation of Aperture Efficiency at Entrance Pupil

By evaluating Equations (4.33–4.36) at the entrance pupil, the relation between an aperture efficiency η_{A} and a beam solid angle Ω_{A} is obtained, which is seen in Equation (3.15). According to Equation (4.30), $E_{\mathrm{inc}}(\hat{\boldsymbol{p}}) = \exp\left[\sqrt{-1}kR_{\mathrm{p,en}}\rho\sin\Theta\cos\left(\psi-\Phi\right)\right]$. Focus on the beam pattern defined as

$$\tilde{P}(l,m;\boldsymbol{r}_{\mathrm{ref}}) := \lambda^4 \left| \iint_{P_{\mathrm{phys}}} E_{\mathrm{det}}\left(\frac{x}{\lambda},\frac{y}{\lambda};\boldsymbol{r}_{\mathrm{ref}}\right) \exp\left[-2\pi\sqrt{-1}\left(\frac{x}{\lambda}l+\frac{y}{\lambda}m\right)\right] \mathrm{d}\left(\frac{x}{\lambda}\right)\mathrm{d}\left(\frac{y}{\lambda}\right)\right|^2, \tag{4.37}$$

$$P(\Theta,\Phi;\boldsymbol{r}_{\mathrm{ref}}) := \cos\Theta\tilde{P}(l,m;\boldsymbol{r}_{\mathrm{ref}}), \tag{4.38}$$

where $x := R_{\mathrm{p,en}}\rho\cos\psi$, $y := R_{\mathrm{p,en}}\rho\sin\psi$, $l = \sin\Theta\cos\Phi$, and $m = \sin\Theta\sin\Phi$. See also Section (2.2.3). $\tilde{P}(l,m)$ equals the numerator of $\eta_{\mathrm{coup}}(\hat{\boldsymbol{p}};\boldsymbol{r}_{\mathrm{ref}})$ and E_{det} is not a Gaussian function obligatory. Applying the Wiener-Khinchin theorem to Equation (4.37),

$$\tilde{P}(l,m;\boldsymbol{r}_{\mathrm{ref}}) = \lambda^4 \iint \left[\iint_{P_{\mathrm{phys}}} E_{\mathrm{det}}\left(\frac{x}{\lambda},\frac{y}{\lambda};\boldsymbol{r}_{\mathrm{ref}}\right) E^*_{\mathrm{det}}\left(u+\frac{x}{\lambda},v+\frac{y}{\lambda};\boldsymbol{r}_{\mathrm{ref}}\right) \mathrm{d}\left(\frac{x}{\lambda}\right)\mathrm{d}\left(\frac{y}{\lambda}\right)\right] \times \exp\left[2\pi\sqrt{-1}(ul+vm)\right]\mathrm{d}u\mathrm{d}v, \tag{4.39}$$

and performing the Fourier transform,

$$\iint \tilde{P}(l,m;\boldsymbol{r}_{\mathrm{ref}}) \exp\left[-2\pi\sqrt{-1}(ul+vm)\right]\mathrm{d}l\mathrm{d}m = \lambda^4 \iint_{P_{\mathrm{phys}}} E_{\mathrm{det}}\left(\frac{x}{\lambda},\frac{y}{\lambda};\boldsymbol{r}_{\mathrm{ref}}\right) E^*_{\mathrm{det}}\left(u+\frac{x}{\lambda},v+\frac{y}{\lambda};\boldsymbol{r}_{\mathrm{ref}}\right) \mathrm{d}\left(\frac{x}{\lambda}\right)\mathrm{d}\left(\frac{y}{\lambda}\right). \tag{4.40}$$

When $u = v = 0$, the part of the denominator of $\eta_{\mathrm{coup}}(\hat{\boldsymbol{p}},\boldsymbol{r}_{\mathrm{ref}})$ appears,

$$\iint \tilde{P}(l,m;\boldsymbol{r}_{\mathrm{ref}})\mathrm{d}l\mathrm{d}m = \lambda^2 \iint_{P_{\mathrm{phys}}} \left|E_{\mathrm{det}}\left(\boldsymbol{\rho};\boldsymbol{r}_{\mathrm{ref}}\right)\right|^2 \mathrm{d}^2\boldsymbol{\rho}. \tag{4.41}$$

$\hat{\boldsymbol{p}}_0 = (\Theta_0,\Phi_0)$ is the direction which makes $\tilde{P}(l,m)$ be the maximum. (l_0,m_0) is the correspondence to $\hat{\boldsymbol{p}}_0$. The normalized beam pattern is defined as

$$\begin{aligned} \tilde{P}_{\mathrm{n}}(l,m;\boldsymbol{r}_{\mathrm{ref}}) &:= \frac{\tilde{P}(l,m;\boldsymbol{r}_{\mathrm{ref}})}{\tilde{P}(l_0,m_0;\boldsymbol{r}_{\mathrm{ref}})}, \\ P_{\mathrm{n}}(\Theta,\Phi;\boldsymbol{r}_{\mathrm{ref}}) &:= \cos\Theta\tilde{P}_n(l,m;\boldsymbol{r}_{\mathrm{ref}}). \end{aligned} \tag{4.42}$$

Substitution of Equation (4.42) into Equation (4.41) yields

$$\begin{aligned} \lambda^2 \iint_{P_{\mathrm{phys}}} \left|E_{\mathrm{det}}\left(\boldsymbol{\rho};\boldsymbol{r}_{\mathrm{ref}}\right)\right|^2 \mathrm{d}^2\boldsymbol{\rho} &= \tilde{P}(l_0,m_0;\boldsymbol{r}_{\mathrm{ref}}) \iint \tilde{P}_{\mathrm{n}}(l,m;\boldsymbol{r}_{\mathrm{ref}})\mathrm{d}l\mathrm{d}m \\ &= \tilde{P}(l_0,m_0;\boldsymbol{r}_{\mathrm{ref}})\Omega_{\mathrm{A}}(\boldsymbol{r}_{\mathrm{ref}}). \end{aligned} \tag{4.43}$$

By using Equations (4.37), (4.42), and (4.43), the same relation as shown in Equation (3.13) is obtained.

$$\eta_{\mathrm{coup}}(\hat{\boldsymbol{p}};\boldsymbol{r}_{\mathrm{ref}}) = \frac{\lambda^2\tilde{P}_n(l,m;\boldsymbol{r}_{\mathrm{ref}})}{A_{\mathrm{p,en}}\Omega_{\mathrm{A}}(\boldsymbol{r}_{\mathrm{ref}})}, \qquad A_{\mathrm{p,en}} := \pi {R_{\mathrm{p,en}}}^2. \tag{4.44}$$

Equation (4.44) shows that the direction of an incident plane wave and the position of the reference spherical wave center, i.e., the detector position determine a coupling efficiency via a beam

pattern $\tilde{P}_n(l, m; \boldsymbol{r}_{\rm ref})$. Finally, an aperture efficiency can be expressed as a function of $\hat{\boldsymbol{p}}$ and $\boldsymbol{r}_{\rm ref}$,

$$\eta_{\rm A}(\hat{\boldsymbol{p}}; \boldsymbol{r}_{\rm ref}) = \eta_{\rm sp,ex}(\boldsymbol{r}_{\rm ref}) \frac{\lambda^2 \tilde{P}_n(l, m; \boldsymbol{r}_{\rm ref})}{A_{\rm p,en}\Omega_{\rm A}(\boldsymbol{r}_{\rm ref})}. \tag{4.45}$$

In case if $\tilde{P}_n = 1$, i.e., $\hat{\boldsymbol{p}} = \hat{\boldsymbol{p}}_0$, Equation (4.45) reduces to

$$\eta_{\rm A}(\hat{\boldsymbol{p}}_0; \boldsymbol{r}_{\rm ref}) = \eta_{\rm sp,ex}(\boldsymbol{r}_{\rm ref}) \frac{\lambda^2}{A_{\rm p,en}\Omega_{\rm A}(\boldsymbol{r}_{\rm ref})}. \tag{4.46}$$

Note that $\eta_{\rm sp,en} = 1$ because the aperture is identified with the aperture stop. Equation (4.46) is different from the well-known form $\eta_{\rm A} = \lambda^2 / A_{\rm p,en}\Omega_{\rm A}$ described in numerous literature (e.g., Rohlfs & Wilson 2004, chap. 5), which is a special case when $\eta_{\rm sp,ex} = 1$ and $\tilde{P}_{\rm n}(l, m; \boldsymbol{r}_{\rm ref}) = 1$.

Evaluation of Aperture Efficiency at Exit pupil

The field reaching the exit pupil from the entrance pupil and the imaginary field by the detector sensitivity are expanded with the normalized Zernike annular polynomials (Appendix B). The use of the Zernike polynomials that are orthogonal polynomials in a finite and annular domain is more reasonable than the use of orthogonal polynomials defined in an infinite domain such as Laguerre-Gaussian beams.

Differences between the fields at the exit pupil and the reference spherical wave can be expanded such that

$$\begin{aligned} E_{\rm ex}(\hat{\boldsymbol{p}}; \boldsymbol{\rho}) = C \exp\left[\sqrt{-1} k \frac{f}{z_{\rm ref}} R_{\rm p,ex} \rho \sin\Theta \cos(\psi - \Phi) + \sqrt{-1} \frac{k {R_{\rm p,ex}}^2}{2 z_{\rm ref}} \rho^2\right] \\ \times \sum_{m,n} {C_n}^m(\hat{\boldsymbol{p}}; \boldsymbol{r}_{\rm ref}) {Z_n}^m(\boldsymbol{\rho}; \varepsilon), \end{aligned} \tag{4.47}$$

$$\begin{aligned} E_{\rm det}(\boldsymbol{\rho}; \boldsymbol{r}_0) = C' \exp\left[\sqrt{-1} k \frac{f}{z_{\rm ref}} R_{\rm p,ex} \rho \sin\Theta \cos(\psi - \Phi) + \sqrt{-1} \frac{k {R_{\rm p,ex}}^2}{2 z_{\rm ref}} \rho^2\right] \\ \times \sum_{p,q} {D_p}^q(\boldsymbol{r}_{\rm ref}; \boldsymbol{r}_0; w_0) {Z_p}^q(\boldsymbol{\rho}; \varepsilon). \end{aligned} \tag{4.48}$$

$E_{\rm ex}$ and $E_{\rm det}$ represent the field at the exit pupil by the incident wave and the detector sensitivity, respectively. C and C' are constants. It is assumed that the detector sensitivity is expanded using the Laguerre-Gaussian beams at either the exit pupil plane or another plane. Coefficients ${D_p}^q$ depend on the beam waist size of the Laguerre-Gaussian beams, w_0, and the beam waist position connected with $\boldsymbol{r}_{\rm ref}$. Using Equations (4.47) and (4.48), the coupling efficiency can be written as

follows:

$$\eta_{\mathrm{coup}} = \frac{\left|\sum_{m,n}\sum_{p,q}\delta_{np}\delta_{mq}{C_n}^m(\hat{\boldsymbol{p}};\boldsymbol{r}_{\mathrm{ref}})\left({D_p}^q(\boldsymbol{r}_{\mathrm{ref}};\boldsymbol{r}_0;w_0)\right)^*\right|^2}{\sum_{n,m}\left|{C_n}^m(\hat{\boldsymbol{p}};\boldsymbol{r}_{\mathrm{ref}})\right|^2\sum_{p,q}\left|{D_p}^q(\boldsymbol{r}_{\mathrm{ref}};\boldsymbol{r}_0;w_0)\right|^2}, \tag{4.49}$$

where δ_{np} is the Kronecker delta. Coefficients ${C_n}^m$ hold information about the wavefront distorted by aberrations.

4.3.3 Relation between Aberration Coefficients and Aperture efficiency

The calculation of coefficients ${C_n}^m$ and ${D_p}^q$ is performed. The response of an aperture efficiency can be observed via Equation (4.49) in case where Seidel aberrations exist.

First, expand wavefront error $W(\hat{\boldsymbol{p}};\boldsymbol{\rho};\boldsymbol{r}_{\mathrm{ref}})$ using the Zernike annular polynomials corresponding to Seidel aberrations and determine coefficients ${C_n}^m(\hat{\boldsymbol{p}};\boldsymbol{r}_{\mathrm{ref}})$. Zernike polynomials ${Z_n}^m$ that meet the following conditions are used: $n+m\leq 4$, $n-|m|\geq 0$, and $n-|m|$ is even. Then,

$$\begin{aligned}
W(\hat{\boldsymbol{p}};\boldsymbol{\rho};\boldsymbol{r}_{\mathrm{ref}}) = {}& {A_1}^1(\hat{\boldsymbol{p}};\boldsymbol{r}_{\mathrm{ref}}){Z_1}^1(\boldsymbol{\rho};\varepsilon) + {B_1}^1(\hat{\boldsymbol{p}};\boldsymbol{r}_{\mathrm{ref}}){Z_1}^{-1}(\boldsymbol{\rho};\varepsilon)\\
&+ {A_2}^0(\hat{\boldsymbol{p}};\boldsymbol{r}_{\mathrm{ref}}){Z_2}^0(\boldsymbol{\rho};\varepsilon) + {A_2}^2(\hat{\boldsymbol{p}};\boldsymbol{r}_{\mathrm{ref}}){Z_2}^2(\boldsymbol{\rho};\varepsilon)\\
&+ {B_2}^2(\hat{\boldsymbol{p}};\boldsymbol{r}_{\mathrm{ref}}){Z_2}^{-2}(\boldsymbol{\rho};\varepsilon) + {A_3}^1(\hat{\boldsymbol{p}};\boldsymbol{r}_{\mathrm{ref}}){Z_3}^1(\boldsymbol{\rho};\varepsilon)\\
&+ {B_3}^1(\hat{\boldsymbol{p}};\boldsymbol{r}_{\mathrm{ref}}){Z_3}^{-1}(\boldsymbol{\rho};\varepsilon) + {A_4}^0(\hat{\boldsymbol{p}};\boldsymbol{r}_{\mathrm{ref}}){Z_4}^0(\boldsymbol{\rho};\varepsilon).
\end{aligned} \tag{4.50}$$

The meanings of coefficients ${A_n}^m$ and ${B_n}^m$ are summarized in Table 4.1. The field at the exit pupil can be expressed using the terms up to the second order W^2

$$\begin{aligned}
E_{\mathrm{ex}}(\hat{\boldsymbol{p}};\boldsymbol{\rho}) &\simeq \frac{R_{\mathrm{p,en}}}{R_{\mathrm{p,ex}}}\exp\left[\sqrt{-1}k\frac{f}{z_{\mathrm{ref}}}R_{\mathrm{p,ex}}\rho\sin\Theta\cos(\psi-\Phi)+\sqrt{-1}\frac{k{R_{\mathrm{p,ex}}}^2}{2z_{\mathrm{ref}}}\rho^2\right]\\
&\quad\times\left(1+\sqrt{-1}kW-\frac{k^2}{2}W^2\right)\\
&= \frac{R_{\mathrm{p,en}}}{R_{\mathrm{p,ex}}}\exp\left[\sqrt{-1}k\frac{f}{z_{\mathrm{ref}}}R_{\mathrm{p,ex}}\rho\sin\Theta\cos(\psi-\Phi)+\sqrt{-1}\frac{k{R_{\mathrm{p,ex}}}^2}{2z_{\mathrm{ref}}}\rho^2\right]\\
&\quad\times\sum_{n,m}{C_n}^m(\hat{\boldsymbol{p}};\boldsymbol{r}_{\mathrm{ref}}){Z_n}^m(\boldsymbol{\rho};\boldsymbol{r}_{\mathrm{ref}}).
\end{aligned} \tag{4.51}$$

Coefficients ${C_n}^m$ as functions of ${A_n}^m$ and ${B_n}^m$ are shown in Appendix C.

Next, consider coefficients ${D_p}^q(\boldsymbol{r}_{\mathrm{ref}};\boldsymbol{r}_0;w_0)$. In the ideal case, the field distribution of the detector sensitivity is a Gaussian function. The distribution is given as a superposition of the Laguerre-Gaussian beams and expanded by using the Zernike annular polynomials.

Before calculating coefficients ${D_p}^q$, take a brief look at the propagation of beams. The incident wave from direction $\hat{\boldsymbol{p}}$ is converted into a nearly spherical wave centered at $\boldsymbol{r}_{\mathrm{ref}}$. It is assumed that

Table 4.1: Aberration coefficients.

${A_1}^1(\hat{\boldsymbol{p}};\boldsymbol{r}_{\rm ref}),\ {B_1}^1(\hat{\boldsymbol{p}};\boldsymbol{r}_{\rm ref})$	tip, tilt, distortion
${A_2}^0(\hat{\boldsymbol{p}};\boldsymbol{r}_{\rm ref})$	defocus, curvature of field
${A_2}^2(\hat{\boldsymbol{p}};\boldsymbol{r}_{\rm ref}),\ {B_2}^2(\hat{\boldsymbol{p}};\boldsymbol{r}_{\rm ref})$	astigmatism
${A_3}^1(\hat{\boldsymbol{p}};\boldsymbol{r}_{\rm ref}),\ {B_3}^1(\hat{\boldsymbol{p}};\boldsymbol{r}_{\rm ref})$	coma
${A_4}^0(\hat{\boldsymbol{p}};\boldsymbol{r}_{\rm ref})$	spherical

the position of beam waist $\boldsymbol{r}_0$ is on the line connecting the exit pupil center and point $\boldsymbol{r}_{\rm ref}$, along which the Laguerre-Gaussian beams propagate. Hence, term $\exp[\sqrt{-1}k(f/z_{\rm ref})R_{\rm p,ex}\rho\sin\Theta\cos(\psi-\Phi)]$ can be ignored, which means that the case to be considered is the on-axis case only, i.e., a wave is incident along the normal to the pupil, and the beam waist is located on the z-axis. In the following sections, it is assumed that $\boldsymbol{r}_0 \propto \boldsymbol{r}_{\rm ref}$ and the beam waist is located at point $\boldsymbol{r}_0 = (0, 0, z_0)$ with a beam size of w_0.

Each mode of the Laguerre-Gaussian beams specified by indexes p' and q' can be expanded using the Zernike polynomials within an annulus. $p'q'$ Gaussian beam mode is given by

$$E_{p'}{}^{q'}(\boldsymbol{\rho};\boldsymbol{r}_0;w_0) = \sqrt{\frac{2Tp'!}{\pi(p'+|q'|)!}}\left(\sqrt{2T}\rho\right)^{|q'|} L_{p'}{}^{|q'|}\left(2T\rho^2\right) \times \exp\left[-T\rho^2 + \sqrt{-1}kz_0 + \sqrt{-1}\frac{kTw(0)^2\rho^2}{2R(0)} + \sqrt{-1}(2p'+|q'|+1)\phi(0) + \sqrt{-1}q'\psi\right], \tag{4.52}$$

$$T := \frac{{R_{\rm p,ex}}^2}{w^2(0)}, \tag{4.53}$$

$$w(z) := w_0\sqrt{1+\left(\frac{2(z-z_0)}{k{w_0}^2}\right)^2}, \tag{4.54}$$

$$R(z) := -(z-z_0)\left[1+\left(\frac{k{w_0}^2}{2(z-z_0)}\right)^2\right], \tag{4.55}$$

$$\phi(z) := \tan^{-1}\frac{2(z-z_0)}{k{w_0}^2}. \tag{4.56}$$

Note that T corresponds to the edge taper in decibel. By using coefficients $F_{p'}{}^{q'}$, the detector sensitivity at the exit pupil can be written as

$$E_{\rm det}(\boldsymbol{\rho};\boldsymbol{r}_0) = \sum_{p',q'} F_{p'}{}^{q'}E_{p'}{}^{q'}(\boldsymbol{\rho};\boldsymbol{r}_0;w_0). \tag{4.57}$$

Following Equation (4.48), Equation (4.52) is re-arranged using the expression of the Laguerre

polynomials as a series (Gradshteyn et al. 2007, p. 1000)

$$
\begin{aligned}
{E_{p'}}^{q'}(\boldsymbol{\rho};\boldsymbol{r}_0;w_0) &= \sqrt{\frac{2Tp'!}{\pi(p'+|q'|)!}}\exp\left[\sqrt{-1}kz_0+\sqrt{-1}\phi(0)+\sqrt{-1}\frac{kTw(0)^2\rho^2}{2z_{\mathrm{ref}}}\right] \\
&\quad\times\sqrt{2T}^{|q'|}\exp\left[\sqrt{-1}(2p'+|q'|)\phi(0)\right]\sum_{s=0}^{p'}\binom{p'+|q'|}{p'-s}\frac{(-2T)^s}{s!}\rho^{|q'|+2s} \\
&\quad\times\exp\left[\alpha(\boldsymbol{r}_{\mathrm{ref}};\boldsymbol{r}_0;w_0)\rho^2\right]\left[\cos(q'\psi)+\sqrt{-1}\sin(q'\psi)\right] \\
&= \sqrt{\frac{2T}{\pi}}\exp\left[\sqrt{-1}kz_0+\sqrt{-1}\phi(0)+\sqrt{-1}\frac{kTw(0)^2\rho^2}{2z_{\mathrm{ref}}}\right]\sum_{p,q}\tilde{D}_p{}^q Z_p{}^q, \qquad (4.58)
\end{aligned}
$$

where

$$
\alpha(\boldsymbol{r}_{\mathrm{ref}};\boldsymbol{r}_0;w_0) = -T+\sqrt{-1}\frac{kTw^2(0)}{2}\left(\frac{1}{R(0)}-\frac{1}{z_{\mathrm{ref}}}\right). \qquad (4.59)
$$

The polynomials in Table B.1 and their orthogonality enable to integrate by ψ and result in

$$
\begin{aligned}
\tilde{D}_p{}^q(p',q';w_0) &= \delta_{qq'}\sqrt{\frac{p'!(p+1)(1+\delta_{q0})(q+\delta_{q0})}{2(p'+|q|)!(|q|+\delta_{t0})}}\exp\left[\sqrt{-1}(2p'+|q|)\phi(0)\right]\frac{\sqrt{2T}^{|q|}}{\sqrt{1-\varepsilon^2}} \\
&\quad\times\sum_{u=0}^{p'}\binom{p'+|q|}{p'-u}\frac{(-2T)^u}{u!}\int_{\varepsilon}^{1}{R_p}^{|q|}(\rho;\varepsilon)\rho^{|q|+2u}\exp\left[\alpha(\boldsymbol{r}_{\mathrm{ref}};\boldsymbol{r}_0;w_0)\rho^2\right]\mathrm{d}(\rho^2). \qquad (4.60)
\end{aligned}
$$

${R_p}^{|q|}$ is the p-th order polynomial and $p+|q|\leq 8$ is a positive even number. By using integral

$$
\begin{aligned}
I_{2\mu}(\boldsymbol{r}_{\mathrm{ref}};\boldsymbol{r}_0;w_0) &:= \int_{\varepsilon}^{1}\rho^{2\mu}\exp\left[\alpha(\boldsymbol{r}_{\mathrm{ref}};\boldsymbol{r}_0;w_0)\rho^2\right]\mathrm{d}(\rho^2) \\
&= \frac{\mu!}{\alpha}\sum_{\nu=0}^{\mu}\frac{(-\alpha)^{\nu-\mu}}{\nu!}\left[\exp(\alpha)-\varepsilon^{2\nu}\exp(\alpha\varepsilon^2)\right], \qquad (4.61)
\end{aligned}
$$

and polynomial $\tilde{R}_p{}^{|q|}(I_{p+|q|+2u})$ defined in Table B.2,

$$
\begin{aligned}
\tilde{D}_p{}^q(p',q';w_0) &= \delta_{qq'}\sqrt{\frac{p'!(p+1)(1+\delta_{q0})(q+\delta_{q0})}{2(p'+|q|)!(|q|+\delta_{q0})}}\exp\left[\sqrt{-1}(2p'+|q|)\phi(0)\right]\frac{\sqrt{2T}^{|q|}}{\sqrt{1-\varepsilon^2}} \\
&\quad\times\sum_{u=0}^{p'}\binom{p'+|q|}{p'-u}\frac{(-2T)^u}{u!}\tilde{R}_p{}^{|q|}(I_{p+|q|+2u}). \qquad (4.62)
\end{aligned}
$$

Thus, coefficients ${D_p}^q(\boldsymbol{r}_{\rm ref};\boldsymbol{r}_0;w_0)$ are as follows:

$$\begin{aligned}
{D_p}^q(\boldsymbol{r}_{\rm ref};\boldsymbol{r}_0;w_0) &= \sum_{p',q'} {F_{p'}}^{q'}\tilde{D}_p{}^q(p',q';w_0) \\
&= \sum_{p',q'} {F_{p'}}^{q'}\delta_{qq'}\sqrt{\frac{p'!(p+1)(1+\delta_{q0})(q+\delta_{q0})}{2(p'+|q|)!(|q|+\delta_{q0})}}\exp\left[\sqrt{-1}(2p'+|q|)\phi(0)\right]\frac{\sqrt{2T}^{|q|}}{\sqrt{1-\varepsilon^2}} \\
&\quad\times\sum_{u=0}^{p'}\binom{p'+|q|}{p'-u}\frac{(-2T)^u}{u!}\tilde{R}_p{}^{|q|}(I_{p+|q|+2u}).
\end{aligned} \tag{4.63}$$

In case of the fundamental mode, ${F_0}^0=1$ and ${F_{p'}}^{q'}=0$ for the other p' and q', Equation (4.63) reduces to

$${D_p}^0=\frac{\sqrt{p+1}}{\sqrt{1-\varepsilon^2}}\tilde{R}_p{}^0(I_p). \tag{4.64}$$

The following notation for polynomials of ε^2 is adopted:

$$[a,b,c,\cdots]:=a+b\varepsilon^2+c\varepsilon^4+\cdots. \tag{4.65}$$

Coefficients ${D_p}^0$ $(p\le 8)$ are given:

$$\begin{aligned}
{D_0}^0 &= \tilde{R}_0{}^0(I_0)=-\frac{\exp(\alpha\varepsilon^2)-\exp(\alpha)}{\alpha\,[1,-1]}, \\
{D_2}^0 &= \tilde{R}_2{}^0(I_2)=\frac{\sqrt{3}}{\alpha^2\,[1,-1]^2}\left\{[2+\alpha,-\alpha]\exp\left(\alpha\varepsilon^2\right)-[2-\alpha,\alpha]\exp(\alpha)\right\}, \\
{D_4}^0 &= \tilde{R}_4{}^0(I_4)=\frac{-\sqrt{5}}{\alpha^3\,[1,-1]^3}\left\{\left[12+6\alpha+\alpha^2,-6\alpha-2\alpha^2,\alpha^2\right]\exp\left(\alpha\varepsilon^2\right)\right. \\
&\qquad\left.-\left[12-6\alpha+\alpha^2,6\alpha-2\alpha^2,\alpha^2\right]\exp(\alpha)\right\}, \\
{D_6}^0 &= \tilde{R}_6{}^0(I_6) \\
&= \frac{\sqrt{7}}{\alpha^4\,[1,-1]^4}\left\{\left[120+60\alpha+12\alpha^2+\alpha^3,-60\alpha-24\alpha^2-3\alpha^3,12\alpha^2+3\alpha^3,-\alpha^3\right]\exp\left(\alpha\varepsilon^2\right)\right. \\
&\qquad\left.-\left[120-60\alpha+12\alpha^2-\alpha^3,60\alpha-24\alpha^2+3\alpha^3,12\alpha^2-3\alpha^3,\alpha^3\right]\exp(\alpha)\right\}, \\
{D_8}^0 &= \tilde{R}_8{}^0(I_8) \\
&= \frac{-3}{\alpha^5\,[1,-1]^5}\left\{\left[1680+840\alpha+180\alpha^2+20\alpha^3+\alpha^4,-840\alpha-360\alpha^2-60\alpha^3-4\alpha^4,\right.\right. \\
&\qquad\left.180\alpha^2+60\alpha^3+6\alpha^4,-20\alpha^3-4\alpha^4,\alpha^4\right]\exp\left(\alpha\varepsilon^2\right) \\
&\qquad-\left[1680-840\alpha+180\alpha^2-20\alpha^3+\alpha^4,840\alpha-360\alpha^2+60\alpha^3-4\alpha^4,\right. \\
&\qquad\left.\left.180\alpha^2-60\alpha^3+6\alpha^4,20\alpha^3-4\alpha^4,\alpha^4\right]\exp(\alpha)\right\}.
\end{aligned}$$

4.3.4 Response of Aperture Efficiency

The response of Equation (4.49) as a function of parameter T can be observed. The detector sensitivity is assumed to be a fundamental Gaussian beam.

First, the case where there are no aberrations is considered, i.e., ${C_0}^0 = 1$ and ${C_n}^m = 0$ for the other n and m. Equation (4.49) reduces to

$$\eta_{\text{coup}} = \frac{\left|{C_0}^0 \left({D_0}^0\right)^*\right|^2}{\sum_{n,m} |{C_n}^m|^2 \sum_{p,q} |{D_p}^q|^2} \tag{4.66}$$

Using ${D_0}^0 = {\tilde{R}_0}^0$

$$\eta_{\text{coup}} = \frac{1}{\sum_{n,m} |{C_n}^m|^2 \sum_{p,q} |{D_p}^q|^2} \frac{\left|\exp(\alpha\varepsilon^2) - \exp(\alpha)\right|^2}{|\alpha|^2 \left[1,-1\right]^2}. \tag{4.67}$$

The summation of $|{C_n}^m|^2$ and $|{D_p}^q|^2$ exhibits all the power passing through the pupil from an object and a detector, respectively, and therefore, the relations are derived,

$$\sum_{n,m} |{C_n}^m|^2 = 1 \tag{4.68}$$

$$\sum_{p,q} |{D_p}^q|^2 = \frac{1}{\pi[1,-1]} \int_0^{2\pi} \int_\varepsilon^1 \rho \mathrm{d}\rho \exp(-2T\rho^2) = \frac{\exp(-2T\varepsilon^2) - \exp(-2T)}{2T[1,-1]}. \tag{4.69}$$

Spillover efficiencies can be calculated according to Equations (4.34) and (4.36)

$$\eta_{\text{sp,en}} = 1 \tag{4.70}$$

$$\eta_{\text{sp,ex}} = \exp(-2T\varepsilon^2) - \exp(-2T) \tag{4.71}$$

Then, an aperture efficiency in no aberrations is obtained.

$$\eta_{\text{coup}} = \frac{2T\left|\exp(\alpha\varepsilon^2) - \exp(\alpha)\right|^2}{|\alpha|^2 \left[1,-1\right] \left[\exp(-2T\varepsilon^2) - \exp(-2T)\right]}, \tag{4.72}$$

$$\eta_{\text{A}} = \frac{2T\left|\exp(\alpha\varepsilon^2) - \exp(\alpha)\right|^2}{|\alpha|^2 \left[1,-1\right]}. \tag{4.73}$$

When $\varepsilon = 0$ and $R(0) = z_{\text{ref}}$, an aperture efficiency can be simply expressed as

$$\eta_{\text{A}} = \frac{2\left[1 - \exp(-T)\right]^2}{T}. \tag{4.74}$$

Next, consider the case where an optical system has aberrations. If the system is composed of axially symmetric elements, it can be assumed that ${B_1}^1 = 0$, ${A_2}^2 = 0$, and ${B_3}^1 = 0$. It is also

assumed for simplicity that $\varepsilon = 0$, $R(0) = z_{\mathrm{ref}}$, and the detector sensitivity is in a fundamental Gaussian mode. As a result, coefficients ${C_n}^0$ and ${D_p}^0$ are calculated.

$$
\begin{aligned}
{C_0}^0 &= 1 - \frac{k^2}{2}\left[\left({A_1}^1\right)^2 + \left({A_2}^0\right)^2 + \left({B_2}^2\right)^2 + \left({A_3}^1\right)^2 + \left({A_4}^0\right)^2\right], \\
{C_2}^0 &= jk{A_2}^0 - \frac{k^2}{2}\left[\frac{\left({A_1}^1\right)^2}{\sqrt{3}} + \frac{2\sqrt{2}{A_1}^1{A_3}^1}{\sqrt{3}} + \frac{4{A_2}^0{A_4}^0}{\sqrt{5}} + \frac{\sqrt{3}\left({B_2}^2\right)^2}{2} + \frac{\left({A_3}^1\right)^2}{5\sqrt{3}}\right], \\
{C_4}^0 &= jk{A_4}^0 - \frac{k^2}{2}\left[\frac{2\sqrt{2}{A_1}^1{A_3}^1}{\sqrt{5}} + \frac{2\left({A_2}^0\right)^2}{\sqrt{5}} + \frac{\left({B_2}^2\right)^2}{2\sqrt{5}} + \frac{\left({A_3}^1\right)^2}{\sqrt{5}} + \frac{2\sqrt{5}\left({A_4}^0\right)^2}{7}\right], \\
{C_6}^0 &= -\frac{k^2}{10\sqrt{7}}\left[6\sqrt{15}{A_2}^0{A_4}^0 + 9\left({A_3}^1\right)^2\right], \\
{C_8}^0 &= -\frac{3k^2}{7}\left({A_4}^0\right)^2,
\end{aligned}
$$

$$
\begin{aligned}
{D_0}^0 &= \frac{1-\exp(-T)}{T}, \\
{D_2}^0 &= \frac{\sqrt{3}}{T^2}\left[2 - T - (2+T)\exp(-T)\right], \\
{D_4}^0 &= \frac{\sqrt{5}}{T^3}\left[12 - 6T + T^2 - (12+6T+T^2)\exp(-T)\right], \\
{D_6}^0 &= \frac{\sqrt{7}}{T^4}\left[120 - 60T + 12T^2 - T^3 - (120+60T+12T^2+T^3)\exp(-T)\right], \\
{D_8}^0 &= \frac{3}{T^5}\left[1680 - 840T + 180T^2 - 20T^3 + T^4 - (1680+840T+180T^2+20T^3+T^4)\exp(-T)\right].
\end{aligned}
$$

By using coefficients ${C_n}^0$ and ${D_p}^0$, the aperture efficiency affected by Seidel aberrations is acquired,

$$
\begin{aligned}
\eta_{\mathrm{A}} = 2T\Bigg|{D_0}^0 + jk\left({A_2}^0{D_2}^0 + {A_4}^0{D_4}^0\right) - \frac{k^2}{2}\Bigg[&\left({D_0}^0 + \frac{{D_2}^0}{\sqrt{3}}\right)\left({A_1}^1\right)^2 + 2\sqrt{2}\left(\frac{{D_2}^0}{\sqrt{3}} + \frac{{D_4}^0}{\sqrt{5}}\right){A_1}^1{A_3}^1 \\
&+ \left({D_0}^0 + \frac{{D_2}^0}{5\sqrt{3}} + \frac{{D_4}^0}{\sqrt{5}} + \frac{9{D_6}^0}{5\sqrt{7}}\right)\left({A_3}^1\right)^2 + \left({D_0}^0 + \frac{2{D_4}^0}{\sqrt{5}}\right)\left({A_2}^0\right)^2 \\
&+ \left(\frac{4{D_2}^0}{\sqrt{5}} + \frac{6\sqrt{15}{D_6}^0}{5\sqrt{7}}\right){A_2}^0{A_4}^0 + \left({D_0}^0 + \frac{2\sqrt{5}{D_4}^0}{7} + \frac{6{D_8}^0}{7}\right)\left({A_4}^0\right)^2 \\
&+ \left({D_0}^0 + \frac{\sqrt{3}{D_2}^0}{2} + \frac{{D_4}^0}{2\sqrt{5}}\right)\left({B_2}^2\right)^2\Bigg]\Bigg|^2
\end{aligned}
\tag{4.75}
$$

Aberration coefficients ${A_1}^1$ and ${A_2}^0$ correspond to tip-tilt and defocus, respectively, and therefore, they are strongly dependent on beam waist position $\boldsymbol{r}_0$ or $\boldsymbol{r}_{\mathrm{ref}}$. Focus on the first order W. If the

beam waist is at the position which satifies

$$A_2{}^0(\hat{\boldsymbol{p}};\boldsymbol{r}_{\mathrm{ref}}) = -\frac{D_4{}^0(T)}{D_2{}^0(T)} A_4{}^0(\hat{\boldsymbol{p}};\boldsymbol{r}_{\mathrm{ref}}), \tag{4.76}$$

then the first order term vanishes. Equation (4.77) represents the condition to reduce effects of spherical aberration. In the same way, the second order W^2 as a function of $A_1{}^1$ is a minimum when the beam waist position satisfies

$$A_1{}^1(\hat{\boldsymbol{p}};\boldsymbol{r}_{\mathrm{ref}}) = -\frac{\sqrt{10}D_2{}^0(T) + \sqrt{6}D_4{}^0(T)}{\sqrt{15}D_0{}^0(T) + \sqrt{5}D_2{}^0(T)} A_3{}^1(\hat{\boldsymbol{p}};\boldsymbol{r}_{\mathrm{ref}}). \tag{4.77}$$

Equation (4.76) represents the condition to reduce effects of coma. Substituting Equations (4.76) and (4.77) into Equation (4.75) yields

$$\begin{aligned}\eta_{\mathrm{A}} = 2T \Bigg| D_0{}^0 - 2\pi^2 \Bigg\{ & \left(D_0{}^0 + \frac{D_2{}^0}{5\sqrt{3}} + \frac{D_4{}^0}{\sqrt{5}} + \frac{9D_6{}^0}{5\sqrt{7}} - \frac{2}{5\sqrt{3}} \frac{(\sqrt{5}D_2{}^0 + \sqrt{3}D_4{}^0)^2}{\sqrt{3}D_0{}^0 + D_2{}^0} \right) \left(\frac{A_3{}^1}{\lambda} \right)^2 \\ & + \left[\left(1 + \frac{\left(D_4{}^0\right)^2}{\left(D_2{}^0\right)^2} \right) D_0{}^0 - \frac{2}{7\sqrt{5}} \left(9 - 7\frac{\left(D_4{}^0\right)^2}{\left(D_2{}^0\right)^2} \right) D_4{}^0 - \frac{6\sqrt{15}D_4{}^0}{5\sqrt{7}D_2{}^0} D_6{}^0 + \frac{6}{7} D_8{}^0 \right] \left(\frac{A_4{}^0}{\lambda} \right)^2 \\ & + \left(D_0{}^0 + \frac{\sqrt{3}D_2{}^0}{2} + \frac{D_4{}^0}{2\sqrt{5}} \right) \left(\frac{B_2{}^2}{\lambda} \right)^2 \Bigg\} \Bigg|^2 . \end{aligned} \tag{4.78}$$

Conditions (4.76) and (4.77) do not maximize an aperture efficiency necessarily. If an asymmetric sensitivity is considered, e.g., a diagonal horn, one can obtain conditions to reduce effects of aberrations including astigmatism.

4.3.5 Verification

In this section, Equation (4.75) and conditions (4.76) and (4.77) are verified using numerical simulation. The results of ray tracing (Radiant Zemax 2014) and PO simulation (TICRA Engineering Consultants 2003) are compared.

A simple system is used for verification, which is composed of a spherical mirror with the circular aperture $\varepsilon = 0$ (Figure 4.11, Table 4.2). The wavelength is 200 μm. The incident angles are $\hat{\boldsymbol{p}} = (0\ \mathrm{deg.}, 0\ \mathrm{deg.})$ and $\hat{\boldsymbol{p}} = (1\ \mathrm{deg.}, 0\ \mathrm{deg.})$. Three cases in terms of the reference spherical wave center $\boldsymbol{r}_{\mathrm{ref}}$ are considered for each incident angle. $\boldsymbol{r}_{\mathrm{ref}}$ is located at the point where

1. Equations (4.76) and (4.77) hold when the edge taper is 15 dB,
2. the Strehl ratio without apodization is maximized,
3. the Gaussian image point is located.

Table 4.2: Parameters of the mirror.

Radius of curvature	-1000 mm
Conic constant	0.0
Diameter	300 mm

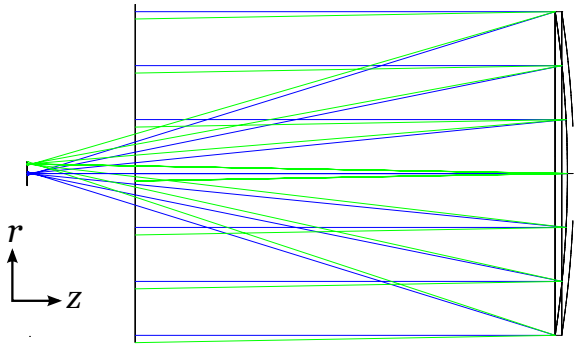

Figure 4.11: Schematics of the model.

Aberration coefficients ${A_n}^m$ and ${B_n}^m$ are derived through ray tracing. An edge taper is estimated using PO simulation. An aperture efficiency is calculated using Equation (4.75) as a function of the aberration coefficients and the edge taper. A Strehl ratio is also calculated by using the aberration coefficients (Mahajan 1983).

$$
\begin{aligned}
S(\hat{\boldsymbol{p}}; \boldsymbol{r}_{\rm ref}) &\simeq \exp\left[-k^2 {W_{\rm dev}}^2(\hat{\boldsymbol{p}}; \boldsymbol{r}_{\rm ref})\right] \\
&= \exp\left\{-k^2 \sum_{m\geq 0}\sum_{n>0}\left[({A_n}^m(\hat{\boldsymbol{p}}; \boldsymbol{r}_{\rm ref}))^2 + ({B_n}^m(\hat{\boldsymbol{p}}; \boldsymbol{r}_{\rm ref}))^2\right]\right\}. \qquad (4.79)
\end{aligned}
$$

Note that the Strehl ratio with apodization can be used as shown in Olmi & Bolli (2007) but pure geometrical features are needed in this discussion. Therefore, "Strehl ratio" imply the quantity defined in Equation (4.79).

In the PO simulation, a fundamental Gaussian beam propagating along vector $\boldsymbol{r}_{\rm ref}$ is used. The size and position of a beam waist are determined so that $R(0) = \sqrt{{r_{\rm ref}}^2 + {z_{\rm ref}}^2}$. An edge taper is set to approximately 5, 10, 15, and 20 dB. The specific values of spillover efficiencies, edge tapers, and beam solid angles are derived from the PO simulation. Then aperture efficiencies are calculated using Equation (4.46).

Case: $\hat{\boldsymbol{p}} =$ (0 deg., 0 deg.)

Coordinates $\boldsymbol{r}_{\rm ref}$, aberration coefficients calculated through ray tracing, and the Strehl ratio for each case are summarized in Table 4.3. The beam waist positions, the spillover efficiencies, and the beam solid angles are shown in Table 4.4. The aperture efficiencies estimated using Equation (4.75), $\eta_{\rm A,an}$, agree with that calculated using Equation (4.46), $\eta_{\rm A,PO}$, through PO simulation for

Table 4.3: Coordinates of $\boldsymbol{r}_{\rm ref}$, Strehl ratio, r.m.s. of fitting residuals, and aberration coefficients for $\hat{\boldsymbol{p}} = (0\ \mathrm{deg.}, 0\ \mathrm{deg.})$.

case	$(r_{\rm ref}, z_{\rm ref})/\mathrm{mm}$	Strehl ratio	r.m.s./λ
1	$(0, -497.330)$	0.9114	1.4×10^{-4}
2	$(0, -497.169)$	0.9150	1.4×10^{-4}
3	$(0, -500.0000)$	0.2527	1.4×10^{-4}

case	${A_1}^1/\lambda$	${A_2}^0/\lambda$	${B_2}^2/\lambda$	${A_3}^1/\lambda$	${A_4}^0/\lambda$
1	0	0.010342	0	0	0.047365
2	0	0	0	0	0.047426
3	0	0.180814	0	0	0.046364

Table 4.4: Beam waist position, spillover, and beam solid angle for $\hat{\boldsymbol{p}} = (0\ \mathrm{deg.}, 0\ \mathrm{deg.})$.

case	$(r_0, z_0)/\mathrm{mm}$	$\eta_{\rm sp,ex}$	$\Omega_{\rm A}/\mathrm{sr}$
1	$(0, -497.329)$	0.7158	6.349×10^{-7}
	$(0, -497.328)$	0.9079	6.873×10^{-7}
	$(0, -497.327)$	0.9701	7.679×10^{-7}
	$(0, -497.324)$	0.9903	8.728×10^{-7}
2	$(0, -497.168)$	0.7158	6.365×10^{-7}
	$(0, -497.167)$	0.9079	6.927×10^{-7}
	$(0, -497.166)$	0.9701	7.773×10^{-7}
	$(0, -497.163)$	0.9903	8.865×10^{-7}
3	$(0, -500.000)$	0.7156	1.968×10^{-6}
	$(0, -499.999)$	0.9078	1.705×10^{-6}
	$(0, -499.997)$	0.9701	1.564×10^{-6}
	$(0, -499.995)$	0.9903	1.506×10^{-6}

higher Strehl ratios (Table 4.5). Figure 4.12 shows points obtained through PO simulation and theoretical curves obtained using Equation (4.75) as a function of edge taper $T_{\rm e}$.

Case: $\hat{\boldsymbol{p}} =$ (1 deg., 0 deg.)

In the same way seen in the case $\hat{\boldsymbol{p}} =$ (1 deg., 0 deg.), coordinates $\boldsymbol{r}_{\rm ref}$, aberration coefficients, and the Strehl ratio are tabulated (Table 4.6). The beam waist positions, the spillover efficiencies, and teh beam solid angles are shown in Table 4.7. The aperture efficiencies estimated using Equation (4.75), $\eta_{\rm A,an}$, agree with that calculated using Equation (4.46), $\eta_{\rm A,PO}$, through PO simulation for higher Strehl ratios (Table 4.8). Figure 4.13 shows points obtained through PO simulation and theoretical curves obtained using Equation (4.75) as a function of edge taper T.

Figure 4.14 shows the beam pattern on the meridional plane. The peak values and the positions are different among the cases 1, 2, and 3 (Table 4.9). When condition (4.77) holds, there may be a possibility to reduce pointing errors due to the third-order coma. Condition (4.77) is practically useful to design a wide field-of-view radio telescope.

Table 4.5: Aperture efficiencies obtained using Equations (4.75) and (4.46), and the difference between them for $\hat{\boldsymbol{p}} = (0\ \mathrm{deg.}, 0\ \mathrm{deg.})$.

case	T_e	$\eta_\mathrm{A,an}$	$\eta_\mathrm{A,PO}$	$\eta_\mathrm{A,an}/\eta_\mathrm{A,PO} - 1$
1	5.463 dB	0.6339	0.6380	-0.7%
	10.356 dB	0.7467	0.7475	-0.1%
	15.246 dB	0.7168	0.7149	0.3%
	20.135 dB	0.6454	0.6421	0.5%
2	5.464 dB	0.6324	0.6363	-0.6%
	10.356 dB	0.7409	0.7417	-0.1%
	15.246 dB	0.7080	0.7062	0.3%
	20.135 dB	0.6353	0.6321	0.5%
3	5.460 dB	0.1162	0.2057	-43.5%
	10.354 dB	0.2285	0.3013	-24.1%
	15.247 dB	0.3299	0.3509	-6.0%
	20.139 dB	0.4051	0.3720	8.9%

Table 4.6: Coordinates of $\boldsymbol{r}_\mathrm{ref}$, Strehl ratio, r.m.s. of fitting residuals, and aberration coefficients for $\hat{\boldsymbol{p}} = (1\ \mathrm{deg.}, 0\ \mathrm{deg.})$.

case	$(r_\mathrm{ref}, z_\mathrm{ref})/\mathrm{mm}$	Strehl ratio	r.m.s./λ
1	$(8.789, -497.256)$	0.8615	2.9×10^{-4}
2	$(8.806, -497.095)$	0.8727	2.9×10^{-4}
3	$(8.728, -500.000)$	0.1571	2.9×10^{-4}

case	${A_1}^1/\lambda$	${A_2}^0/\lambda$	${B_2}^2/\lambda$	${A_3}^1/\lambda$	${A_4}^0/\lambda$
1	-0.015143	0.010325	-0.006677	-0.034067	0.047285
2	0	0	-0.006680	-0.034100	0.047346
3	-0.096023	0.185345	-0.006642	-0.033510	0.046258

Table 4.7: Beam waist position, spillover, and beam solid angle for $\hat{\boldsymbol{p}} = (1\ \mathrm{deg.}, 0\ \mathrm{deg.})$.

case	$(r_0, z_0)/\mathrm{mm}$	$\eta_\mathrm{sp,ex}$	$\Omega_\mathrm{A}/\mathrm{sr}$
1	$(8.789, -497.256)$	0.7157	6.6594×10^{-7}
	$(8.789, -497.255)$	0.9078	7.1740×10^{-7}
	$(8.789, -497.253)$	0.9701	7.9846×10^{-7}
	$(8.789, -497.251)$	0.9903	9.0487×10^{-7}
2	$(8.806, -497.095)$	0.7158	6.6724×10^{-7}
	$(8.806, -497.094)$	0.9078	7.2529×10^{-7}
	$(8.806, -497.092)$	0.9701	8.0951×10^{-7}
	$(8.806, -497.090)$	0.9903	9.1926×10^{-7}
3	$(8.728, -500.000)$	0.7155	1.8843×10^{-6}
	$(8.728, -499.999)$	0.9078	1.6534×10^{-6}
	$(8.728, -499.997)$	0.9701	1.5364×10^{-6}
	$(8.727, -499.995)$	0.9903	1.4956×10^{-6}

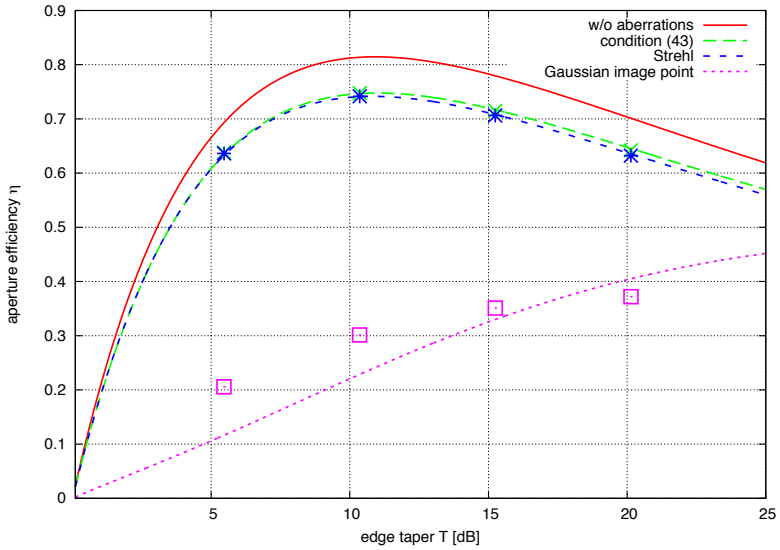

Figure 4.12: Aperture efficiency calculated using Equation (4.75) (lines) and the PO simulation (dots). Red (solid line): no aberrations. Green (long dashed line): Case 1. Blue (dashed line): Case 2. Magenta (dotted line): Case 3.

4.3.6 Discussion

Approximation Precision and Strehl Ratio

The results in Section 4.3.5 indicate that the aperture efficiency estimated using Equation (4.75) agrees with that calculated using PO simulation if the Strehl ratio is high. Consider one of the assumption used in Equation (4.51). The terms up to the second order one, W^2, are used to derive Equation (4.75). Absolute values of the third-order terms are estimated with the standard deviation of wavefront errors, W_{dev}, and summarized in Table 4.10. Table 4.10 seems to describe the precision demonstrated in Table 4.5 and 4.8. The Strehl ratio may indicate the precision of

Table 4.8: Aperture efficiencies obtained using Equations (4.75) and (4.46), and the difference between them for $\hat{\boldsymbol{p}} = (1\ \mathrm{deg.}, 0\ \mathrm{deg.})$.

case	T_{e}	$\eta_{\mathrm{A,an}}$	$\eta_{\mathrm{A,PO}}$	$\eta_{\mathrm{A,an}}/\eta_{\mathrm{A,PO}} - 1$
1	5.463 dB	0.6019	0.6082	-1.0%
	10.354 dB	0.7133	0.7161	-0.4%
	15.243 dB	0.6880	0.6875	0.1%
	20.131 dB	0.6217	0.6193	0.4%
2	5.463 dB	0.6020	0.6070	-0.8%
	10.354 dB	0.7057	0.7083	-0.4%
	15.243 dB	0.6745	0.6781	-0.5%
	20.131 dB	0.6052	0.6096	-0.7%
3	5.459 dB	0.0464	0.2149	-78.4%
	10.353 dB	0.1521	0.3107	-51.1%
	15.244 dB	0.2684	0.3573	-24.9%
	20.135 dB	0.3633	0.3747	3.0%

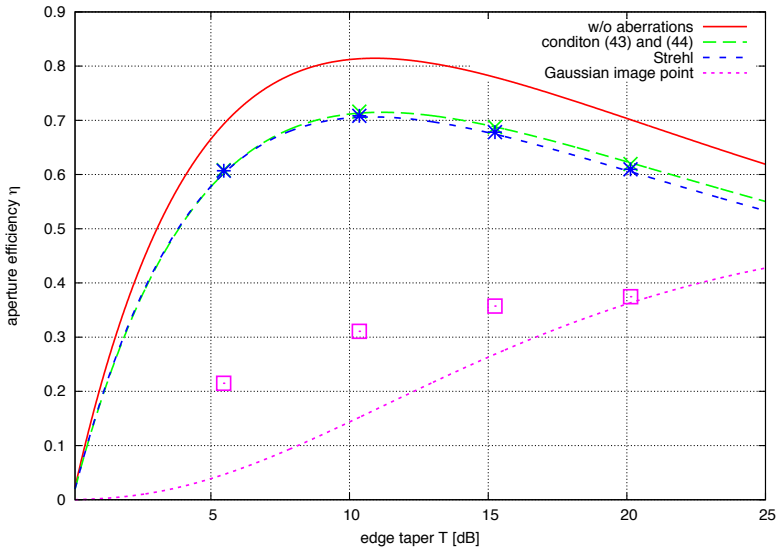

Figure 4.13: Aperture efficiency calculated using Equation (4.75) (curves) and the PO simulation (dots). Red (solid line): no aberrations. Green (long dashed line): Case 1. Blue (dashed line): Case 2. Magenta (dotted line): Case 3.

Table 4.9: Displacement of the peak direction and the maximum.

case	peak displacement	maximum
1	$-0''.50$	71.83 dBi
2	$-8''.39$	71.77 dBi
3	$9''.47$	68.99 dBi

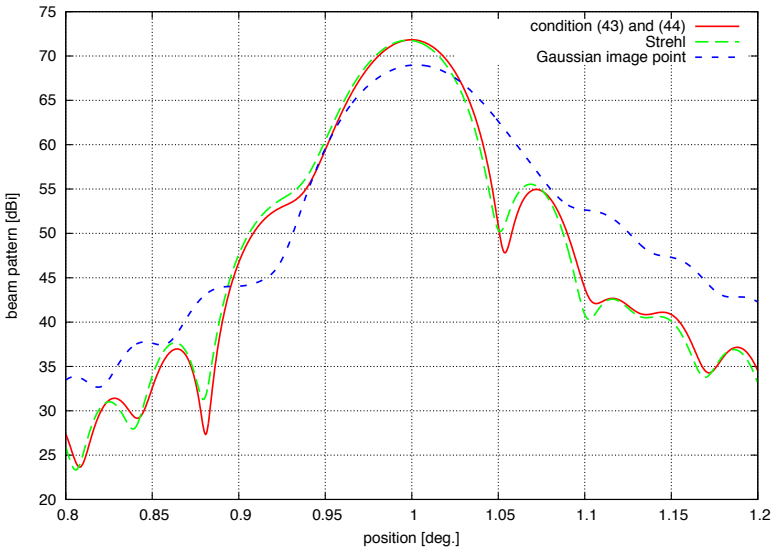

Figure 4.14: Beam patterns away from the field-of-view center (PO simulation). Red (solid line): Case 1. Green (long dashed line): Case 2. Blue (dashed line): Case 3.

Table 4.10: Relative magnitude of the third-order term with respect to the zeroth-order term.

W_{dev}	Strehl ratio	$\lvert -jk^3{W_{\mathrm{dev}}}^3/6\rvert/1$
$\lambda/34.6$	0.968	0.1%
$\lambda/30.2$	0.908	0.5%
$\lambda/16.0$	0.858	1.0%
$\lambda/12.7$	0.784	2.0%
$\lambda/9.4$	0.639	5.0%
$\lambda/7.4$	0.491	10.0%
$\lambda/5.9$	0.323	20.0%
$\lambda/4.7$	0.167	40.0%

Equation (4.75). If the Strehl ratio is 0.8, one will be able to estimate an aperture efficiency with approximately 2% precision.

Applications

The parameters on which an aperture efficiency depends are clarified. One can obtain various information on the system by selecting which parameter is regarded as a free parameter. Equation (4.45) shows that $\hat{\boldsymbol{p}}$ and $\boldsymbol{r}_{\mathrm{ref}}$ are parameters. Equation (4.75) indicates that an aperture efficiency depends on specific features of the system via ${A_n}^m$ and ${B_n}^m$. It is briefly discussed what Equation (4.75) can be applied to and in which cases PO simulation is needed.

When an aperture efficiency is regarded as a function of incident angle $\hat{\boldsymbol{p}}$, and the other parameters are constants,the beam pattern can be obtained as seen in Equation (4.45). Only calculating ${A_n}^m(\hat{\boldsymbol{p}};\boldsymbol{r}_{\mathrm{ref}})$ and ${B_n}^m(\hat{\boldsymbol{p}};\boldsymbol{r}_{\mathrm{ref}})$ by using ray tracing software with respect to various $\hat{\boldsymbol{p}}$ is adequate to obtain the beam pattern.

Next, consider the case when an aperture efficiency is regarded as a function of detector positions $\boldsymbol{r}_0 \propto \boldsymbol{r}_{\mathrm{ref}}$ and the other parameters are constants. The precision of detector alignment can be estimated. As another example, a point spread function (PSF) and a complex field distribution at the focal plane, which are affected by aberrations, can be predicted when ${D_0}^0 = 1$ and ${D_p}^q = 0$ for $p \neq 0$ or $q \neq 0$. A coupling efficiency η_{coup} can be regarded as the linear combination of the expansion coefficients of an incident wave and the Laguerre-Gaussian modes, i.e.,

$$\begin{aligned}\eta_{\mathrm{coup}} &\propto \left|{C_0}^0(\hat{\boldsymbol{p}};\boldsymbol{r}_{\mathrm{ref}})\left({D_0}^0(\boldsymbol{r}_{\mathrm{ref}};\boldsymbol{r}_0;w_0)\right)^*\right|^2 \\ &= \left|\sum_{p'}{C_0}^0(\hat{\boldsymbol{p}};\boldsymbol{r}_{\mathrm{ref}})\left(\tilde{D}_0{}^0(p',0;w_0)\right)^*\left({F_{p'}}^0\right)^*\right|^2, \end{aligned} \tag{4.80}$$

where $\tilde{D}_p{}^q(p',q';w_0)$ appears in Equation (4.62) and ${F_{p'}}^{q'}$ are the expansion coefficients of the sensitivity in Equation (4.57). Equation (4.80) exhibits the field at the exit pupil composed of the Laguerre-Gaussian beams weighted by ${C_0}^0(\hat{\boldsymbol{p}};\boldsymbol{r}_{\mathrm{ref}})\left(\tilde{D}_0{}^0(p',0;w_0)\right)^*$. Then a PSF and a complex

field distribution at the focal plane are obtained as the sum of the Laguerre-Gaussian beams.

Focus on the case when aberration coefficients ${A_n}^m$ and ${B_n}^m$ are regarded as free parameters and $\hat{\boldsymbol{p}}$ as well as $\boldsymbol{r}_{\mathrm{ref}}$ are constants. For example, Equation (4.75) may be used for a tolerance analysis using ray tracing. Generally, a tolerance analysis requires numerous cases of misalignment and deformation. In this analysis, calculations are performed using various methods, e.g., the Monte Carlo method. Equation (4.75) can provide the aperture efficiency or other information on all the cases. Improvement of an error budget quality and robustness is expected.

Finally, the cases when this analytical evaluation can be applied are summarized. In this study, the keys of the evaluation are assumptions that propagation between the entrance and exit pupils can be described using geometrical optics and propagation in front of the entrance pupil as well as behind the exit pupil can be described using the Fresnel diffraction. Therefore, one need PO simulation or other numerical simulation in the following cases:

1. Diffraction effects at the edge of optical elements,

2. A higher order approximation needed than Fresnel diffraction,

3. Evaluation of polarization properties.

4.3.7 Summary of Aperture Efficiency

The parameter dependence of an aperture efficiency is clarified, which exclude the obscurity of the aperture efficiency for beams propagating out of the center of the field of view. It is clearly shown that an aperture efficiency depends on the incident angle and the position of detectors. The relation between an aperture efficiency and a beam pattern is explicitly shown. By expanding wavefront errors and a detector sensitivity by using the Zernike annular polynomials, analytical expression of the aperture efficiency affected by aberrations as functions of an incident angle, a detector position, and aberration coefficients can be acquired. If a Strehl ratio without apodization is greater than 0.8, an aperture efficiency can be estimated with approximately 2% precision by using ray tracing, and not PO simulation.

The conditions to reduce the effects of spherical aberration and coma are also derived. The condition for reducing coma dramatically reduces the pointing error caused by coma. If a non-axial symmetric sensitivity is assumed, a condition to reduce astigmatism may be derived. Various applications to improve a telescope design are expected, for example, the beam pattern, PSF, and tolerance analysis.

4.4 Novel Method to Design Telescope

A novel method to design a wide field-of-view radio telescope is proposed on the basis of the discussion in Sections 4.3 and 4.4. The result in Section 4.3 shows that the performance of a telescope is determined by the beam parameters at the pupil. The result in Section 4.4 indicates that the effect of wave front errors on an aperture efficiency can be reduced. Furthermore, both of the results state that one can use geometrical optics or ray tracing software between the entrance pupil and the exit pupil.

A novel method to design a wide field-of-view radio telescope is composed of a few steps.

1. to determine the distribution of detector sensitivity at the exit pupil,
2. to calculate the coefficients ${D_p}^q$ by using Equation (4.63),
3. to optimize a design to maximize aperture efficiency using ray tracing software.

In the step 1, the distribution of detector sensitivity has to satisfy and is determined by the requirements of, e.g., beam width, side lobe level, and so on. The requirements originate from the science targets of a telescope planned or the convenience of receivers to be used. If the distribution of detector sensitivity is assumed to be a Gaussian distribution, the parameter to be determined is only the beam size w at the exit pupil.

In the step 2, calculate coefficients ${D_p}^q$ for the beam parameters determined in the step 1 by using Equation (4.63). If the sensitivity is assumed to be a Gaussian distribution, one can use the result in Equation (4.64).

In the step 3, use ray tracing software and design a telescope optical system to maximize an aperture efficiency presented in Equation (4.49). If the sensitivity is assumed to be a Gaussian distribution, one can use Equation (4.75) instead of Equation (4.49). An easier way to design can be also considered. Before Equation (4.49) or Equation (4.75) is used, one optimize a telescope optical design to maximize the Strehl ratio and then seek a local maximum of Equation (4.49) in the vicinity of the maximum Strehl ratio.

4.5 Summary

The descriptions or theories of the properties of a radio telescope which are based on a fundamental Gaussian beam is extended to consider the case of a general beam. The frequency-independent condition is simply represented by the lens formula. An aperture efficiency can be described analytically in case of a telescope having aberrations and a detector sensitivity different from an on-axis fundamental Gaussian mode. A novel method to design a wide field-of-view radio tele-

scope is proposed as the application of the frequency-independent condition and the analytical expression of an aperture efficiency.

5

Application to 10-m THz Telescope in Antarctica

5.1 Introduction

A 10-m THz telescope in Antarctica is planned by University of Tsukuba. Tsuzuki et al. (2015) found an optical design with one-degree^2 field of view (Figure 5.1) using ray tracing simulation. As an example of applying the results in Chapter 4, the aperture efficiency of the telescope is shown in this chapter.

5.2 10-m THz telescope in Antarctica

The 10-m THz telescope in Antarctica consists of a Ritchey-Crétien telescope (Wilson 2007), a correcting mirror M1 without optical power, and a re-imaging system (Figure 5.2). The F numbers of the primary mirror and at the Nasmyth focus are 0.55 and 6, respectively. An aperture stop is located at the secondary mirror whose diameter is 1500 mm. The diameter of the entrance pupil is 9454 mm. The mirror M1 is a correcting mirror expressed by polynomials. A field of view at the Nasmyth focal plane is required to be more than 1 degree^2, so that the mirror M1 needs to cancel out astigmatism. The re-imaging optics is composed of four free-form mirrors and an alumina lens and converts the F number of 6 at the Nasmyth focus into an F number of 1 at a detector focus. This optical system is acquired to satisfy that the Strehl ratio is more than 0.8 within a field of view of 1 degree^2 at 850 GHz. Figure 5.3 shows the distribution of the Strehl ratio at the detector focal plane. In most of the region within a 1-degree^2 field of view, the Strehl ratio exceeds 0.9.

5.3 Calculation of Aperture Efficiency

In this section, the aperture efficiency of this system is shown. The case of satisfying Equations (4.76) and (4.77) is also calculated. The frequency is assumed to be 850 GHz, or the wavelength to be 352.9 μm. It is assumed that the detector sensitivity has an axial symmetry. The 6 cases are calculated: the incident angles are ($0.35°$, $0.35°$), ($0.0°$, $0.5°$), ($0.5°$, $0.0°$), ($0.0°$, $0.0°$), ($0.35°$, $-0.35°$), and ($0.0°$, $-0.5°$), corresponding to the number 1 to 6 in Figure 5.3, respectively.

5.3.1 Spillover Efficiency at Entrance Pupil

Since the size of the aperture is 10000 mm and the size of the entrance pupil is 9454 mm, the spillover efficiency of an incident wave is given by Equation (4.34),

$$\eta_{\mathrm{sp,en}} = \frac{(9454 - 750)^2}{(10000 - 750)^2} = 0.8757. \tag{5.1}$$

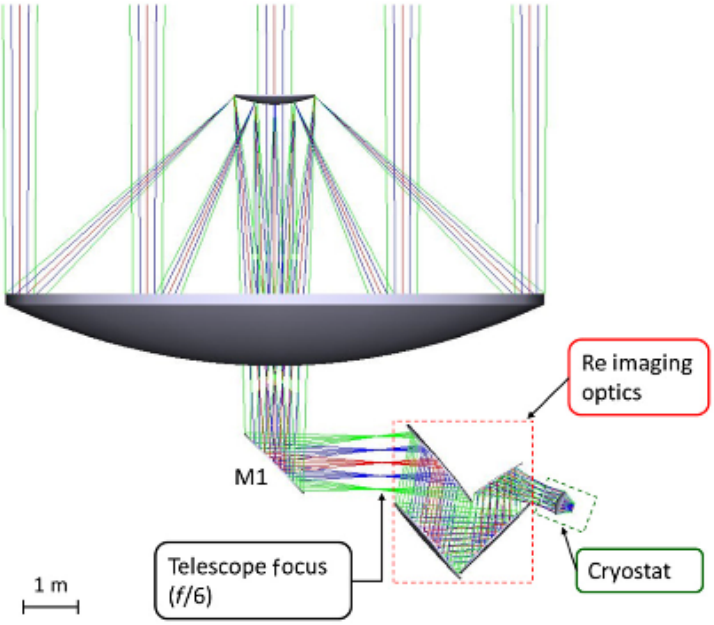

Figure 5.1: Optical design for a 10-m THz telescope in Antarctica planned by University of Tsukuba (Fig. 3 in Tsuzuki et al. (2015)).

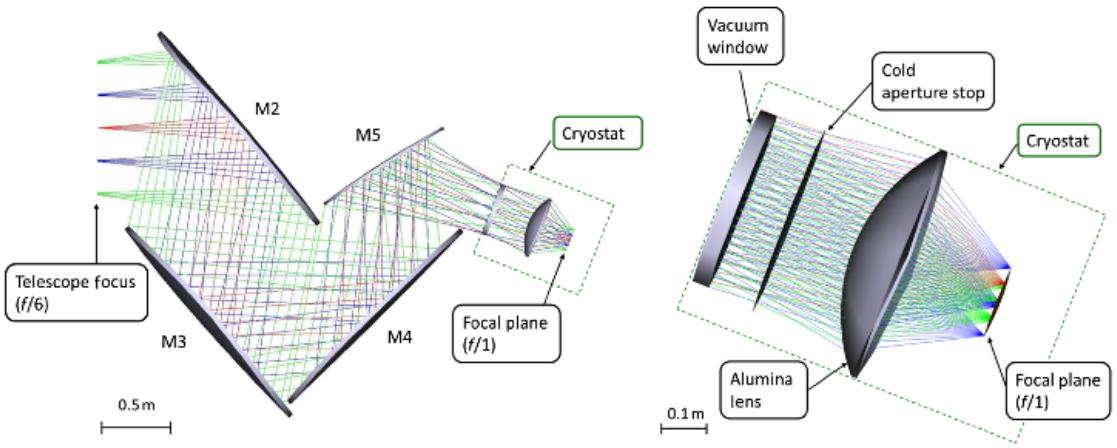

Figure 5.2: Re-imaging system of the 10-m THz telescope in Antarctica (Fig. 4 in Tsuzuki et al. (2015)).

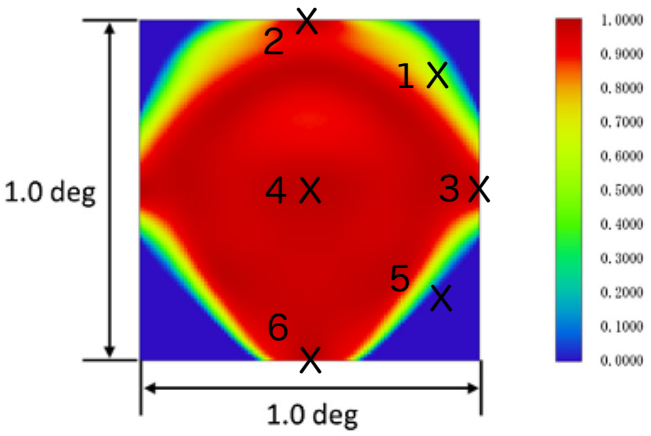

Figure 5.3: The distribution of the Strehl ratio at the focal plane (modified from Fig. 5 in Tsuzuki et al. (2015)).

Note that the radius of the secondary mirror, which blocks part of the aperture, is 750 mm.

5.3.2 Spillover Efficiency at Exit Pupil

It is assumed that the edge taper at the secondary mirror is 15 dB, which corresponds to the beam size of about 198 mm at the cryostat window and about 570 mm at the secondary mirror. One of the pupils is located near at the cryostat window. According to Equation (4.71), the spillover efficiency of the detector sensitivity is given by

$$\eta_{\rm sp,ex} = 10^{-15\varepsilon^2/10} - 10^{-15/10} = 0.8936. \tag{5.2}$$

Note that ε is the ratio of the diameter of the secondary mirror to that of the primary mirror, which is 0.15 and means the blockage of the secondary mirror.

5.3.3 Coupling Efficiency and Aperture Efficiency

Coupling efficiency is given by Equation (4.49),

$$\begin{aligned}\eta_{\rm coup} = \frac{2T(1-\varepsilon^2)}{\eta_{\rm sp,en}\eta_{\rm sp,ex}} \Bigg| & {D_0}^0 + jk\left({A_2}^0{D_2}^0 + {A_4}^0{D_4}^0\right) - \frac{k^2}{2}\Bigg[\left({D_0}^0 + \frac{{D_2}^0}{\sqrt{3}}\right)\left({A_1}^1\right)^2 \\ & + 2\sqrt{2}\left(\frac{{D_2}^0}{\sqrt{3}} + \frac{{D_4}^0}{\sqrt{5}}\right){A_1}^1{A_3}^1 + \left({D_0}^0 + \frac{{D_2}^0}{5\sqrt{3}} + \frac{{D_4}^0}{\sqrt{5}} + \frac{9{D_6}^0}{5\sqrt{7}}\right)\left({A_3}^1\right)^2 \\ & + \left({D_0}^0 + \frac{2{D_4}^0}{\sqrt{5}}\right)\left({A_2}^0\right)^2 + \left(\frac{4{D_2}^0}{\sqrt{5}} + \frac{6\sqrt{15}{D_6}^0}{5\sqrt{7}}\right){A_2}^0{A_4}^0 \\ & + \left({D_0}^0 + \frac{2\sqrt{5}{D_4}^0}{7} + \frac{6{D_8}^0}{7}\right)\left({A_4}^0\right)^2 + \left({D_0}^0 + \frac{\sqrt{3}{D_2}^0}{2} + \frac{{D_4}^0}{2\sqrt{5}}\right)\left({B_2}^2\right)^2\Bigg]\Bigg|^2. \end{aligned} \tag{5.3}$$

Note that T is defined in Equation (4.53). The values of coefficients ${D_p}^0$ for the edge taper of 15 dB are shown in Table 5.1.

In case of optimization with respect to Strehl ratios, aberration coefficients ${A_n}^m$ and ${B_n}^m$ obtained from ray tracing simulation is tabulated (Table 5.2) and the coupling efficiency and the aperture efficiencies estimated from aberration coefficients ${A_n}^m$ and ${B_n}^m$ are shown in Table 5.3. Since the coupiling efficiency for 15 dB taper and no aberrations is 0.815, $\eta_{\rm sp,en} = 0.8757$, and $\eta_{\rm sp,ex} = 0.8936$ in this design, 0.638 is a maximum value expected theoretically. The calculated aperture efficiencies, about 0.6, in Table 5.3 imply that this optical system will have extremely high performance.

Next, the case where detector positions are adjusted to satisfy Equations (4.76) and (4.77) is also investigated. The results are in Tables 5.4 and 5.5 similar to Tables 5.2 and 5.3. The calculated aperture efficiencies are almost a maximum value. To improve this value, the spillover efficiencies have to be smaller or the detector sensitivity has to be changed.

5.4 Summary

The results in Chapter 4 are applied to the design of the 10-m THz telescope in Antarctica planned by University of Tsukuba. The design is obtained by using ray tracing simulation. The aperture efficiencies of this telescope are very high and almost a maximum value, which is 0.638 in this case, can be obtained after detector positions are adjusted such that Equations (4.76) and (4.77) hold.

Table 5.1: Coefficients ${D_p}^0$ for the edge taper 15 dB.

${D_0}^0$	${D_2}^0$	${D_4}^0$	${D_6}^0$	${D_8}^0$
0.4644684488	−0.2162701538	0.0462018983	−0.0065183938	0.00070956

Table 5.2: Aberration coefficients ${A_n}^m$ and ${B_n}^m$ at the focal plane.

coefficients	case 1	case 2	case 3	case 4	case 5	case 6
${A_1}^1/\lambda$	−0.040755	0.000000	0.027099	0.000000	0.056737	0.000000
${B_1}^1/\lambda$	0.012635	0.136158	0.005592	0.005846	0.031999	0.010043
${A_2}^0/\lambda$	−0.026712	0.005301	0.005814	0.002480	0.017920	−0.000478
${A_2}^2/\lambda$	0.033571	0.000589	0.000365	−0.001727	−0.235371	−0.000660
${B_2}^2/\lambda$	−0.023285	0.000000	0.001374	0.000000	−0.185834	0.000000
${A_3}^1/\lambda$	−0.019332	0.000000	0.001773	0.000000	0.005522	0.000000
${B_3}^1/\lambda$	0.012951	0.001552	−0.000951	−0.003301	0.037477	0.001568
${A_4}^0/\lambda$	0.009022	0.004330	0.005501	0.000067	−0.026056	−0.001556

Table 5.3: Aperture efficiency.

	case 1	case 2	case 3	case 4	case 5	case 6
coupling efficiency	0.716	0.810	0.797	0.813	0.034	0.813
aperture efficiency	0.560	0.634	0.623	0.636	0.027	0.636

Table 5.4: Aberration coefficients ${A_n}^m$ and ${B_n}^m$ after adjustment.

coefficients	case 1	case 2	case 3	case 4	case 5	case 6
${A_1}^1/\lambda$	0.008850	0.000000	0.000637	0.000000	−0.001130	0.000000
${B_1}^1/\lambda$	0.003299	0.000561	−0.000447	−0.001469	0.017162	0.000693
${A_2}^0/\lambda$	0.001019	0.000933	0.001174	0.000005	−0.005832	−0.000339
${A_2}^2/\lambda$	0.039785	0.000720	−0.000989	−0.001496	−0.244960	−0.000639
${B_2}^2/\lambda$	0.026139	0.000000	0.000390	0.000000	0.199199	0.000000
${A_3}^1/\lambda$	0.019911	0.000000	0.001433	0.000000	−0.002543	0.000000
${B_3}^1/\lambda$	0.007421	0.001263	−0.001006	−0.003304	0.038610	0.001559
${A_4}^0/\lambda$	0.004666	0.004273	0.005376	0.000022	−0.026711	−0.001551

Table 5.5: Aperture efficiency after adjustment.

	case 1	case 2	case 3	case 4	case 5	case 6
coupling efficiency	0.758	0.814	0.814	0.815	0.053	0.815
aperture efficiency	0.593	0.637	0.637	0.638	0.041	0.638

6

Wavefront Measurements

6.1 Introduction

This section deals with a wavefront sensor, which will be necessary to construct and operate a large sub-millimeter or THz telescope in the future because wavefront sensing is imperative in the manufacture of optical elements and the calibration of optical systems. Padin (2013) reported that the Fried length is 44 m at the third quartile for the CCAT site in observing at 350 μm. It is possible that telescope performance is affected by the atmosphere, i.e., seeing.

Among the various types of wavefront sensors proposed until now (Platt & Shack 2001; Roddier 1988; Vérinaud 2004), one of the most promising is the point-diffraction interferometer (PDI). This type of sensor had been proposed a century earlier by Linnik (Malacara 2007) and is commonly used today because it offers highly accurate measurements even in unstable environments (Malacara 2007). The PDI is categorized as a common-path interferometer, in which unaberrated light (the reference beam) is separated from the incident light with a pinhole at the focal plane and then interferes with the rest of the light (the test beam). Four interferograms with phase differences of $0,\ \pi,\ \pi/2$, and $-\pi/2$ are necessary for the PDI to reconstruct the phase of the wavefront. Since the phase of the reference beam is modulated temporally, the time resolution is poorer than that obtained using geometric shape measurement such as in Shack-Hartmann sensors.

Recently, Millerd et al. (Millerd et al. 2004) successfully measured a phase of wavefront in real time, combining a polarizing point-diffraction plate composed of a wire grid and an instantaneous phase shifter. The direction of the wire grid in the pinhole is orthogonal to that in its surrounding area to make the reference and test beams orthogonally polarized. After transmitting the polarizing point-diffraction plate, a holographic element combines the two beams and then splits the combined beams into four replicas. The four replicas pass through a phase mask composed of wave plates and polarizers just in front of the detector array, and then are transformed into the four interferograms. This configuration enables to realize highly precise measurements even in the presence of vibrations. However, the efficiency of this sensor is one-quarter owing to the polarization.

Effects of the pinhole size have also been investigated because the pinhole induces various errors, e.g., adding aberrations to the reference beam and distorting the test beam. Smartt & Steel (1975) discussed a general theory and a case in which the pinhole acted as the delta function, but they did not show calculations of a specific PDI system example. There are many papers discussing the effects of the pinhole on distorting the reference wavefront in high-numerical-aperture systems, e.g., Naulleau et al. (2000); Lingfeng & Dingguo (2007); Wang et al. (2013); Glückstad & Mogensen (2001); Anderson (1995); Sanchez-de-la Llave & Castillo (2002). Naulleau et al. (2000) assumed that imperfection of a reference beam, which arose from the pinhole, limited measurement accuracy and that systematic geometric effects could be removed if they could be measured.

They showed that the reference wave r.m.s. increased when the pinhole size became larger but did not discuss the geometric effects. These studies entailed mainly use of numerical methods and only rarely were analytical methods employed. Therefore, estimates of specific values such as the wavefront r.m.s. could be obtained but predicting response (e.g., how far the system was from linearity) proved difficult. As an instance of using analytical methods, Glückstad & Mogensen (2001) provided a detailed analysis on the choice of the pinhole size, which should be smaller than 0.627 times the Airy radius, but did not discuss uncertainties accompanying measurements, manufacture, and so on. The performance of common path interferometers was discussed in Anderson (1995); Sanchez-de-la Llave & Castillo (2002) by evaluating the visibility which is not directly connected with wavefront, but deducing phase directly was hardly discussed and therefore it is difficult to estimate effects or uncertainties of parameters.

Based on this background of knowledge, a novel wavefront sensor based on a PDI is proposed and its performance is studied with an analytical formulation. This sensor uses as much energy entering the sensor as possible without throwing away part of the energy. Because the polarizing point-diffraction plate applied by Millerd et al. (2004) reflects a polarized beam parallel to the direction of the wire grid, one can acquire simultaneously the two-polarization states for each of the test and reference beams with a slightly tilting polarizing point-diffraction beam splitter (PPBS), corresponding to the polarizing point-diffraction plate in Millerd et al. (2004).

In this section, the configuration and concept of the novel sensor in Section 6.2. In section 6.3 the analytical formulation with the Fraunhofer diffraction equation is derived, and it is proved that there are two terms: one stemming from the pinhole and the other from the polarizing properties of the PPBS. Using the derived formula, the effects of the pinhole size and the polarizing properties of the PPBS are discussed in Section 6.4, as well as the propagation of uncertainties. Discussion in this section is in accordance with Imada et al. (2015a), which as well as discussion in Yamamoto et al. (2015) can be applied to instruments used in a radio band, cf., Serabyn & Wallace (2010).

6.2 Real-time Wavefront Sensor Configuration

A novel wavefront sensor is shown in Figure 6.1. Collimated light with small aberrations passes through the entrance pupil and Lens1. It reaches the PPBS slightly tilted at the focal plane of Lens1 so that the beams transmitted through and reflected by the PPBS can be used to make four interferograms at the same time. It is assumed that effects of tilting, e.g., astigmatism, can be negligible and that results of the tilted PPBS correspond to those of a PPBS perpendicular to the z axis, though these assumptions should be verified with numerical simulations. The PPBS, which consists of a wire gird for example, has polarizing properties. The PPBS has a polarizing pinhole

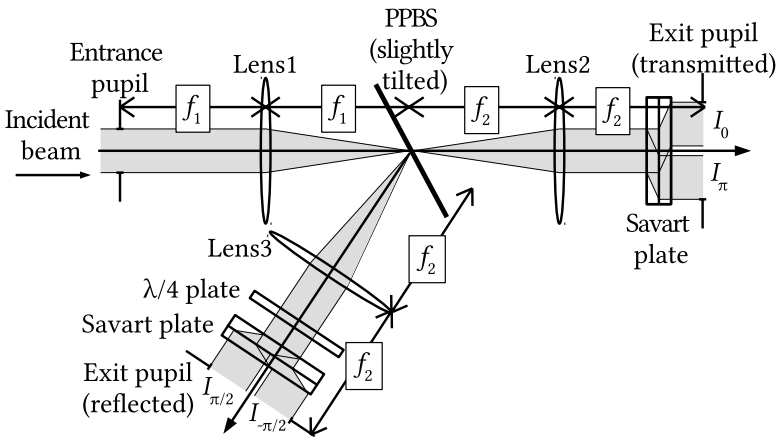

Figure 6.1: Schematic configuration of the novel sensor. Lens 1 has a focal length of f_1. The PPBS is set at the focal plane of Lens 1 and slightly tilted. The reflected and transmitted beams are collimated by Lens 2 or Lens 3, whose focal lengths are each f_2. Interferograms named I_0 and I_π are made at the exit pupil on the transmitted path. Other interferograms named $I_{\pi/2}$ and $I_{-\pi/2}$ are made at the exit pupil on the reflected path. Details of the polarization and Savart plates are shown in Figure 6.2 and 6.3.

of which diameter $2R_{\mathrm{pin}}$ (Figure 6.2) is smaller than or equivalent to the Airy disk. The region excluding the pinhole also has a polarizing property but is orthogonal to that of the pinhole. The pinhole allows one polarization to pass though and the region excluding the pinhole does the other polarization. The beam passing through the pinhole (either transmitted through it or reflected by it) behave as a reference beam without aberrations. The beam passing through the outer region of the PPBS, called the test beam, carries information of the incident aberrations to the detectors. By setting two Savart plates (Malacara 2007) so that their optical axes are inclined at 45° and -45° (Figure 6.3), two interferograms can be obtained: one of the reference beam and test beam with the same phase and the other with a phase difference of π rad. By setting a quarter-wave plate in ether the transmitted or the reflected path, another pair of interferograms can be obtained, the reference beam of which has a $\pm\pi/2$-rad delay compared to the test beam. The Savart plates and quarter-wave plate can be set at an arbitrary position on the path after the PPBS because the beams are collimated. The key points of the system proposed in this paper are that both the transmitted and reflected beams can be used, that both the reference and test beams propagate on a common path, and that four interferograms can be obtained simultaneously.

The variables used in the formulation in Section 6.3 are defined as follows: (x_1, y_1), (x_2, y_2), and $(x_{\mathrm{PPBS}}, y_{\mathrm{PPBS}})$ denote coordinates at pupil 1 (entrance pupil, P1), pupil 2 (exit pupil, P2, detector), and the PPBS, respectively. It is assumed that all optical elements to be rotationally symmetric. The radii of P1, P2, the PPBS, and the pinhole are referred to as R_1, R_2, R_{PPBS}, and R_{pin}, respectively. The distances between P1 and the PPBS and between the PPBS and P2 are f_1 and f_2, respectively. The F numbers are defined as $F_1 = f_1/(2R_1)$ and $F_2 = f_2/(2R_2)$, respectively.

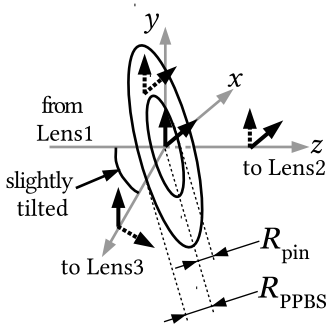

Figure 6.2: The PPBS and polarizations of the transmitted and reflected beams. The PPBS whose radius is R_{PPBS} has a pinhole with a radius of R_{pin}. The bold solid arrows represent polarizations of the beams passing through the pinhole and the bold dashed arrows represent those through the region other than the pinhole.

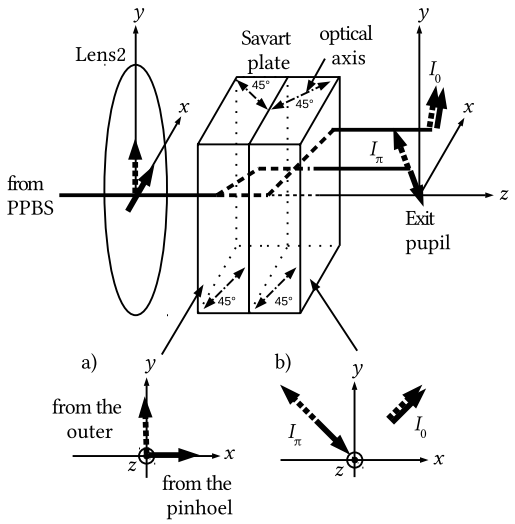

Figure 6.3: Polarizations and Savart plate on the transmitted path after the PPBS. The bold solid arrows represent a reference beam polarization and the bold dashed arrows represent a test beam polarization. The double-headed arrows represent optical axes of the Savart plate projected on the yz or zx plane. In case of the reflected path, add the quarter-wave plate to this figure. a) Incident field on the first Savart plate surface. b) Transmitted field through the second Savart plate.

The analysis and discussion in the following section focus on the pinhole size R_{pin}. The pinhole size R_{pin} act as an important parameter determining the performance of PDIs as shown in the literature Naulleau et al. (2000); Lingfeng & Dingguo (2007); Wang et al. (2013); Glückstad & Mogensen (2001); Anderson (1995); Sanchez-de-la Llave & Castillo (2002), which will be made clear again in the following discussion. The radius of PPBS R_{PPBS} can be arbitrary selected and therefore, if there are small aberrations, it can be $NF_1\lambda$ $(N \in \mathbb{N})$ so that spatial resolution on the entrance pupil should be $2R_1/N$.

6.3 Formulation

To investigate the novel system using an analytic method, consider beam propagation with diffraction integrals but only have to conduct the Fraunhofer integral. In case of the system shown in Figure 6.1, the field on the entrance pupil and the PPBS can be connected with a Fourier transform because they are put at the front and back focal planes, respectively. The exit pupil and the PPBS can be connected this way as well.

6.3.1 Fraunhofer Propagation to the Detector Plane

The electric field at pupil 1 is assumed to be given by the following equation with wavefront error $\delta(x_1, y_1; t)$ and amplitude error $\alpha(x_1, y_1; t)$:

$$\boldsymbol{E}_1(x_1, y_1; t) = \begin{pmatrix} E_{1,x}(x_1, y_1; t) \\ E_{1,y}(x_1, y_1; t) \end{pmatrix} = \begin{pmatrix} E_x \left[1 + \alpha(x_1, y_1; t)\right] \exp\left[\sqrt{-1}\delta(x_1, y_1; t)\right] \\ E_y \left[1 + \alpha(x_1, y_1; t)\right] \exp\left[\sqrt{-1}\delta(x_1, y_1; t)\right] \end{pmatrix}, \tag{6.1}$$

where $\delta(0, 0; t) = 0$ always holds. The time t is hereafter shown as needed. By using $\boldsymbol{E}_1$ and the Fraunhofer diffraction equation, which holds when R_1 and $R_{\mathrm{PPBS}} \ll f_1$, the electric field at the PPBS can be expressed as

$$\boldsymbol{E}_{\mathrm{PPBS}}(x_{\mathrm{PPBS}}, y_{\mathrm{PPBS}}) = \frac{\sqrt{-1}}{\lambda f_1} \iint_{\mathrm{P1}} \boldsymbol{E}_1(x_1, y_1) \exp\left[\sqrt{-1}\frac{k\left(x_1 x_{\mathrm{PPBS}} + y_1 y_{\mathrm{PPBS}}\right)}{f_1}\right] \mathrm{d}x_1 \mathrm{d}y_1, \tag{6.2}$$

where λ is the wavelength of the input beam and k is the wavenumber ($= 2\pi/\lambda$). The integral is evaluated at pupil 1. Because the PPBS and the pinhole are set to be circular, the electric fields can be written after passing through the PPBS using a polar coordinate system (where $r_{\mathrm{PPBS}} := \sqrt{{x_{\mathrm{PPBS}}}^2 + {y_{\mathrm{PPBS}}}^2}$)

$$\begin{aligned} {\boldsymbol{E}_{\mathrm{PPBS}}}^{\mathrm{T}}(x_{\mathrm{PPBS}}, y_{\mathrm{PPBS}}) &= T(r_{\mathrm{PPBS}}) \boldsymbol{E}_{\mathrm{PPBS}}(x_{\mathrm{PPBS}}, y_{\mathrm{PPBS}}), \\ {\boldsymbol{E}_{\mathrm{PPBS}}}^{\mathrm{R}}(x_{\mathrm{PPBS}}, y_{\mathrm{PPBS}}) &= R(r_{\mathrm{PPBS}}) \boldsymbol{E}_{\mathrm{PPBS}}(x_{\mathrm{PPBS}}, y_{\mathrm{PPBS}}). \end{aligned} \tag{6.3}$$

where the superscripts T and R represent transmitted and reflected beams, respectively. T and R are matrices that represent the PPBS polarizing properties. They can be written as

$$T(r_{\mathrm{PPBS}}) = \begin{cases} \begin{pmatrix} T_x & 0 \\ 0 & T_y \end{pmatrix} & (r_{\mathrm{PPBS}} \leq R_{\mathrm{pin}}) \\ \begin{pmatrix} T_y & 0 \\ 0 & T_x \end{pmatrix} & (R_{\mathrm{pin}} < r_{\mathrm{PPBS}} \leq R_{\mathrm{PPBS}}) \\ \text{null matrix} & (R_{\mathrm{PPBS}} < r_{\mathrm{PPBS}}) \end{cases} \tag{6.4}$$

$$R(r_{\mathrm{PPBS}}) = \begin{cases} \begin{pmatrix} R_x & 0 \\ 0 & R_y \end{pmatrix} & (r_{\mathrm{PPBS}} \leq R_{\mathrm{pin}}) \\ \begin{pmatrix} R_y & 0 \\ 0 & R_x \end{pmatrix} & (R_{\mathrm{pin}} < r_{\mathrm{PPBS}} \leq R_{\mathrm{PPBS}}) \\ \text{null matrix} & (R_{\mathrm{PPBS}} < r_{\mathrm{PPBS}}) \end{cases} \tag{6.5}$$

Note that the polarizing properties depend on the incident angle of a beam. However, it is assumed that they are independent of the incident angle if the F number F_1 is large enough. The transmitted field along x axis is

$${E_{\mathrm{PPBS},x}}^{\mathrm{T}} = \begin{cases} T_x E_{\mathrm{PPBS},x} & (r_{\mathrm{PPBS}} \leq R_{\mathrm{pin}}) \\ T_y E_{\mathrm{PPBS},x} & (R_{\mathrm{pin}} < r_{\mathrm{PPBS}} \leq R_{\mathrm{PPBS}}) \\ \text{null} & (R_{\mathrm{PPBS}} < r_{\mathrm{PPBS}}) \end{cases} . \tag{6.6}$$

The other fields can also be written like Equation (6.6). The calculations of ${E_{\mathrm{PPBS},x}}^{\mathrm{T}}$ are shown as an example.

By using the Fraunhofer diffraction equation again and substituting Equation (6.6), the electric field at pupil 2 can be expressed as

$$\begin{aligned} {E_{2,x}}^{\mathrm{T}}(x_2, y_2) = & \frac{\sqrt{-1}}{\lambda f_2} \iint_{\mathrm{P_{PPBS}}} {E_{\mathrm{PPBS},x}}^{\mathrm{T}}(x_{\mathrm{PPBS}}, y_{\mathrm{PPBS}}) \\ & \times \exp\left[\sqrt{-1}\frac{k\left(x_{\mathrm{PPBS}}x_2 + y_{\mathrm{PPBS}}y_2\right)}{f_2}\right] \mathrm{d}x_{\mathrm{PPBS}}\mathrm{d}y_{\mathrm{PPBS}} \\ = & \frac{-T_x}{\lambda^2 f_1 f_2} \iint_{\mathrm{P_{pin}}} \mathrm{d}x_{\mathrm{PPBS}}\mathrm{d}y_{\mathrm{PPBS}} \iint_{\mathrm{P1}} \mathrm{d}x_1\mathrm{d}y_1 E_{1,x}(x_1, y_1) \\ & \times \exp\left[\sqrt{-1}k\left(\frac{x_1}{f_1} + \frac{x_2}{f_2}\right)x_{\mathrm{PPBS}} + \sqrt{-1}k\left(\frac{y_1}{f_1} + \frac{y_2}{f_2}\right)y_{\mathrm{PPBS}}\right] \\ & + \frac{-T_y}{\lambda^2 f_1 f_2} \iint_{\mathrm{P_{PPBS}} \setminus \mathrm{P_{pin}}} \mathrm{d}x_{\mathrm{PPBS}}\mathrm{d}y_{\mathrm{PPBS}} \iint_{\mathrm{P1}} \mathrm{d}x_1\mathrm{d}y_1 E_{1,x}(x_1, y_1) \\ & \times \exp\left[\sqrt{-1}k\left(\frac{x_1}{f_1} + \frac{x_2}{f_2}\right)x_{\mathrm{PPBS}} + \sqrt{-1}k\left(\frac{y_1}{f_1} + \frac{y_2}{f_2}\right)y_{\mathrm{PPBS}}\right], \end{aligned} \tag{6.7}$$

where the $\mathrm{P_{PPBS}}$ represents a circle with a radius of R_{PPBS}, the $\mathrm{P_{pin}}$ represents a circle with a radius of R_{pin}, and $\mathrm{P_{PPBS}} \setminus \mathrm{P_{pin}}$ means an annular region of the PPBS excluding the pinhole. The next relation holds about interval of the integration:

$$\iint_{\mathrm{P_{PPBS}} \setminus \mathrm{P_{pin}}} \mathrm{d}x_{\mathrm{PPBS}}\mathrm{d}y_{\mathrm{PPBS}} = \iint_{\mathrm{P_{PPBS}}} \mathrm{d}x_{\mathrm{PPBS}}\mathrm{d}y_{\mathrm{PPBS}} - \iint_{\mathrm{P_{pin}}} \mathrm{d}x_{\mathrm{PPBS}}\mathrm{d}y_{\mathrm{PPBS}}. \tag{6.8}$$

Rearranging Equation (6.7) by using Equation (6.8),

$$\begin{aligned} {E_{2,x}}^{\mathrm{T}}(x_2, y_2) &= T_x A_x + T_y \left(B_x - A_x\right) \\ &= \left(T_x - T_y\right) A_x + T_y B_x, \end{aligned} \tag{6.9}$$

where

$$\begin{aligned} A_x := \frac{-1}{\lambda^2 f_1 f_2} \iint_{\mathrm{P_{pin}}} \mathrm{d}x_{\mathrm{PPBS}} \mathrm{d}y_{\mathrm{PPBS}} \iint_{\mathrm{P1}} \mathrm{d}x_1 \mathrm{d}y_1 E_{1,x}(x_1, y_1) \\ \times \exp\left[\sqrt{-1}k\left(\frac{x_1}{f_1} + \frac{x_2}{f_2}\right) x_{\mathrm{PPBS}} + \sqrt{-1}k\left(\frac{y_1}{f_1} + \frac{y_2}{f_2}\right) y_{\mathrm{PPBS}}\right], \end{aligned} \tag{6.10}$$

$$\begin{aligned} B_x := \frac{-1}{\lambda^2 f_1 f_2} \iint_{\mathrm{P_{PPBS}}} \mathrm{d}x_{\mathrm{PPBS}} \mathrm{d}y_{\mathrm{PPBS}} \iint_{\mathrm{P1}} \mathrm{d}x_1 \mathrm{d}y_1 E_{1,x}(x_1, y_1) \\ \times \exp\left[\sqrt{-1}k\left(\frac{x_1}{f_1} + \frac{x_2}{f_2}\right) x_{\mathrm{PPBS}} + \sqrt{-1}k\left(\frac{y_1}{f_1} + \frac{y_2}{f_2}\right) y_{\mathrm{PPBS}}\right]. \end{aligned} \tag{6.11}$$

A_x is integrated on the pinhole ($0 \leq r_{\mathrm{PPBS}} \leq R_{\mathrm{pin}}$) and B_x is integrated on the whole PPBS including the pinhole ($0 \leq r_{\mathrm{PPBS}} \leq R_{\mathrm{PPBS}}$). A_x, which is determined by the pinhole geometry, contributes to the interferograms but has not been investigated.

6.3.2 Evaluation of the Integrals A_x and B_x

Before calculating Equations (6.10) and (6.11), variables are changed from the Cartesian coordinate system to the polar one:

$$\begin{aligned} r_{\mathrm{PPBS}} \cos\theta_{\mathrm{PPBS}} := x_{\mathrm{PPBS}}, \quad r_{\mathrm{PPBS}} \sin\theta_{\mathrm{PPBS}} := y_{\mathrm{PPBS}}, \\ \rho\cos\theta := \frac{x_1}{f_1} + \frac{x_2}{f_2}, \qquad \rho\sin\theta := \frac{y_1}{f_1} + \frac{y_2}{f_2}. \end{aligned} \tag{6.12}$$

Integrating over r_{PPBS} and θ_{PPBS}, then

$$A_x = \frac{-f_1}{2\pi f_2} \int_0^{2\pi} \mathrm{d}\theta \int_0^{\ell(\theta)} k^2 {R_{\mathrm{pin}}}^2 \rho \mathrm{d}\rho E_{1,x}(\rho, \theta) \frac{J_1(kR_{\mathrm{pin}}\rho)}{kR_{\mathrm{pin}}\rho}, \tag{6.13}$$

$$B_x = \frac{-f_1}{2\pi f_2} \int_0^{2\pi} \mathrm{d}\theta \int_0^{\ell(\theta)} k^2 {R_{\mathrm{PPBS}}}^2 \rho \mathrm{d}\rho E_{1,x}(\rho, \theta) \frac{J_1(kR_{\mathrm{PPBS}}\rho)}{kR_{\mathrm{PPBS}}\rho}, \tag{6.14}$$

where J_1 is the first-order Bessel function of the first kind and the parameter $\ell(\theta)$ is

$$\ell(\theta) := \rho_2 \cos\theta + \sqrt{\left(\frac{R_1}{f_1}\right)^2 - {\rho_2}^2 \sin^2\theta}, \tag{6.15}$$

where $\rho_2 := \sqrt{(x_2/f_2)^2 + (y_2/f_2)^2}$. ρ_2 represents the distance from the center of pupil 2.

First, the integral A_x is calculated. It is assumed that (1) the pinhole size R_{pin} is less than or

equivalent to the Airy disk size; (2) $|\alpha(\rho,\theta)| \ll 1$ whose periods are shorter than the entrance pupil diameter $2R_1$; and (3) $\exp[\sqrt{-1}k\delta(\rho,\theta)]$ also has shorter periods than the entrance pupil diameter $2R_1$. The assumption (1) means that the first null point of the Bessel function $J_1(kR_{\rm pin}\rho)$, i.e., $1.22\pi/(kR_{\rm pin})$, is much larger than $2R_1$, noting that ρ is the function of the coordinate on the entrance pupil and therefore the integral A_x does not easily depend on the coordinate of the pupil. The assumption (2) and (3) mean that differences of $[1+\alpha(\rho,\theta)]\exp[\sqrt{-1}k\delta(\rho,\theta)]J_1(kR_{\rm pin}\rho)/(kR_{\rm pin}\rho)$ from the function $J_1(kR_{\rm pin}\rho)/(kR_{\rm pin}\rho)$ can be canceled when integrated, that is

$$\iint_{\rm P1}[1+\alpha(\rho,\theta)]\exp[\sqrt{-1}k\delta(\rho,\theta)]\frac{J_1(kR_{\rm pin}\rho)}{kR_{\rm pin}\rho}k^2{R_{\rm pin}}^2\rho{\rm d}\rho \approx \iint_{\rm P1}\frac{J_1(kR_{\rm pin}\rho)}{kR_{\rm pin}\rho}k^2{R_{\rm pin}}^2\rho{\rm d}\rho, \quad (6.16)$$

noting that the input field is given by Equation (6.1). Thus, it can be assumed that $E_{1,x}(\rho,\theta)$ in the integral should be regraded as a constant E_x. Using the relation ${\rm d}J_0(x)/{\rm d}x = -J_1(x)$ (Watson 1966), the following result is acquired:

$$A_x = \frac{f_1}{f_2}E_x\frac{1}{2\pi}\int_0^{2\pi}{\rm d}\theta\left[J_0\left(kR_{\rm pin}\ell(\theta)\right)-1\right] = -\frac{f_1}{f_2}E_x f(R_{\rm pin};r_2), \quad (6.17)$$

where $r_2 := \sqrt{{x_2}^2+{y_2}^2}(=f_2\rho_2)$. When r_2 is 0, i.e., at the center of pupil 2,

$$f(R_{\rm pin};0) = 1 - J_0\left(\pi\frac{R_{\rm pin}}{F_1\lambda}\right), \quad (6.18)$$

otherwise, Equation (6.17) needs to be integrated numerically at $R_{\rm pin}/(F_1\lambda) = n/8\,(n=0,1,\cdots,10)$ and the numerical results with polynomials of $R_{\rm pin}/F_1\lambda$ are approximated as

$$f(R_{\rm pin};r_2) = a(r_2)\left(\frac{R_{\rm pin}}{F_1\lambda}\right)^2 + b(r_2)\left(\frac{R_{\rm pin}}{F_1\lambda}\right)^4 + c(r_2)\left(\frac{R_{\rm pin}}{F_1\lambda}\right)^5 + d(r_2)\left(\frac{R_{\rm pin}}{F_1\lambda}\right)^6. \quad (6.19)$$

The reasons to adopt Equation (6.19) are that $f(R_{\rm pin};r_2=0)$ can be written with the zeroth order Bessel function of the first kind consisting of even-ordered polynomials, and that adding the term $(R_{\rm pin}/F_1\lambda)^5$ can make residuals smaller. The coefficients in Equation (6.19) and fitting residuals are tabulated in Table 6.1. The function $f(R_{\rm pin};r_2)$ is shown in Figure 6.4. The residuals are sufficiently small to discuss effects of the pinhole in measuring wavefront in Section 6.4.

Table 6.1: Coefficients of the polynomials in Equation (6.19).

r_2	$a(r_2)$	$b(r_2)$	$c(r_2)$	$d(r_2)$	rms of residuals
$0.2R_2$	2.58	-2.12	0.80	0.01	4.9×10^{-4}
$0.4R_2$	2.91	-3.33	1.82	-0.20	9.5×10^{-4}
$0.6R_2$	3.45	-5.70	4.10	-0.79	1.8×10^{-3}
$0.8R_2$	4.21	-9.63	8.40	-2.07	2.8×10^{-3}
R_2	5.18	-15.45	15.45	-4.40	3.1×10^{-3}

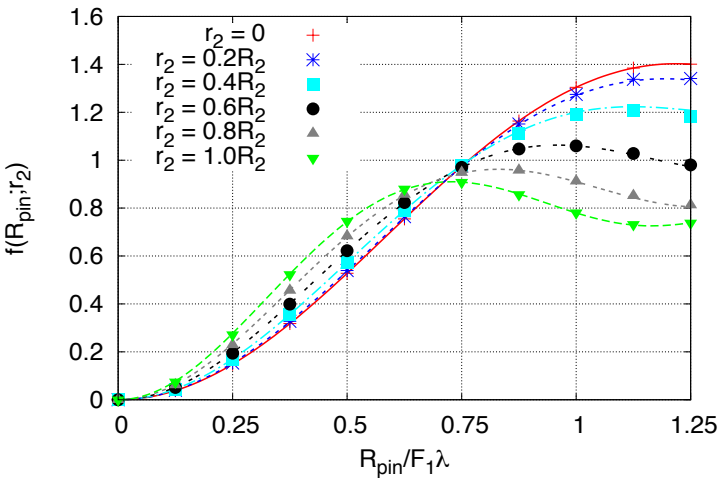

Figure 6.4: The function $f(R_{\rm pin}; r_2)$ in Equation (6.19). The points expressed by the symbols (e.g., the cross) are obtained by integrating numerically.

Next, evaluate the integral B_x. $J_1(kR_{\rm PPBS}\rho)/(kR_{\rm PPBS}\rho)$ takes approximate unity when $\rho(x_1, y_1) \approx 0$ and converges to zero with oscillation ($\rho \to \infty$), and therefore only the field $E_1(\rho(x_1, y_1) \approx 0)$, i.e., $E_{1,x}(-(f_1/f_2)x_2, -(f_1/f_2)y_2)$ will contribute to the integral B_x, which means one can take $E_{1,x}(-(f_1/f_2)x_2, -(f_1/f_2)y_2)$ out of the integral as a constant.

If $R_{\rm PPBS} \sim 50F_1\lambda$, which means that pupil 1 can be spatially resolved into $\sim 50^2$ areas, then $kR_{\rm PPBS}$ ($\sim 10^4$ at $F_1 \sim 30$) is so large that the interval can be extended from $[0 : \ell(\theta)]$ to $[0 : \infty]$. Thus,

$$\begin{aligned} B_x &\simeq -\frac{f_1}{2\pi f_2} E_{1,x}\left(-\frac{f_1}{f_2}x_2, -\frac{f_1}{f_2}y_2\right) \int_0^{2\pi} \mathrm{d}\theta \int_0^{\infty} k^2 {R_{\rm PPBS}}^2 \rho \mathrm{d}\rho \frac{J_1(kR_{\rm PPBS}\rho)}{kR_{\rm pin}\rho} \\ &= \frac{f_1}{f_2} E_{1,x}\left(-\frac{f_1}{f_2}x_2, -\frac{f_1}{f_2}y_2\right) J_0(kR_{\rm PPBS}\rho)|_0^{\infty} = -\frac{f_1}{f_2} E_{1,x}\left(-\frac{f_1}{f_2}x_2, -\frac{f_1}{f_2}y_2\right). \end{aligned} \tag{6.20}$$

The electric fields other than ${E_{\rm PPBS,}x}^{\rm T}$ are also calculated in the same manner. The results are compiled in the following equations

$$\begin{aligned} A_x(x_2, y_2) &= -\frac{f_1}{f_2} E_x f(R_{\rm pin}; r_2), \\ A_y(x_2, y_2) &= -\frac{f_1}{f_2} E_y f(R_{\rm pin}; r_2), \\ B_x(x_2, y_2; t) &= -\frac{f_1}{f_2} E_{1,x}\left(-\frac{f_1}{f_2}x_2, -\frac{f_1}{f_2}y_2; t\right), \\ B_y(x_2, y_2; t) &= -\frac{f_1}{f_2} E_{1,y}\left(-\frac{f_1}{f_2}x_2, -\frac{f_1}{f_2}y_2; t\right), \end{aligned} \tag{6.21}$$

and

$$
\begin{aligned}
{E_{2,x}}^{\mathrm{T}}(x_2, y_2; t) &= (T_x - T_y)\, A_x + T_y B_x, \\
{E_{2,y}}^{\mathrm{T}}(x_2, y_2; t) &= (T_y - T_x)\, A_y + T_x B_y, \\
{E_{2,x}}^{\mathrm{R}}(x_2, y_2; t) &= (R_x - R_y)\, A_x + R_y B_x, \\
{E_{2,y}}^{\mathrm{R}}(x_2, y_2; t) &= (R_y - R_x)\, A_y + R_x B_y.
\end{aligned}
\tag{6.22}
$$

A_x and A_y indicate there is a contribution from the pinhole that would be non-zero. Equation (6.22) corresponds to equation (3) in Smartt & Steel (1975). Note that a small pinhole, small aberrations, and large F number are assumed.

6.3.3 Interferograms and Phase Derivation

In general, one can observe averages of the square of the electric field over time in the visible light and infrared regions. The average over time is defined as

$$
\langle F(t) \rangle := \frac{1}{T_0} \int_0^{T_0} F(t) \mathrm{d}t. \tag{6.23}
$$

It is assumed that the electric fields are statistically stationary and that T_0 is large enough for $\langle F(t) \rangle$ to converge to a certain value asymptotically.

Four interferograms can be calculated by using

$$
\begin{aligned}
I_0(x_2, y_2; t) &:= \left\langle \left| \tfrac{1}{\sqrt{2}} \left({E_{2,x}}^{\mathrm{T}} + {E_{2,y}}^{\mathrm{T}} \right) \right|^2 \right\rangle, \\
I_\pi(x_2, y_2; t) &:= \left\langle \left| \tfrac{1}{\sqrt{2}} \left({E_{2,x}}^{\mathrm{T}} - {E_{2,y}}^{\mathrm{T}} \right) \right|^2 \right\rangle, \\
I_{\pi/2}(x_2, y_2; t) &:= \left\langle \left| \tfrac{1}{\sqrt{2}} \left({E_{2,x}}^{\mathrm{R}} + \sqrt{-1} {E_{2,y}}^{\mathrm{R}} \right) \right|^2 \right\rangle, \\
I_{-\pi/2}(x_2, y_2; t) &:= \left\langle \left| \tfrac{1}{\sqrt{2}} \left({E_{2,x}}^{\mathrm{R}} - \sqrt{-1} {E_{2,y}}^{\mathrm{R}} \right) \right|^2 \right\rangle.
\end{aligned}
\tag{6.24}
$$

Note that the time t on the left-hand side of Equation (6.24) represents fluctuations longer than T_0.

A parameter $M(x_2, y_2; t)$ and reconstructed phase $\delta_{\mathrm{rec}}(-(f_1/f_2)x_2, -(f_1/f_2)y_2; t)$ are defined as

$$
M := \frac{I_{\pi/2}(x_2, y_2; t) - I_{-\pi/2}(x_2, y_2; t)}{I_0(x_2, y_2; t) - I_\pi(x_2, y_2; t)}, \tag{6.25}
$$

$$
\delta_{\mathrm{rec}} := \tan^{-1} M(x_2, y_2; t), \tag{6.26}
$$

respectively. M is a value determined by measurements. δ_{rec} is commonly used so far to estimate phase. On the other hand, the interferograms can be calculated and one can predict what kind of

functions of the true δ describes M. It is assumed that $\delta(x_1, y_1; t)$ and $\alpha(x_1, y_1; t)$ keep constant values in T_0. By using Equation (6.21), (6.22), and (6.24),

$$\frac{{f_2}^2}{{f_1}^2}\frac{I_{\pi/2} - I_{-\pi/2}}{E_x E_y} = 2\left(|R_x|^2 - |R_y|^2\right) f\,(1+\alpha)\sin\delta + 2\sqrt{-1}\,(R_x {R_y}^* - {R_x}^* R_y)\, f\,(1+\alpha)\cos\delta - \sqrt{-1}\,(R_x {R_y}^* - {R_x}^* R_y)\,(1+\alpha)^2 \tag{6.27}$$

and

$$\frac{{f_2}^2}{{f_1}^2}\frac{I_0 - I_\pi}{E_x E_y} = 2\,|T_x - T_y|^2 f\,(1+\alpha)\cos\delta - 2\,|T_x - T_y|^2 f^2 + (T_x {T_y}^* + {T_x}^* T_y)\,(1+\alpha)^2, \tag{6.28}$$

where $\alpha = \alpha(-(f_1/f_2)x_2, -(f_1/f_2)y_2; t)$, $f = f(R_{\mathrm{pin}}; r_2)$ and $\delta = \delta(-(f_1/f_2)x_2, -(f_1/f_2)y_2; t)$. The polarizing properties of the PPBS can be generally written as

$$\begin{aligned} T_x &= |T_x| \exp\left(\sqrt{-1}{\phi_x}^{\mathrm{T}}\right), \quad T_y = |T_y| \exp\left(\sqrt{-1}{\phi_y}^{\mathrm{T}}\right), \\ R_x &= |R_x| \exp\left(\sqrt{-1}{\phi_x}^{\mathrm{R}}\right), \quad R_y = |R_y| \exp\left(\sqrt{-1}{\phi_y}^{\mathrm{R}}\right). \end{aligned} \tag{6.29}$$

Substituting Equation (6.29) into (6.27) and (6.28),

$$\frac{{f_2}^2}{{f_1}^2}\frac{I_{\pi/2} - I_{-\pi/2}}{E_x E_y} = 2\left(|R_x|^2 - |R_y|^2\right) f\,(1+\alpha)\sin\delta - 4\,|R_x|\,|R_y| \sin\left({\phi_x}^{\mathrm{R}} - {\phi_y}^{\mathrm{R}}\right) f\,(1+\alpha)\cos\delta + 2\,|R_x|\,|R_y| \sin\left({\phi_x}^{\mathrm{R}} - {\phi_y}^{\mathrm{R}}\right)(1+\alpha)^2, \tag{6.30}$$

$$\frac{{f_2}^2}{{f_1}^2}\frac{I_0 - I_\pi}{E_x E_y} = 2\,|T_x - T_y|^2 f\,(1+\alpha)\cos\delta - 2\,|T_x - T_y|^2 f^2 + 2\,|T_x|\,|T_y| \cos\left({\phi_x}^{\mathrm{T}} - {\phi_y}^{\mathrm{T}}\right)(1+\alpha)^2. \tag{6.31}$$

Note that in Equation (6.30), the term resulting from $A_x A_y$ vanishes in the subtraction but in Equation (6.31) the term from $A_x A_y$ which includes f^2 remains. This means that $I_0 - I_\pi$ is more subject to the effect of the pinhole than $I_{\pi/2} - I_{-\pi/2}$. By defining the coefficients below,

$$C := \frac{|R_x|^2 - |R_y|^2}{|T_x - T_y|^2}, \tag{6.32}$$

$$D := -\frac{f}{1+\alpha} + \frac{|T_x|\,|T_y| \cos\left({\phi_x}^{\mathrm{T}} - {\phi_y}^{\mathrm{T}}\right)(1+\alpha)}{|T_x - T_y|^2 f}, \tag{6.33}$$

$$E := -\frac{2\,|R_x|\,|R_y| \sin\left({\phi_x}^{\mathrm{R}} - {\phi_y}^{\mathrm{R}}\right)}{|T_x - T_y|^2} \tag{6.34}$$

$$F := \frac{|R_x|\,|R_y| \sin\left({\phi_x}^{\mathrm{R}} - {\phi_y}^{\mathrm{R}}\right)(1+\alpha)}{|T_x - T_y|^2 f}, \tag{6.35}$$

the parameter M can be written as

$$M = \frac{I_{\pi/2} - I_{-\pi/2}}{I_0 - I_\pi} = \frac{C\sin\delta + E\cos\delta + F}{\cos\delta + D}. \tag{6.36}$$

If phase shifter plates such as

$${\phi_x}^{\mathrm{T}} - {\phi_y}^{\mathrm{T}} = (n + 1/2)\pi,\ {\phi_x}^{\mathrm{R}} - {\phi_y}^{\mathrm{R}} = n\pi\ (n \in \mathbb{N}), \tag{6.37}$$

can be set on the transmitted and reflected paths after the PPBS, the parameter M can be greatly simplified to

$$M = \frac{I_{\pi/2} - I_{-\pi/2}}{I_0 - I_\pi} = \frac{C\sin\delta}{\cos\delta + D}, \tag{6.38}$$

$$C = \frac{|R_x|^2 - |R_y|^2}{|T_y - T_x|^2}, \tag{6.39}$$

$$D = -\frac{f}{1+\alpha}. \tag{6.40}$$

Equation (6.38) shows that $\tan\delta$ cannot describe the ratio of the interferogram subtraction M and that M intrinsically contains the parameter D only determined by $f(R_{\mathrm{pin}}; r_2)$ which arises from the pinhole. The phase is derived from Equation (6.38) as follows:

$$\delta = \begin{cases} \sin^{-1}\dfrac{DM}{\sqrt{C^2+M^2}} + \tan^{-1}\dfrac{M}{C} \\ \pi - \sin^{-1}\dfrac{DM}{\sqrt{C^2+M^2}} + \tan^{-1}\dfrac{M}{C} \end{cases}. \tag{6.41}$$

It should be noted that the equation including $+\sin^{-1}$ can be used when $\cos\delta + D > 0$ ($|D| \leq 1$) or $\cos\delta + 1/D > 0$ ($|D| > 1$); otherwise the other equation including $\pi - \sin^{-1}$ can be used. The terms C and D are determined by the polarizing properties and the pinhole size, respectively. δ is identified with δ_{rec} when $C = 1$ and $D = 0$. It is possible that measurements which have been carried out so far include errors due to C and D.

The advantage in this configuration is that it enables the simultaneous measurement of the four interferograms of $I_0, I_\pi, I_{\pi/2}$, and $I_{-\pi/2}$. This system would also have high efficiency because it utilizes both the transmitted and reflected beams.

The term $D(R_{\mathrm{pin}}; x_2, y_2; t)$ is worth special mention because it appears when $R_{\mathrm{pin}} \neq 0$ (see also Figure 6.4). When the PDI is taken into consideration, the term D always exists intrinsically and can be of the order of unity.

6.4 Discussion

To simplify the following discussion, it is assumed that $\alpha(x_1, y_1; t)$ is always zero. $\delta(x_1, y_1; t)$ means the differences between (x_1, y_1) and $(0, 0)$ on pupil 1. The Airy radius is introduced as $R_{\mathrm{Airy}} := 1.22F_1\lambda$ and a parameter as $Q := \delta_{\mathrm{rec}}/\delta$.

6.4.1 Effect of Pinhole Size

In this section, consider the effect of the pinhole, i.e., the effect of the term D appearing in Equation (6.38) on the wavefront sensing. When C equals unity and δ equals $2\pi/10$ which is equivalent to $\lambda/10$, for example, Figure 6.5 shows how far from unity the parameter Q is. Q depends on the pinhole size R_{pin} and the polarization properties of the PPBS.

In case of $R_{\mathrm{pin}} < 0.615R_{\mathrm{Airy}}$ $(= 0.75F_1\lambda)$, Q is 2–3. It is hardly dependent on the pupil coordinate. However, Q for $R_{\mathrm{pin}} > 0.615R_{\mathrm{Airy}}$ $(= 0.75F_1\lambda)$ is more than 2.5 and strongly depends on the pupil coordinate. The reason for the large Q for $R_{\mathrm{pin}} > 0.615R_{\mathrm{Airy}}$ $(= 0.75F_1\lambda)$ is that the term D is nearly -1, which results in the denominator in Equation (6.38) getting a smaller value, though the numerator is less affected. The large R_{pin} also causes an unequal distribution of the reference beam amplitude on pupil 2, being stronger at the center and weaker at the edge. This accounts for the pupil coordinate dependence of Q.

Figure 6.6 shows response curves of $\tan M$ against the given δ at $r_2 = 0.2R_2$. When the red lines in the case in which extinction ratio is infinity is considered, the curve for $R_{\mathrm{pin}} = 0.410R_{\mathrm{Airy}}$ $(= 0.5F_1\lambda)$ departs from linearity more than that for $R_{\mathrm{pin}} = 0.082R_{\mathrm{Airy}}$ $(= 0.1F_1\lambda)$.

6.4.2 Effect of the Polarizing Properties of the PPBS

C is determined only by the polarizing properties of the PPBS. When there is no absorption at the PPBS, for example, a transmittance and reflectance to be $T_y = -R_x = 2\sqrt{2}/3$, and $R_y = -T_x = (1/3)\exp(\sqrt{-1}\pi/2)$. The extinction ratios ($|T_y|^2/|T_x|^2, |R_x|^2/|R_y|^2$) are 8, and C is 0.78. In the limit where the extinction ratios become infinity, C becomes unity. On the other hand, C gets to zero in the case of bad extinction ratios.

Figure 6.7 shows the relatively minor variations of Q depending on the term C. In other words, there is a little difference between $C = 1$ and $C = 0.78$, corresponding to the extinction ratio of infinity and 8, respectively. In Figure 6.6, when $C < 0.8$, i.e., in the case in which the PPBS has poor polarizing properties and the extinction ratio is less than 8, the curves depart from a linearity and develop into "flat-steep-flat" curves, which means that small C cannot be adopted for the wavefront sensor. For the small δ, the small C fulfills a role to reduce Q but, on the contrary, D increases Q.

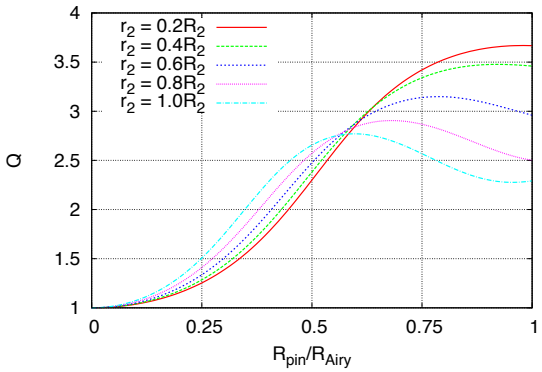

Figure 6.5: Variation of $Q = \delta_{\mathrm{rec}}/\delta$ against the pinhole size R_{pin}. The axis of the ordinate is Q. The abscissa is the size of the pinhole. Unity of the ordinate means that the wavefront error is correctly acquired. The case in which $C = 1$ and $\delta = 2\pi/10$ is plotted.

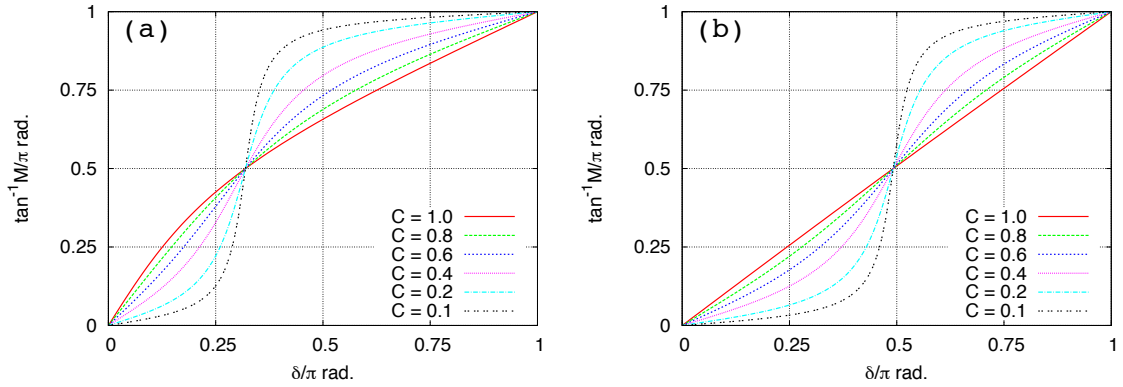

Figure 6.6: Response curves of $\tan M$ against the given δ at $r_2 = 0.2R_2$. (a) $R_{\mathrm{pin}} = 0.410R_{\mathrm{Airy}}$ $(= 0.5F_1\lambda)$. (b) $R_{\mathrm{pin}} = 0.082R_{\mathrm{Airy}}$ $(= 0.1F_1\lambda)$. The flat-steep-flat curves appear when C is getting small.

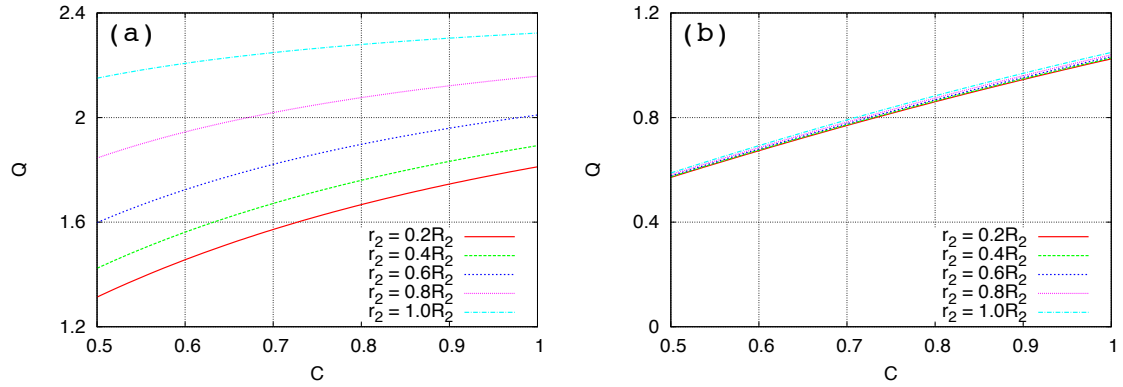

Figure 6.7: Variation of $Q = \delta_{\mathrm{rec}}/\delta$ against the parameter C. The axis of the ordinate is Q. The abscissa is the term C. The case in which $\delta = 2\pi/10$ is plotted. (a) $R_{\mathrm{pin}} = 0.410R_{\mathrm{Airy}}$ $(= 0.5F_1\lambda)$. (b) $R_{\mathrm{pin}}0.082R_{\mathrm{Airy}}$ $(= 0.1F_1\lambda)$.

According to Figures 6.6 and 6.7, extremely high extinction ratios (more than about 8) may not be necessary and that building the proposed sensor is possible except for the poor polarizing properties of the PPBS.

6.4.3 Propagation of Uncertainties

To investigate how large tolerance this system can accept when in manufacturing and whether or not the system can be calibrated uncertainties of the three parameters, C, D, and M are estimated. By using the equation (6.41), absolute values of the following partial differentiations can be calculated:

$$\left|\frac{\partial\delta}{\partial C}\right| = \left|\frac{-CDM}{(C^2+M^2)\sqrt{C^2+M^2-D^2M^2}} - \frac{M}{C^2+M^2}\right|, \tag{6.42}$$

$$\left|\frac{\partial\delta}{\partial D}\right| = \left|\frac{M}{\sqrt{C^2+M^2-D^2M^2}}\right|, \tag{6.43}$$

$$\left|\frac{\partial\delta}{\partial M}\right| = \left|\frac{C^2D}{(C^2+M^2)\sqrt{C^2+M^2-D^2M^2}} + \frac{C}{C^2+M^2}\right|. \tag{6.44}$$

Figures 6.8, 6.9, and 6.10 show the absolute values of the partial differential coefficients in Equations (6.42), (6.43), and (6.44), respectively. Figure 6.8 indicates that $|\partial\delta/\partial C|$ is smaller than 0.5 in most cases and that the accuracy of inferring the term C may not be severe. If $\Delta\delta$ has to be smaller than $\pi/50$ which is equivalent to $\lambda/100$, the uncertainty ΔC has to be smaller than $\pi/25 \sim 1.2\times10^{-1}$.

Figures 6.9 and 6.10 show that the partial differential coefficients are < 1.5 in the range of 0–$0.410R_{\mathrm{Airy}}$ (0–$0.5F_1\lambda$) for the radius of the pinhole R_{pin}. In other words, setting $R_{\mathrm{pin}} < 0.410R_{\mathrm{Airy}}$ $(0.5F_1\lambda)$ will suppress the propagation of the uncertainties of measurements M or inaccurate estimates of D and will decrease the uncertainty of the wavefront error δ. If $\Delta\delta$ has to be $< \pi/50$, the uncertainty ΔD has to be $< \pi/(50\cdot1.5) \sim 4.2\times10^{-2}$ and that of ΔM has to be $< \pi/(50\cdot0.75) \sim 8.4\times10^{-2}$.

The propagation of the above uncertainties can be calculated by using

$$\Delta\delta = \sqrt{\left|\frac{\partial\delta}{\partial C}\right|^2\Delta C^2 + \left|\frac{\partial\delta}{\partial D}\right|^2\Delta D^2 + \left|\frac{\partial\delta}{\partial M}\right|^2\Delta M^2}. \tag{6.45}$$

In the case in which $R_{\mathrm{pin}} = 0.410R_{\mathrm{Airy}}$ $(= 0.5F_1\lambda)$, the following results is obtained when it is assumed that $|\partial\delta/\partial C| < 0.5$, $|\partial\delta/\partial D| < 1.5$, and $|\partial\delta/\partial M| < 0.75$:

$$\Delta\delta < 6.2\times10^{-2} \sim \frac{\pi}{50}\ \mathrm{rad.}, \tag{6.46}$$

where $\Delta C = 7.0\times10^{-2}$, $\Delta D = 2.4\times10^{-2}$, and $\Delta M = 4.8\times10^{-2}$ are achieved. It is revealed

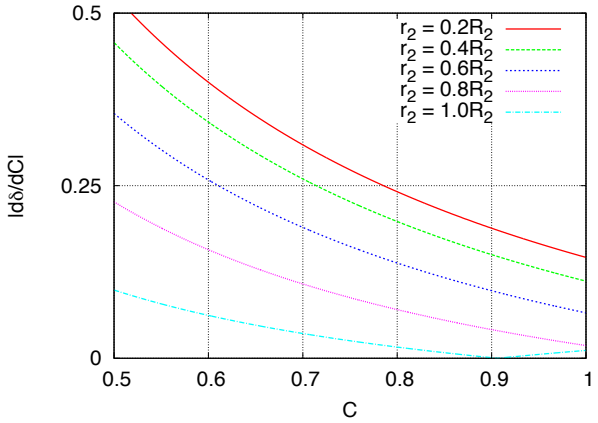

Figure 6.8: $|\partial\delta/\partial C|$ versus C. It is assumed that $\delta = 2\pi/10$ and $R_{\rm pin} = 0.140 R_{\rm Airy}$ $(= 0.5 F_1 \lambda)$.

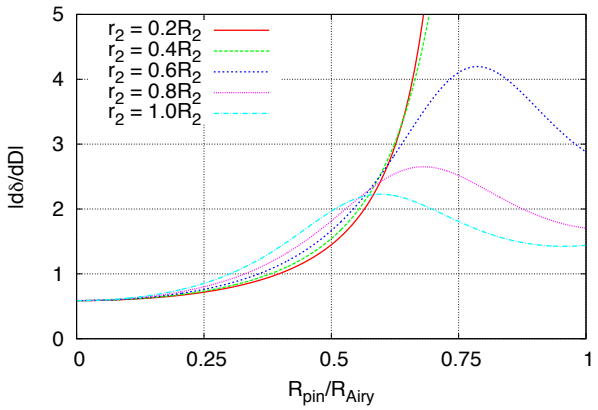

Figure 6.9: $|\partial\delta/\partial D|$ versus $R_{\rm pin}$. It is assumed that $\delta = 2\pi/10$ and $C = 1$. $|\partial\delta/\partial D|$ diverges near the singular point where the denominator in Equation (6.43) becomes zero.

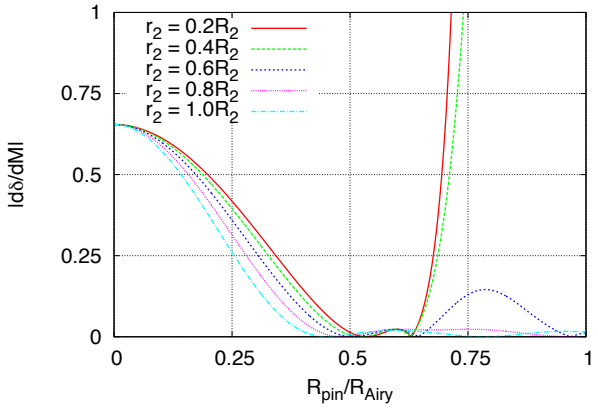

Figure 6.10: $|\partial\delta/\partial M|$ versus $R_{\rm pin}$. It is assumed that $\delta = 2\pi/10$ and $C = 1$. $|\partial\delta/\partial M|$ diverges near the singular point where the denominator in Equation (6.44) becomes zero.

that the uncertainties $\Delta C, \Delta D$, and ΔM need to be estimated within a few percent in order to suppress $\Delta\delta \sim \pi/50$ rad ($\lambda/100$). Thanks to revealing necessary precision of the parameters C and D, one can give feedback on tolerances in manufacturing. If the requisite uncertainty of δ is $\sim \lambda/100$, one can calibrate δ_{rec} by using C and D estimated with a few percent precision. Thus, it is possible to calibrate the system with a small pinhole whose radius is $< 0.410R_{\mathrm{Airy}}\ (= 0.5F_1\lambda)$.

6.5 Summary

A novel wavefront sensor has been proposed and its performance has been studied. The sensor has a PPBS. Both the pinhole and the other part of the PPBS polarize the incident beams but their polarizing directions are orthogonal. The key points of the proposed sensor are that both of the transmitted and reflected beams are used, that both the reference and test beams propagate on common paths, and that four interferograms can be obtained simultaneously. Therefore, measuring of the wavefront error in real time with high precision can be achieved. This sensor works without throwing away part of the energy entering it.

Analytical studies have been conducted in which the Fraunhofer diffraction equation has been solved, revealing the strong effects of the pinhole radius on sensor performance. It is recommended that the pinhole should be smaller than the Airy disk ($R_{\mathrm{pin}} < 0.410R_{\mathrm{Airy}} = 0.5F_1\lambda$) for better performance. If $R_{\mathrm{pin}} < 0.410R_{\mathrm{Airy}} = 0.5F_1\lambda$, the ratio $Q = \delta_{\mathrm{rec}}/\delta$ is less than a factor of 2, the performance is not affected by the pupil coordinate and the propagation of the uncertainties of measuring the interferograms and estimating the term D which stems from the existence of the pinhole (Equation (6.38)) is suppressed. The term C determined by the polarizing properties of the PPBS (Equation (6.38)) does not strongly affect sensor performance, enabling the construction of a novel system using a polarizing element without need for extremely high extinction ratios (i.e., > 8 would be sufficient). The uncertainties of C and D necessary for calibrating the novel system are about a few percent. It means that one calibrate it and the uncertainty of measurements of the wavefront error would be $\lambda/100$.

7

Conclusion

In this thesis, the parameters which describe the properties of an antenna are theoretically considered. In considering a receiving antenna, a receiving beam pattern and an effective aperture area are proved to be the most fundamental parameters. A receiving beam pattern can be measured using a point source. An effective aperture area can be also measured using an isotropic source. Both parameters can determine the properties of an antenna completely. In other words, other parameters, a beam solid angle, main beam efficiency, a beam width, directivity, and gain, are determined by the two. By assuming reciprocity, the parameters mentioned above can be predicted via transmitting properties.

In case of an aperture antenna, the parameters are also explicitly expressed. In addition, if receiver sensitivity is assumed, the parameters describing the antenna properties can be determined only by the parameters of the receiver sensitivity. An aperture efficiency is defined as the ratio of an effective aperture area to a physical aperture area, which is composed of two spillover efficiencies and an optical, or coupling, efficiency. The spillover efficiency at an entrance pupil is ignored until now but it is needed when a wide field-of-view telescope is considered.

When a radio telescope is designed, there are ultimately two requirements. One is that an aperture efficiency is independent of frequency and the other is that one keeps an aperture efficiency as high as possible. In case of a single-beam telescope transmitting an on-axis fundamrntal Gaussian beam, the way to design an optical system satisfying these requirements is known well but the way in case of an arbitrary beam is not known. When a wide field-of-view telescope is considered, generalized theories for an arbitrary beam are necessary.

In Chapter 4, extension of the theories for an on-axis fundamental Gaussian beam is demonstrated theoretically. Frequency-independent condition is proved to be the lens formula. Whenever the lens formula holds, the electric fields at an object plane and an image plane are determined only by the geometry of a system taken into account. It is achieved that the dependence of an aperture efficiency is written analytically as a function of the aberration coefficients and the parameters of detector sensitivity. This expression enables to evaluate both effects of geometry and diffraction. The results are the answers to the questions brought up in Chapter 1.

In generalizing the theories, it is revealed that geometrical optics has an important role even when a radio telescope dealing with strongly coherent wave is considered. A novel method to design a radio telescope is proposed on the basis of the results. The feature of the novel method is the combination of geometrical optics and quasi optics. As a concise application, calculating the aperture efficiency of the 10-m THz telescope in Antarctica which is planned by University of Tsukuba is demonstrated. The optical design is proved to be almost perfect.

Chapter 6 deals with discussion of a novel wavefront sensor, which can be applied to radio devices. Wavefront sensing is an important technique to construct an optical system and to operate a telescope. In radio bands, wavefront sensing will be necessary in the future.

A

Invariance of Coupling Efficiency

Coupling efficiency η_{coup} can be proved to be a constant by evaluating diffraction. Consider a system which is composed of a mirror M located between pupils A and B. The pupils A and B and the mirror M is sufficiently larger than the scale of the wavelength of electromagnetic wave propagating in the system.

The distribution of an electric field $\boldsymbol{E}_1(x_\mathrm{A}, y_\mathrm{A}, z_\mathrm{A})$ is given on the pupil A. The shape of the mirror M is expressed as

$$S = z_\mathrm{M} - F(x_\mathrm{M}, y_\mathrm{M}) = 0. \tag{A.1}$$

The field $\boldsymbol{E}_1(x_\mathrm{A}, y_\mathrm{A}, z_\mathrm{A})$ induces an electric field on the mirror M, which is given by

$$\boldsymbol{E}_1(x_\mathrm{M}, y_\mathrm{M}, z_\mathrm{M}) = C \iint_\mathrm{A} \boldsymbol{E}_1(x_\mathrm{A}, y_\mathrm{A}, z_\mathrm{A}) K(x_\mathrm{A}, y_\mathrm{A}; x_\mathrm{M}, y_\mathrm{M}; k) \mathrm{d}x_\mathrm{A} \mathrm{d}y_\mathrm{A}, \tag{A.2}$$

where C is a constant and

$$\begin{aligned} K(x_\mathrm{A}, y_\mathrm{A}; x_\mathrm{M}, y_\mathrm{M}; k) &:= \frac{\exp\left[\sqrt{-1}k\sqrt{(x_\mathrm{M}-x_\mathrm{A})^2 + (y_\mathrm{M}-y_\mathrm{A})^2 + (F(x_\mathrm{M}-x_\mathrm{A}) - z_\mathrm{A})^2}\right]}{\sqrt{(x_\mathrm{M}-x_\mathrm{A})^2 + (y_\mathrm{M}-y_\mathrm{A})^2 + (F(x_\mathrm{M}-x_\mathrm{A}) - z_\mathrm{A})^2}} \\ &= K(x_\mathrm{M}, y_\mathrm{M}; x_\mathrm{A}, y_\mathrm{A}; k) = K^*(x_\mathrm{M}, y_\mathrm{M}; x_\mathrm{A}, y_\mathrm{A}; -k). \end{aligned} \tag{A.3}$$

After reflecting on the mirror M, the field $\boldsymbol{E}_1(x_\mathrm{M}, y_\mathrm{M}, z_\mathrm{M})$ is transformed into

$$\boldsymbol{E}_1'(x_\mathrm{M}, y_\mathrm{M}, z_\mathrm{M}) = \boldsymbol{E}_1(x_\mathrm{M}, y_\mathrm{M}, z_\mathrm{M}) + 2\boldsymbol{n}(x_\mathrm{M}, y_\mathrm{M}) \times \left[\boldsymbol{n}(x_\mathrm{M}, y_\mathrm{M}) \times \boldsymbol{E}_1(x_\mathrm{M}, y_\mathrm{M}, z_\mathrm{M})\right], \tag{A.4}$$

where $\boldsymbol{n}(x_\mathrm{M}, y_\mathrm{M}) = \mathrm{grad}\, S / |\mathrm{grad}\, S|$. Thus, one can obtain the field on the pupil B, $\boldsymbol{E}_1(x_\mathrm{B}, y_\mathrm{B}, z_\mathrm{B})$, induced by the field $\boldsymbol{E}_1(x_\mathrm{A}, y_\mathrm{A}, z_\mathrm{A})$.

$$\begin{aligned} \boldsymbol{E}_1(x_\mathrm{B}, y_\mathrm{B}, z_\mathrm{B}) &= C^* \iint_\mathrm{M} \boldsymbol{E}_1'(x_\mathrm{M}, y_\mathrm{M}, z_\mathrm{M}) K(x_\mathrm{M}, y_\mathrm{M}; x_\mathrm{B}, y_\mathrm{B}; -k) \mathrm{d}x_\mathrm{M} \mathrm{d}y_\mathrm{M} \\ &= |C|^2 \iint_\mathrm{M} \mathrm{d}x_\mathrm{M} \mathrm{d}y_\mathrm{M} \iint_\mathrm{A} \mathrm{d}x_\mathrm{A} \mathrm{d}y_\mathrm{A} K(x_\mathrm{A}, y_\mathrm{A}; x_\mathrm{M}, y_\mathrm{M}; k) K^*(x_\mathrm{B}, y_\mathrm{B}; x_\mathrm{M}, y_\mathrm{M}; k) \\ &\qquad \times \left\{\boldsymbol{E}_1(x_\mathrm{A}, y_\mathrm{A}, z_\mathrm{A}) + 2\boldsymbol{n} \times \left[\boldsymbol{n} \times \boldsymbol{E}_1(x_\mathrm{A}, y_\mathrm{A}, z_\mathrm{A})\right]\right\} \end{aligned} \tag{A.5}$$

Consider the coupling efficiency $\mathfrak{C}(z_\mathrm{B})$ of $\boldsymbol{E}_1(x_\mathrm{B}, y_\mathrm{B}, z_\mathrm{B})$ and $\boldsymbol{E}_2(x_\mathrm{B}, y_\mathrm{B}, z_\mathrm{B})$ on the pupil B.

$$\begin{aligned} \mathfrak{C}(z_\mathrm{B}) &= \iint_\mathrm{B} \boldsymbol{E}_1(x_\mathrm{B}, y_\mathrm{B}, z_\mathrm{B}) \cdot \boldsymbol{E}_2^*(x_\mathrm{B}, y_\mathrm{B}, z_\mathrm{B}) \mathrm{d}x_\mathrm{B} \mathrm{d}y_\mathrm{B} \\ &= |C|^2 \iint_\mathrm{B} \mathrm{d}x_\mathrm{B} \mathrm{d}y_\mathrm{B} \iint_\mathrm{M} \mathrm{d}x_\mathrm{M} \mathrm{d}y_\mathrm{M} \iint_\mathrm{A} \mathrm{d}x_\mathrm{A} \mathrm{d}y_\mathrm{A} K(x_\mathrm{A}, y_\mathrm{A}; x_\mathrm{M}, y_\mathrm{M}; k) K^*(x_\mathrm{B}, y_\mathrm{B}; x_\mathrm{M}, y_\mathrm{M}; k) \\ &\qquad \times \left\{\boldsymbol{E}_1(x_\mathrm{A}, y_\mathrm{A}, z_\mathrm{A}) + 2\boldsymbol{n} \times \left[\boldsymbol{n} \times \boldsymbol{E}_1(x_\mathrm{A}, y_\mathrm{A}, z_\mathrm{A})\right]\right\} \cdot \boldsymbol{E}_2^*(x_\mathrm{B}, y_\mathrm{B}, z_\mathrm{B}) \end{aligned} \tag{A.6}$$

By using the vector triple product expansion $\boldsymbol{a} \times (\boldsymbol{b} \times \boldsymbol{c}) = (\boldsymbol{a} \cdot \boldsymbol{c})\boldsymbol{b} - (\boldsymbol{a} \cdot \boldsymbol{b})\boldsymbol{c}$, the product in Equation (A.6) meets the following relation:

$$\boldsymbol{n} \times [\boldsymbol{n} \times \boldsymbol{E}_1(x_\mathrm{A}, y_\mathrm{A}, z_\mathrm{A})] \cdot \boldsymbol{E}_2^*(x_\mathrm{B}, y_\mathrm{B}, z_\mathrm{B}) = \boldsymbol{n} \times [\boldsymbol{n} \times \boldsymbol{E}_2^*(x_\mathrm{A}, y_\mathrm{A}, z_\mathrm{A})] \cdot \boldsymbol{E}_1(x_\mathrm{B}, y_\mathrm{B}, z_\mathrm{B}). \tag{A.7}$$

Equation (A.6) is rearranged by using Equation (A.7), then

$$\begin{aligned}\mathfrak{C}(z_\mathrm{B}) = |C|^2 \iint_\mathrm{A} \mathrm{d}x_\mathrm{A}\mathrm{d}y_\mathrm{A} \iint_\mathrm{M} \mathrm{d}x_\mathrm{M}\mathrm{d}y_\mathrm{M} \iint_\mathrm{B} \mathrm{d}x_\mathrm{B}\mathrm{d}y_\mathrm{B} K^*(x_\mathrm{M}, y_\mathrm{M}; x_\mathrm{A}, y_\mathrm{A}; -k) K^*(x_\mathrm{B}, y_\mathrm{B}; x_\mathrm{M}, y_\mathrm{M}; k) \\ \times \{\boldsymbol{E}_2^*(x_\mathrm{B}, y_\mathrm{B}, z_\mathrm{B}) + 2\boldsymbol{n} \times [\boldsymbol{n} \times \boldsymbol{E}_2^*(x_\mathrm{B}, y_\mathrm{B}, z_\mathrm{B})]\} \cdot \boldsymbol{E}_1(x_\mathrm{A}, y_\mathrm{A}, z_\mathrm{A}).\end{aligned} \tag{A.8}$$

The right hand side of Equation (A.8) is regarded as the complex conjugate of coupling efficiency at the pupil A between the field $\boldsymbol{E}_1(x_\mathrm{A}, y_\mathrm{A}, z_\mathrm{A})$ and the field induced at the pupil A by the field $\boldsymbol{E}_2(x_\mathrm{B}, y_\mathrm{B}, z_\mathrm{B})$ at the pupil B. Consequently, $\mathfrak{C}(z_\mathrm{B}) = \mathfrak{C}^*(z_\mathrm{A})$ and $|\mathfrak{C}(z_\mathrm{B})|^2 = |\mathfrak{C}^*(z_\mathrm{A})|^2$ are derived, which means that the coupling efficiency η_coup is invariant through the whole optical path.

B

Zernike annular polynomials

The normalized Zernike annular polynomials are of the form

$$Z_n{}^m(\rho,\theta;\varepsilon) = \begin{cases} N_n{}^m R_n{}^m(\rho;\varepsilon)\cos(m\theta) & (m \geq 0) \\ N_n{}^m R_n{}^{|m|}(\rho;\varepsilon)\sin(m\theta) & (m < 0) \end{cases}, \tag{B.1}$$

and defined in the domain $0 \leq \varepsilon \leq \rho \leq 1$ $(\varepsilon < 1)$ and $0 \leq \theta \leq 2\pi$ (Mahajan 1981), where m is an integer, n a non-negative integer, $n \geq |m|$, and $n - |m|$ even. The normalized factor and orthogonality are as follows:

$$N_n{}^m = \sqrt{\frac{2(n+1)}{1+\delta_{m0}}}, \tag{B.2}$$

$$\int_\varepsilon^1 \mathrm{d}\rho \int_0^{2\pi} \mathrm{d}\theta\, \rho Z_n{}^m(\rho,\theta;\varepsilon) Z_p{}^q(\rho,\theta;\varepsilon) = \pi(1-\varepsilon^2)\delta_{np}\delta_{mq}. \tag{B.3}$$

In the case of $\varepsilon = 0$, the domain of definition is a circle and $Z_n{}^m(\rho,\theta;\varepsilon)$ reduces to the Zernike circle polynomials.

The terms used in this paper are tabulated in Table B.1. In Table B.2, the polynomials of the integral I_p defined in Equation (4.61) are shown. The notation for the polynomials of ε defined in Equation (4.65) is used.

Table B.1: Radial polynomials ${R_n}^m(\rho;\varepsilon)$.

$(n,\lvert m\rvert)$	${R_n}^{\lvert m\rvert}(\rho;\varepsilon)$	${N_n}^m$
$(0,0)$	1	1
$(1,1)$	$\dfrac{\rho}{\sqrt{[1,1]}}$	2
$(2,0)$	$\dfrac{2\rho^2-[1,1]}{[1,-1]}$	$\sqrt{3}$
$(2,2)$	$\dfrac{\rho^2}{\sqrt{[1,1,1]}}$	$\sqrt{6}$
$(3,1)$	$\dfrac{3[1,1]\rho^3-2[1,1,1]\rho}{[1,-1]\sqrt{[1,1][1,4,1]}}$	$\sqrt{8}$
$(3,3)$	$\dfrac{\rho^3}{\sqrt{[1,1,1,1]}}$	$\sqrt{8}$
$(4,0)$	$\dfrac{6\rho^4-6[1,1]\rho^2+[1,4,1]}{[1,-1]^2}$	$\sqrt{5}$
$(4,2)$	$\dfrac{4[1,1,1]\rho^4-3[1,1,1,1]\rho^2}{[1,-1]\sqrt{[1,1,1][1,4,10,4,1]}}$	$\sqrt{10}$
$(4,4)$	$\dfrac{\rho^4}{\sqrt{[1,1,1,1,1]}}$	$\sqrt{10}$
$(5,1)$	$\dfrac{10[1,4,1]\rho^5-12[1,4,4,1]\rho^3+3[1,4,10,4,1]\rho}{[1,-1]^2\sqrt{[1,4,1][1,9,9,1]}}$	$\sqrt{12}$
$(5,3)$	$\dfrac{5[1,1,1,1]\rho^5-4[1,1,1,1,1]\rho^3}{[1,-1]\sqrt{[1,1,1,1][1,4,10,20,10,4,1]}}$	$\sqrt{12}$
$(6,0)$	$\dfrac{20\rho^6-30[1,1]\rho^4+12[1,3,1]\rho^2-[1,9,9,1]}{[1,-1]^3}$	$\sqrt{7}$
$(6,2)$	$\dfrac{15[1,4,10,4,1]\rho^6-20[1,4,10,10,4,1]\rho^4+6[1,4,10,20,10,4,1]\rho^2}{[1,-1]^2\sqrt{[1,4,10,4,1][1,9,45,65,45,9,1]}}$	$\sqrt{14}$
$(7,1)$	$\dfrac{35[1,9,9,1]\rho^7-60[1,9,15,9,1]\rho^5+30[1,9,25,25,9,1]\rho^3-4[1,9,45,65,45,9,1]\rho}{[1,-1]^3\sqrt{[1,9,9,1][1,16,36,16,1]}}$	4
$(8,0)$	$\dfrac{70\rho^8-140[1,1]\rho^6+90[1,8/3,1]\rho^4-20[1,6,6,1]\rho^2+[1,16,36,16,1]}{[1,-1]^4}$	3

Table B.2: Polynomials $\tilde{R}_n{}^{|m|}(I_p)$.

$(n,\|m\|)$	$\tilde{R}_n{}^{\|m\|}(I_p)$
$(0,0)$	I_p
$(1,1)$	$\dfrac{I_p}{\sqrt{[1,1]}}$
$(2,0)$	$\dfrac{2I_p-[1,1]I_{p-2}}{[1,-1]}$
$(2,2)$	$\dfrac{I_p}{\sqrt{[1,1,1]}}$
$(3,1)$	$\dfrac{3[1,1]I_p-2[1,1,1]I_{p-2}}{[1,-1]\sqrt{[1,1][1,4,1]}}$
$(3,3)$	$\dfrac{I_p}{\sqrt{[1,1,1,1]}}$
$(4,0)$	$\dfrac{6I_p-6[1,1]I_{p-2}+[1,4,1]I_{p-4}}{[1,-1]^2}$
$(4,2)$	$\dfrac{4[1,1,1]I_p-3[1,1,1,1]I_{p-2}}{[1,-1]\sqrt{[1,1,1][1,4,10,4,1]}}$
$(4,4)$	$\dfrac{I_p}{\sqrt{[1,1,1,1,1]}}$
$(5,1)$	$\dfrac{10[1,4,1]I_p-12[1,4,4,1]I_{p-2}+3[1,4,10,4,1]I_{p-4}}{[1,-1]^2\sqrt{[1,4,1][1,9,9,1]}}$
$(5,3)$	$\dfrac{5[1,1,1,1]I_p-4[1,1,1,1,1]I_{p-2}}{[1,-1]\sqrt{[1,1,1,1][1,4,10,20,10,4,1]}}$
$(6,0)$	$\dfrac{20I_p-30[1,1]I_{p-2}+12[1,3,1]I_{p-4}-[1,9,9,1]I_{p-6}}{[1,-1]^3}$
$(6,2)$	$\dfrac{15[1,4,10,4,1]I_p-20[1,4,10,10,4,1]I_{p-2}+6[1,4,10,20,10,4,1]I_{p-4}}{[1,-1]^2\sqrt{[1,4,10,4,1][1,9,45,65,45,9,1]}}$
$(7,1)$	$\dfrac{35[1,9,9,1]I_p-60[1,9,15,9,1]I_{p-2}+30[1,9,25,25,9,1]I_{p-4}-4[1,9,45,65,45,9,1]I_{p-6}}{[1,-1]^3\sqrt{[1,9,9,1][1,16,36,16,1]}}$
$(8,0)$	$\dfrac{70I_p-140[1,1]I_{p-2}+90[1,8/3,1]I_{p-4}-20[1,6,6,1]I_{p-6}+[1,16,36,16,1]I_{p-8}}{[1,-1]^4}$

C

Coefficients C_n^m

$$
\begin{aligned}
{C_0}^0 &= 1 - \frac{k^2}{2}\left[\left({A_1}^1\right)^2 + \left({B_1}^1\right)^2 + \left({A_2}^0\right)^2 + \left({A_2}^2\right)^2 + \left({B_2}^2\right)^2 + \left({A_3}^1\right)^2 + \left({B_3}^1\right)^2 + \left({A_4}^0\right)^2\right] \\
{C_1}^1 &= \sqrt{-1}k{A_1}^1 - \frac{k^2}{2}\left[\frac{2[1,-1]}{\sqrt{3}[1,1]}{A_1}^1{A_2}^0 + \frac{2\sqrt{2[1,1,1]}}{\sqrt{3}[1,1]}\left({A_1}^1{A_2}^2 + {B_1}^1{B_2}^2\right) + \frac{2\sqrt{2[1,4,1]}}{\sqrt{3}[1,1]}{A_2}^0{A_3}^1\right. \\
&\qquad \left. + \frac{[1,-1]\sqrt{[1,4,1]}}{\sqrt{3}[1,1]\sqrt{[1,1,1]}}\left({A_2}^2{A_3}^1 + {B_2}^2{B_3}^1\right) + \frac{2\sqrt{2}[1,-1]}{\sqrt{5[1,4,1]}}{A_3}^1{A_4}^0\right] \\
{C_1}^{-1} &= \sqrt{-1}k{B_1}^1 - \frac{k^2}{2}\left[\frac{2[1,-1]}{\sqrt{3}[1,1]}{B_1}^1{A_2}^0 + \frac{2\sqrt{2[1,1,1]}}{\sqrt{3}[1,1]}\left({A_1}^1{B_2}^2 - {B_1}^1{A_2}^2\right) + \frac{2\sqrt{2[1,4,1]}}{\sqrt{3}[1,1]}{A_2}^0{B_3}^1\right. \\
&\qquad \left. + \frac{[1,-1]\sqrt{[1,4,1]}}{\sqrt{3}[1,1]\sqrt{[1,1,1]}}\left({B_2}^2{A_3}^1 - {A_2}^2{B_3}^1\right) + \frac{2\sqrt{2}[1,-1]}{\sqrt{5[1,4,1]}}{B_3}^1{A_4}^0\right] \\
{C_2}^0 &= \sqrt{-1}k{A_2}^0 - \frac{k^2}{2}\left\{\frac{[1,-1]}{\sqrt{3}[1,1]}\left[\left({A_1}^1\right)^2 + \left({B_1}^1\right)^2\right] + \frac{2\sqrt{2[1,4,1]}}{\sqrt{3}[1,1]}\left({A_1}^1{A_3}^1 + {B_1}^1{B_3}^1\right)\right. \\
&\qquad + \frac{4}{\sqrt{5}}{A_2}^0{A_4}^0 + \frac{\sqrt{3}[1,1][1,-1]}{2[1,1,1]}\left[\left({A_2}^2\right)^2 + \left({B_2}^2\right)^2\right] \\
&\qquad \left. + \frac{[1,-1][1,-8,1]}{5\sqrt{3}[1,1][1,4,1]}\left[\left({A_3}^1\right)^2 + \left({B_3}^1\right)^2\right]\right\} \\
{C_2}^2 &= \sqrt{-1}k{A_2}^2 - \frac{k^2}{2}\left\{\frac{\sqrt{2[1,1,1]}}{\sqrt{3}[1,1]}\left[\left({A_1}^1\right)^2 - \left({B_1}^1\right)^2\right] + \frac{[1,-1]\sqrt{[1,4,1]}}{\sqrt{3}[1,1]\sqrt{[1,1,1]}}\left({A_1}^1{A_3}^1 - {B_1}^1{B_3}^1\right)\right. \\
&\qquad + \frac{\sqrt{3}[1,1][1,-1]}{[1,1,1]}{A_2}^0{A_2}^2 + \frac{[1,-1]^2}{\sqrt{5}[1,1,1]}{A_2}^2{A_4}^0 \\
&\qquad \left. + \frac{2\sqrt{2}[2,10,21,10,2]}{5\sqrt{3}[1,1][1,4,1]\sqrt{[1,1,1]}}\left[\left({A_3}^1\right)^2 - \left({B_3}^1\right)^2\right]\right\} \\
{C_2}^{-2} &= \sqrt{-1}k{B_2}^2 - \frac{k^2}{2}\left\{\frac{2\sqrt{2[1,1,1]}}{\sqrt{3}[1,1]}{A_1}^1{B_1}^1 + \frac{[1,-1]\sqrt{[1,4,1]}}{\sqrt{3}[1,1]\sqrt{[1,1,1]}}\left({A_1}^1{B_3}^1 + {B_1}^1{A_3}^1\right)\right. \\
&\qquad + \frac{\sqrt{3}[1,1][1,-1]}{[1,1,1]}{A_2}^0{B_2}^2 + \frac{[1,-1]^2}{\sqrt{5}[1,1,1]}{B_2}^2{A_4}^0 \\
&\qquad \left. + \frac{4\sqrt{2}[2,10,21,10,2]}{5\sqrt{3}[1,1][1,4,1]\sqrt{[1,1,1]}}{A_3}^1{B_3}^1\right\} \\
{C_3}^1 &= \sqrt{-1}k{A_3}^1 - \frac{k^2}{2}\left[\frac{2\sqrt{2[1,4,1]}}{\sqrt{3}[1,1]}{A_1}^1{A_2}^0 + \frac{[1,-1\sqrt{[1,4,1]}]}{\sqrt{3}[1,1][1,1,1]}\left({A_1}^1{A_2}^2 + {B_1}^1{B_2}^2\right)\right. \\
&\qquad + \frac{2\sqrt{2}[1,-1]}{\sqrt{5[1,4,1]}}{A_1}^1{A_4}^0 + \frac{2[1,-1][1,-8,1]}{5\sqrt{3}[1,1][1,4,1]}{A_2}^0{A_3}^1 \\
&\qquad \left. + \frac{4\sqrt{2}[2,10,21,10,2]}{5\sqrt{3}[1,1][1,4,1]\sqrt{[1,1,1]}}\left({A_2}^2{A_3}^1 + {B_2}^2{B_3}^1\right) + \frac{2[1,10,1]}{\sqrt{5}[1,4,1]}{A_3}^1{A_4}^0\right]
\end{aligned}
$$

$$C_3{}^{-1} = \sqrt{-1}kB_3{}^1 - \frac{k^2}{2}\left[\frac{2\sqrt{2[1,4,1]}}{\sqrt{3}[1,1]}B_1{}^1A_2{}^0 + \frac{[1,-1\sqrt{[1,4,1]}]}{\sqrt{3}[1,1][1,1,1]}\left(A_1{}^1B_2{}^2 - B_1{}^1A_2{}^2\right)\right.$$
$$+\frac{2\sqrt{2}[1,-1]}{\sqrt{5[1,4,1]}}B_1{}^1A_4{}^0 + \frac{2[1,-1][1,-8,1]}{5\sqrt{3}[1,1][1,4,1]}A_2{}^0B_3{}^1$$
$$\left.+\frac{4\sqrt{2}[2,10,21,10,2]}{5\sqrt{3}[1,1][1,4,1]\sqrt{[1,1,1]}}\left(B_2{}^2A_3{}^1 - A_2{}^2B_3{}^1\right) + \frac{2[1,10,1]}{\sqrt{5}[1,4,1]}B_3{}^1A_4{}^0\right]$$

$$C_3{}^3 = -\frac{k^2}{2}\left[\frac{\sqrt{3[1,0,1]}}{\sqrt{[1,1,1]}}\left(A_1{}^1A_2{}^2 - B_1{}^1B_2{}^2\right) + \frac{2\sqrt{6}[1,-1][1,3,1]}{5\sqrt{[1,0,1][1,1,1][1,4,1]}}\left(A_2{}^2A_3{}^1 - B_2{}^2B_3{}^1\right)\right]$$

$$C_3{}^{-3} = -\frac{k^2}{2}\left[\frac{\sqrt{3[1,0,1]}}{\sqrt{[1,1,1]}}\left(A_1{}^1B_2{}^2 + B_1{}^1A_2{}^2\right) + \frac{2\sqrt{6}[1,-1][1,3,1]}{5\sqrt{[1,0,1][1,1,1][1,4,1]}}\left(A_2{}^2B_3{}^1 + B_2{}^2A_3{}^1\right)\right]$$

$$C_4{}^0 = \sqrt{-1}kA_4{}^0 - \frac{k^2}{2}\left\{\frac{2\sqrt{2}[1,-1]}{\sqrt{5[1,4,1]}}\left(A_1{}^1A_3{}^1 + B_1{}^1B_3{}^1\right) + \frac{2}{\sqrt{5}}\left(A_2{}^0\right)^2 + \frac{2\sqrt{5}}{7}\left(A_4{}^0\right)^2\right.$$
$$\left.+\frac{[1,-1]^2}{2\sqrt{5}[1,1,1]}\left[\left(A_2{}^2\right)^2 + \left(B_2{}^2\right)^2\right] + \frac{[1,10,1]}{\sqrt{5}[1,4,1]}\left[\left(A_3{}^1\right)^2 + \left(B_3{}^1\right)^2\right]\right\}$$

$$C_4{}^2 = -\frac{k^2}{2}\left\{\frac{3\sqrt{[1,4,10,4,1]}}{\sqrt{5[1,1,1][1,4,1]}}\left(A_1{}^1A_3{}^1 - B_1{}^1B_3{}^1\right) + \frac{\sqrt{3}[1,-1][1,1]^3}{[1,1,1]\sqrt{[1,4,10,4,1]}}A_2{}^2A_4{}^0\right.$$
$$\left.+\frac{3\sqrt{[1,4,10,4,1]}}{\sqrt{5}[1,1,1]}A_2{}^0A_2{}^2 + \frac{12[0,0,1,-1]}{\sqrt{10}[1,4,1]\sqrt{[1,1,1][1,4,10,4,1]}}\left[\left(B_3{}^1\right)^2 - \left(A_3{}^1\right)^2\right]\right\}$$

$$C_4{}^{-2} = -\frac{k^2}{2}\left\{\frac{3\sqrt{[1,4,10,4,1]}}{\sqrt{5[1,1,1][1,4,1]}}\left(A_1{}^1B_3{}^1 + B_1{}^1A_3{}^1\right) + \frac{\sqrt{3}[1,-1][1,1]^3}{[1,1,1]\sqrt{[1,4,10,4,1]}}B_2{}^2A_4{}^0\right.$$
$$\left.+\frac{3\sqrt{[1,4,10,4,1]}}{\sqrt{5}[1,1,1]}A_2{}^0B_2{}^2 - \frac{24[0,0,1,-1]}{\sqrt{10}[1,4,1]\sqrt{[1,1,1][1,4,10,4,1]}}A_3{}^1B_3{}^1\right\}$$

$$C_4{}^4 = -\frac{3k^2\sqrt{[1,1,1,1,1]}}{2\sqrt{10}[1,1,1]}\left[\left(A_2{}^2\right)^2 - \left(B_2{}^2\right)^2\right]$$

$$C_4{}^{-4} = -\frac{3k^2\sqrt{[1,1,1,1,1]}}{\sqrt{10}[1,1,1]}A_2{}^2B_2{}^2$$

$$C_5{}^1 = -\frac{k^2}{2}\left[\frac{2\sqrt{3[1,8,1]}}{\sqrt{5[1,4,1]}}A_1{}^1A_4{}^0 + \frac{6\sqrt{2}[1,1]\sqrt{[1,8,1]}}{5[1,4,1]}A_2{}^0A_3{}^1\right.$$
$$\left.+\frac{3[1,1][1,-1]\sqrt{[1,8,1]}}{5[1,4,1]\sqrt{[1,1,1]}}\left(A_2{}^2A_3{}^1 + B_2{}^2B_3{}^1\right) + \frac{2\sqrt{6}[1,-1][1,-10,1]}{7\sqrt{5}[1,4,1]\sqrt{[1,8,1]}}A_3{}^1A_4{}^0\right]$$

$$C_5{}^{-1} = -\frac{k^2}{2}\left[\frac{2\sqrt{3[1,8,1]}}{\sqrt{5[1,4,1]}}B_1{}^1A_4{}^0 + \frac{6\sqrt{2}[1,1]\sqrt{[1,8,1]}}{5[1,4,1]}A_2{}^0B_3{}^1\right.$$
$$\left.+\frac{3[1,1][1,-1]\sqrt{[1,8,1]}}{5[1,4,1]\sqrt{[1,1,1]}}\left(B_2{}^2A_3{}^1 - A_2{}^2B_3{}^1\right) + \frac{2\sqrt{6}[1,-1][1,-10,1]}{7\sqrt{5}[1,4,1]\sqrt{[1,8,1]}}B_3{}^1A_4{}^0\right]$$

$$C_5{}^3 = -\frac{3k^2\sqrt{[1,4,10,20,10,4,1]}}{5\sqrt{[1,0,1][1,1,1][1,4,1]}}\left(A_2{}^2A_3{}^1 - B_2{}^2B_3{}^1\right)$$

$$C_5{}^{-3} = -\frac{3k^2\sqrt{[1,4,10,20,10,4,1]}}{5\sqrt{[1,0,1][1,1,1][1,4,1]}}\left(A_2{}^2B_3{}^1 + B_2{}^2A_3{}^1\right)$$

$$
\begin{aligned}
{C_6}^0 &= -\frac{k^2}{2}\left\{\frac{6\sqrt{15}}{5\sqrt{7}}{A_2}^0{A_4}^0 + \frac{9[1,1][1,-1]}{5\sqrt{7}[1,4,1]}\left[\left({A_3}^1\right)^2 + \left({B_3}^1\right)^2\right]\right\} \\
{C_6}^2 &= -\frac{k^2}{2}\left\{\frac{4\sqrt{15[1,9,45,65,45,9,1]}}{5\sqrt{7[1,1,1][1,4,10,4,1]}}{A_2}^2{A_4}^0 + \frac{12[1,1]\sqrt{[1,9,45,65,45,9,1]}}{5\sqrt{14}[1,4,1]\sqrt{[1,4,10,4,1]}}\left[\left({A_3}^1\right)^2 - \left({B_3}^1\right)^2\right]\right\} \\
{C_6}^{-2} &= -\frac{k^2}{2}\left[\frac{4\sqrt{15[1,9,45,65,45,9,1]}}{5\sqrt{7[1,1,1][1,4,10,4,1]}}{B_2}^2{A_4}^0 + \frac{24[1,1]\sqrt{[1,9,45,65,45,9,1]}}{5\sqrt{14}[1,4,1]\sqrt{[1,4,10,4,1]}}{A_3}^1{B_3}^1\right] \\
{C_7}^1 &= -\frac{9k^2\sqrt{10[1,16,36,16,1]}}{35\sqrt{[1,4,1][1,8,1]}}{A_3}^1{A_4}^0 \\
{C_7}^{-1} &= -\frac{9k^2\sqrt{10[1,16,36,16,1]}}{35\sqrt{[1,4,1][1,8,1]}}{B_3}^1{A_4}^0 \\
{C_8}^0 &= -\frac{3k^2}{7}\left({A_4}^0\right)^2
\end{aligned}
$$

Bibliography

Anderson, C. S. 1995, Applied Optics, 34, 7474

Arimoto, A. 1974, Journal of the Optical Society of America (1917-1983), 64, 850

Balanis, C. A. 2005, *Antenna theory : analysis and design, 3rd edition* (Wiley-Interscience, New Jersey)

Baselmans, J. 2012, Journal of Low Temperature Physics, 167, 292

Born, M. & Wolf, E. 1997, *Principles of Optics: Electromagnetic Theory of Propagation, Interference and Diffraction of Light, Sixth Edition* (Cambridge University Press, Cambridge)

Carlstrom, J. E., Ade, P. A. R., Aird, K. A., *et al.* 2011, Publications of the Astronomical Society of the Pacific, 123, 568

Carson, J. R. 1924, The Bell System Technical Journal, 3, 393

Carson, J. R. 1930, The Bell System Technical Journal, 9, 325

Chang, S. & Prata, A. 2005, Journal of the Optical Society of America A, 22, 2454

Chu, T.-S. 1983, IEEE Transactions on Antennas and Propagation, 31, 614

Fowler, J. W., Niemack, M. D., Dicker, S. R., *et al.* 2007, Applied Optics, 46, 3444

Fried, D. L. 1965, Journal of the Optical Society of America (1917-1983), 55, 1427

Glenn, J., Bertoldi, F., Carpenter, J., *et al.* 2012, *CCAT Science Requirements*

Glückstad, J. & Mogensen, P. C. 2001, Applied optics, 40, 268

Goldsmith, P. 1998, *Quasioptical Systems: Gaussian Beam Quasioptical Propogation and Applications* (IEEE Press, New Jersey)

Goodman, J. W. 2005, *Introduction to Fourier optics* (Poberts & Company, Colorado)

Gradshteyn, I. S., Ryzhik, I. M., Jeffrey, A., & Zwillinger, D. 2007, *Table of Integrals, Series, and Products* (Elsevier Academic Press, Massachusetts)

Imada, H., Matsuo, T., Yamamoto, K., & Kino, M. 2015a, Applied Optics, 54, 7870

Imada, H. & Nagai, M. 2016, in preparation

Imada, H., Nagai, M., Kino, M., *et al.* 2015b, IEEE Transactions on Terahertz Science and Technology, 5, 57

Kataza, H., Wada, T., Sakon, I., *et al.* 2012, in *Space Telescopes and Instrumentation 2012: Optical, Infrared, and Millimeter Wave, Society of Photo-Optical Instrumentation Engineers (SPIE) Conference Series*, Vol. 8442, 84420Q

Kraus, J. & Marhefka, R. 2002, *Antennas for all applications*, McGraw-Hill series in electrical engineering (McGraw-Hill, New York)

Kraus, J. D. 1966, *Radio astronomy* (McGraw-Hill, New York)

Lingfeng, C. & Dingguo, S. 2007, in *Optical Design and Testing III, Society of Photo-Optical Instrumentation Engineers (SPIE) Conference Series*, Vol. 6834, 68342N

Lowenthal, D. 1974, Applied optics, 13, 2126

Mahajan, V. N. 1981, Journal of the Optical Society of America (1917-1983), 71, 75

Mahajan, V. N. 1982, Journal of the Optical Society of America (1917-1983), 72, 1258

Mahajan, V. N. 1983, Journal of the Optical Society of America (1917-1983), 73, 860

Mahajan, V. N. 1986, Journal of the Optical Society of America A, 3, 470

Malacara, D. 2007, *Optical shop testing* (John Wiley & Sons, New Jersey)

Martin, D. H. & Bowen, J. W. 1993, IEEE Transactions on Microwave Theory and Techniques, 41, 1676

Millerd, J. E., Brock, N. J., Hayes, J. B., & Wyant, J. C. 2004, in *Interferometry XII: Techniques and Analysis, Society of Photo-Optical Instrumentation Engineers (SPIE) Conference Series*, Vol. 5531, 264

Murphy, J. A. 1987, International Journal of Infrared and Millimeter Waves, 8, 1165

Nagai, M. & Imada, H. 2016, in preparation

Naulleau, P., Goldberg, K. A., Lee, S. H., *et al.* 2000, in *AIP Conference Proceedings*, 66

Nitta, T., Karatsu, K., Sekimoto, Y., *et al.* 2014, Journal of Low Temperature Physics, 176, 684

Noll, R. J. 1976, Journal of the Optical Society of America (1917-1983), 66, 207

Nyquist, H. 1928, Physical Review, 32, 110

Olmi, L. & Bolli, P. 2007, Applied optics, 46, 4092

Padin, S. 2013, *CCAT Telescope Project Book*

Padin, S., Hollister, M., Radford, S., *et al.* 2010, in *Ground-based and Airborne Telescopes III, Society of Photo-Optical Instrumentation Engineers (SPIE) Conference Series*, Vol. 7733, 77334Y

Padin, S., Staniszewski, Z., Keisler, R., *et al.* 2008, Applied Optics, 47, 4418

Platt, B. C. & Shack, R. 2001, Journal of Refractive Surgery, 17, S573

Radiant Zemax. 2014, *Zemax 13: Optical Design Program User's Manual*

Remijan, A., Adams, M., & Warmels, R. 2015, *ALMA Cycle 3 Technical Handbook*

Riechers, D. A., Stacey, G., Giovanelli, R., *et al.* 2015, IAU General Assembly, 22

Roddier, F. 1988, Applied Optics, 27, 1223

Rohlfs, K. & Wilson, T. 2004, *Tools of Radio Astronomy*, Astronomy and Astrophysics Library (Springer)

Ruze, J. 1966, IEEE Proceedings, 54, 633

Sanchez-de-la Llave, D. & Castillo, M. D. I. 2002, Applied optics, 41, 2607

Schelkunoff, S. A. & Friis, H. T. 1952, *Antennas: theory and practice*, Vol. 639 (Wiley, New York)

Serabyn, E. & Wallace, J. K. 2010, in *Millimeter, Submillimeter, and Far-Infrared Detectors and Instrumentation for Astronomy V, Society of Photo-Optical Instrumentation Engineers (SPIE) Conference Series*, Vol. 7741, 77410U

Silver, S. 1949, *Microwave Antenna Theory and Design*, Electromagnetics and Radar Series (P. Peregrinus)

Smartt, R. & Steel, W. 1975, Japanese Journal of Applied Physics, 14, 351

Stutzman, W. L. & Thiele, G. A. 2012, *Antenna theory and design* (John Wiley & Sons, New Jersey)

Terebizh, V. Y. 2008, Bulletin Crimean Astrophysical Observatory, 104, 179

TICRA Engineering Consultants. 2003, *Reference Manual for GRASP8*

Tsuzuki, T., Nitta, T., Imada, H., *et al.* 2015, Journal of Astronomical Telescopes, Instruments, and Systems, 1(2)

Vérinaud, C. 2004, Optics Communications, 233, 27

Wang, D., Wang, F., Zou, H., & Zhang, B. 2013, Applied optics, 52, 7602

Watson, G. N. 1966, *A treatise on the theory of Bessel functions second edition* (Cambridge university press, Cambridge)

Wilson, T. 2007, *Reflecting Telescope Optics I: Basic Design Theory and its Historical Development* (Springer, London)

Yamamoto, K., Matsuo, T., Imada, H., & Kino, M. 2015, Applied Optics, 54, 7895